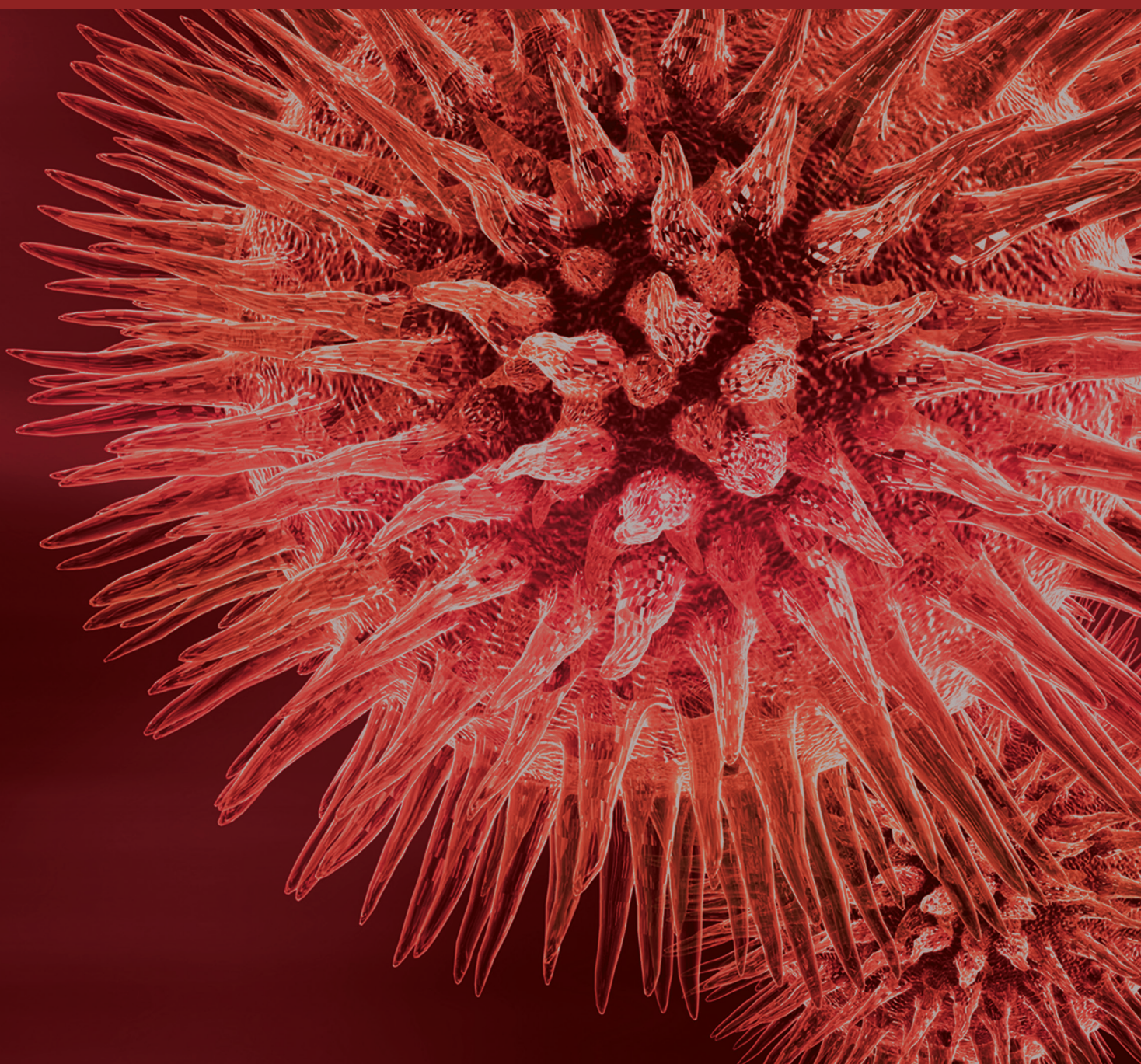


BioMed Research International

# Molecular Imaging for Personalized Medicine

Guest Editors: James Russell, Jie Tian, Seigo Kinuya, Baozhong Shen,  
and Xiao-Feng Li





---

# **Molecular Imaging for Personalized Medicine**

BioMed Research International

---

## **Molecular Imaging for Personalized Medicine**

Guest Editors: James Russell, Jie Tian, Seigo Kinuya,  
Baozhong Shen, and Xiao-Feng Li



---

Copyright © 2016 Hindawi Publishing Corporation. All rights reserved.

This is a special issue published in “BioMed Research International.” All articles are open access articles distributed under the Creative Commons Attribution License, which permits unrestricted use, distribution, and reproduction in any medium, provided the original work is properly cited.

## Contents

### **Molecular Imaging for Personalized Medicine**

James Russell, Jie Tian, Seigo Kinuya, Baozhong Shen, and Xiao-Feng Li  
Volume 2016, Article ID 5170159, 1 page

### **Personalized Medicine Based on Theranostic Radioiodine Molecular Imaging for Differentiated Thyroid Cancer**

Byeong-Cheol Ahn  
Volume 2016, Article ID 1680464, 9 pages

### **The Role of $^{99m}\text{Tc}$ -Annexin V Apoptosis Scintigraphy in Visualizing Early Stage Glucocorticoid-Induced Femoral Head Osteonecrosis in the Rabbit**

Xiaolong Wang, Yu Liu, Xuemei Wang, Rui Liu, Jianbo Li, Guoliang Zhang, Qiang Li, Lei Wang, Zhigang Bai, and Jianmin Zhao  
Volume 2016, Article ID 7067259, 6 pages

### **The Role of $^{18}\text{F}$ -FDG PET/CT and MRI in Assessing Pathological Complete Response to Neoadjuvant Chemotherapy in Patients with Breast Cancer: A Systematic Review and Meta-Analysis**

Qiufang Liu, Chen Wang, Panli Li, Jianjun Liu, Gang Huang, and Shaoli Song  
Volume 2016, Article ID 3746232, 10 pages

### **The Synthesis and Evaluations of the $^{68}\text{Ga}$ -Lissamine Rhodamine B (LRB) as a New Radiotracer for Imaging Tumors by Positron Emission Tomography**

Xuena Li, Yafu Yin, Bulin Du, Na Li, and Yaming Li  
Volume 2016, Article ID 8549635, 6 pages

### **$N$ - $^{11}\text{C}$ -Methyl-Dopamine PET Imaging of Sympathetic Nerve Injury in a Swine Model of Acute Myocardial Ischemia: A Comparison with $^{13}\text{N}$ -Ammonia PET**

Weina Zhou, Xiangcheng Wang, Yulin He, Yongzhen Nie, Guojian Zhang, Cheng Wang, Chunmei Wang, and Xuemei Wang  
Volume 2016, Article ID 8430637, 8 pages

### **Thyroid Remnant Estimation by Diagnostic Dose $^{131}\text{I}$ Scintigraphy or $^{99m}\text{TcO}_4^-$ Scintigraphy after Thyroidectomy: A Comparison with Therapeutic Dose $^{131}\text{I}$ Imaging**

Guanghai Liu, Na Li, Xuena Li, Song Chen, Bulin Du, and Yaming Li  
Volume 2016, Article ID 4763824, 5 pages

## Editorial

# Molecular Imaging for Personalized Medicine

James Russell,<sup>1</sup> Jie Tian,<sup>2</sup> Seigo Kinuya,<sup>3</sup> Baozhong Shen,<sup>4</sup> and Xiao-Feng Li<sup>5</sup>

<sup>1</sup>Memorial Sloan Kettering Cancer Center, New York, NY, USA

<sup>2</sup>Chinese Academy of Sciences, Beijing, China

<sup>3</sup>Kanazawa University, Kanazawa, Japan

<sup>4</sup>Harbin Medical University, Harbin, China

<sup>5</sup>University of Louisville, Louisville, KY, USA

Correspondence should be addressed to James Russell; russellj@mskcc.org and Xiao-Feng Li; linucmed@gmail.com

Received 23 June 2016; Accepted 23 June 2016

Copyright © 2016 James Russell et al. This is an open access article distributed under the Creative Commons Attribution License, which permits unrestricted use, distribution, and reproduction in any medium, provided the original work is properly cited.

This issue is devoted to molecular imaging in the context of personalized medicine. Recent advances in biology, particularly genomic and expression screens, have made it possible to hope that treatment can be matched very specifically to the patient's disease, as characterized at the molecular level. In oncology, where hopes for personalized medicine are perhaps highest, tumors will be treated based on the specific mutations that drive their unrestrained growth, rather than on their site of origin. For all branches of medicine, there is also the potential for matching drug dosage to the individual's drug metabolism profile, established through genetic analysis.

Along with genomic information, molecular imaging will be crucial in the development of personalized medicine. Molecular imaging—essentially any imaging procedure that delivers some information on a disease state, beyond the purely anatomical—is an incredibly diverse area of research, covering every disease state and imaging modality, with astonishing innovation in developing novel imaging agents. However, there are three aims that commonly emerge in the literature: to image some physiological/biological state that will be diagnostic/predictive; to observe treatment response; and to image the accumulation of drug in the lesion, an approach known as theranostics.

Appropriately, all these aims are represented in the six articles featured here. Dr. X. Li et al. (Shenyang, China) report the successful production of a <sup>68</sup>Ga labeled rhodamine based probe for PET imaging of mitochondrial potential in tumors, with the biology of probe uptake still to be clarified. Dr. W. Zhou et al. (Hohhot, China) demonstrate that N-11C methyl dopamine is a promising PET imaging

agent for cardiac reperfusion injury, comparing it with a commonly used PET tracer of perfusion, <sup>13</sup>N ammonium in a swine model. X. Wang et al., also from Hohhot, present a comparison between <sup>99m</sup>Tc labeled Annexin-V and methyl diphosphonate, in the detection of femoral head osteonecrosis in glucocorticoid treated rabbits, which indicates an advantage for Annexin-V in earlier detection of pathologic changes. B.-C. Ahn (Daegu, Republic of Korea) presents a review of theranostic imaging in the context of radioiodine treatment of differentiated thyroid cancer, while G. Liu et al. (Shenyang) make a practical contribution to this disease by demonstrating the superiority of <sup>131</sup>I imaging compared to <sup>99m</sup>TcO<sub>4</sub><sup>-</sup> in identifying remaining tissue in patients who have undergone surgery. Finally, Q. Liu et al. (Shanghai) publish a meta-analysis of <sup>18</sup>F-FDG PET/CT imaging and MRI in determining pathological complete response in breast cancer patients receiving neoadjuvant chemotherapy.

We hope that the reader will find something stimulating in this selection from an exciting and rapidly expanding area of research.

## Acknowledgments

As guest editors we would like to thank the featured authors for their high quality contributions.

James Russell  
Jie Tian  
Seigo Kinuya  
Baozhong Shen  
Xiao-Feng Li

## Review Article

# Personalized Medicine Based on Theranostic Radioiodine Molecular Imaging for Differentiated Thyroid Cancer

**Byeong-Cheol Ahn**

*Department of Nuclear Medicine, Kyungpook National University School of Medicine and Hospital,  
50 Samduk-dong 2-ga, Jung-gu, Daegu 700-721, Republic of Korea*

Correspondence should be addressed to Byeong-Cheol Ahn; abc2000@knu.ac.kr

Received 24 November 2015; Accepted 13 April 2016

Academic Editor: Jie Tian

Copyright © 2016 Byeong-Cheol Ahn. This is an open access article distributed under the Creative Commons Attribution License, which permits unrestricted use, distribution, and reproduction in any medium, provided the original work is properly cited.

Molecular imaging based personalized therapy has been a fascinating concept for individualized therapeutic strategy, which is able to attain the highest efficacy and reduce adverse effects in certain patients. Theranostics, which integrates diagnostic testing to detect molecular targets for particular therapeutic modalities, is one of the key technologies that contribute to the success of personalized medicine. Although the term “theranostics” was used after the second millennium, its basic principle was applied more than 70 years ago in the field of thyroidology with radioiodine molecular imaging. Differentiated thyroid cancer, which arises from follicular cells in the thyroid, is the most common endocrine malignancy, and theranostic radioiodine has been successfully applied to diagnose and treat differentiated thyroid cancer, the applications of which were included in the guidelines published by various thyroid or nuclear medicine societies. Through better pathophysiologic understanding of thyroid cancer and advancements in nuclear technologies, theranostic radioiodine contributes more to modern tailored personalized management by providing high therapeutic effect and by avoiding significant adverse effects in differentiated thyroid cancer. This review details the inception of theranostic radioiodine and recent radioiodine applications for differentiated thyroid cancer management as a prototype of personalized medicine based on molecular imaging.

## 1. Introduction

The term “theranostics” is portmanteau word of “therapeutics” and “diagnostics” and was coined by John Funkhouser (Chief Executive Officer of PharmaNetics) in 2002 to describe his company’s business model for developing diagnostic tests directly linked to the application of specific therapies [1, 2]. As an invaluable tool in personalized medicine, theranostics can be defined as a diagnostic methodology for individually tailored therapeutic intervention, and it customizes healthcare practices to an individual patient by eliminating unnecessary treatments for patients whom a standard therapy is not appropriate and/or by optimizing a therapeutic plan for a particular patient [3]. The theranostic system integrates diagnostic testing to detect the presence of a molecular target for which a specific therapeutic modality is intended [4].

Although we began using the term “theranostics” after the second millennium, the basic principle of theranostics has been applied for some time in the field of thyroidology;

radioiodine was used as the first theranostic agent [5]. Radioiodine theranostics is a typical example of personalized medicine and has been used extensively for the management of differentiated thyroid cancer [6, 7]. Better understanding of thyroid cancer pathophysiology and advancements in bioengineering, electrical engineering, and radiochemical technologies have improved radioiodine theranostics, which contributes to a tailored personalized management system for differentiated thyroid cancer.

This review details the inception of theranostic radioiodine as well as recent updates in radioiodine applications for differentiated thyroid cancer, which is a prototype of personalized medicine based on molecular imaging.

## 2. Radioiodine and Differentiated Thyroid Cancer

Although radioiodine has been used to diagnose and treat differentiated thyroid cancer for more than 70 years, the

accumulation of radioiodine in cancer cells was not fully understood until 1996, when the sodium iodide symporter (NIS) was first cloned by Carrasco et al. [8]. The NIS is an intrinsic plasma membrane glycoprotein with 13 transmembrane domains which actively transports one iodide into the cytosol of benign or malignant thyroid cells from extracellular fluid along with two sodium ions [9]. Administration of beta emitting radioiodine I-131 instead of naturally occurring stable iodine I-127 can selectively harm or kill the differentiated thyroid cancer cells that specifically accumulate iodine; in addition, the cells also can be imaged with gamma camera using gamma rays concomitantly emitted from I-131.

I-131 administration after total or near-total thyroidectomy can potentially have a tumoricidal effect on thyroid cancer cells that may persist after surgery, and radioiodine imaging using a gamma camera obtained at the time visualizes previously undiagnosed regional or distant metastatic lesions. In addition, postoperative I-131 administration may facilitate the early detection of a recurrence, based on serum thyroglobulin measurement or radioiodine imaging by removing residual normal thyroid tissues [10, 11]. Mazzaferri et al. had reported beneficial effects of I-131 administration as an initial therapy in differentiated thyroid cancer with long-term large cohort studies and ended up the debate of applying the I-131 administration to the disease which had spanned decades due to good prognosis and long course of the disease [12–14]. A number of subsequent studies confirmed the beneficial effects of reducing the recurrence and mortality rates and supported the use of I-131 administration as an initial adjuvant therapy for the disease [10, 11]. However, the beneficial effects of I-131 administration were not observed in all patients with the disease, and similar studies for patients at a lowest risk of recurrence or mortality revealed no such effect [10]. Therefore, individualized clinical decision-making is needed in certain patients who belong to subgroups in which this beneficial effect of I-131 administration is observed [10, 15–17].

### 3. Theranostic Molecular Imaging of Radioiodine

Radioiodine imaging was first molecular imaging performed by Dr. Benedict Cassen in 1950 at UCLA. He developed the rectilinear scanner and successfully imaged the gland, revealing biologic characteristics of the thyroid tissues using radioiodine before the era of tomographic imaging [18]. Molecular imaging allows visual representation, characterization, and quantification of the biological characteristics of cell and tissues within intact living organisms. Therefore, it can visualize the therapeutic targets of certain diseases [19].

In order to evaluate suspected but unproven cancers, diverse diagnostic imaging techniques have been applied, and these techniques can visualize and localize hidden cancerous lesions. Figure 1 demonstrates F-18 FDG PET imaging of ovarian cancer as a typical example of diagnostic imaging. The F-18 FDG PET study successfully visualized hidden malignant foci; however, the study cannot predict therapeutic response to chemotherapy. Patient A received systemic

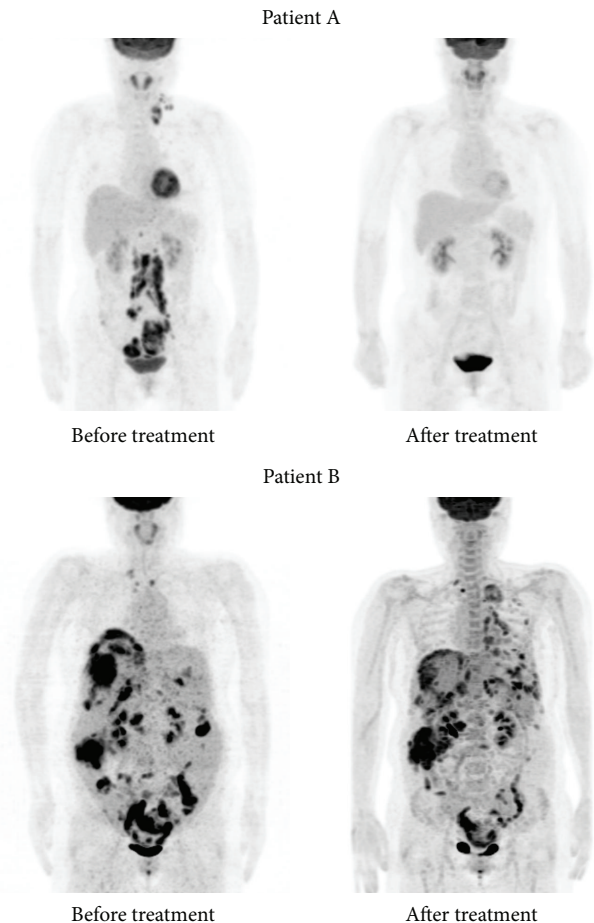


FIGURE 1: Patients A and B were diagnosed with advanced ovarian cancer. Pretreatment F-18 FDG PET imaging successfully visualized multiple cancerous lesions in the neck and abdominal cavity. However, the imaging was not able to predict the therapeutic response to the subsequent chemotherapy. Patient A achieved complete remission after chemotherapy; however, patient B progressed to disease status after chemotherapy.

chemotherapy due to far advanced disease stage based on the diagnostic imaging and complete remission was obtained by chemotherapy. However, patient B with a similar clinical condition as observed using diagnostic imaging underwent chemotherapy that did not yield any effects, based on the imaging, which was not able to forecast the therapeutic response, and the patient might experience adverse effects related to the chemotherapy.

Unlike diagnostic imaging studies, radioiodine imaging can forecast response to therapy and can therefore be used for theranostic imaging, which can potentially alter the decision to treat with I-131 and finalize the subsequent therapeutic dose of I-131 [10]. Figure 2 demonstrates the benefit of theranostic radioiodine imaging, which is able to forecast therapeutic response of metastatic thyroid cancer to I-131 treatment. Patient A, who has radioiodine avid metastatic lesions on radioiodine imaging, received I-131 treatment three times and was disease-free after the I-131 treatments. Patient B, who has a radioiodine nonavid metastatic lesions on

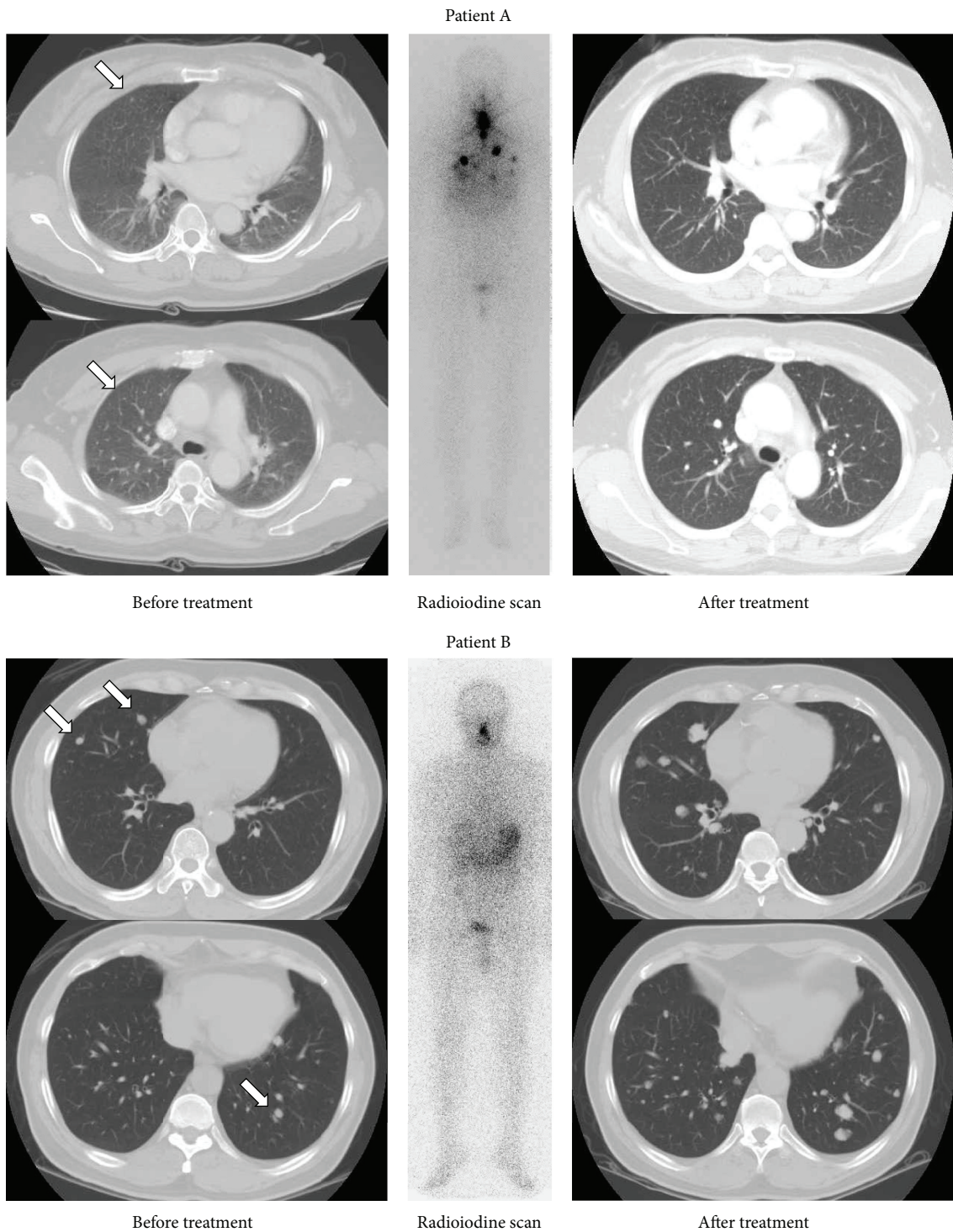


FIGURE 2: Patients A and B were diagnosed with thyroid cancer with pulmonary metastases (indicated by arrows) by pretreatment diagnostic CT imaging. Radioiodine imaging was able to forecast the therapeutic response to I-131 treatment. Patient A showed obvious uptake on radioiodine imaging and achieved complete remission after three I-131 treatments; however, patient B showed no radioiodine uptake on the imaging and progressed to disease status after I-131 treatment.

radioiodine imaging, revealed progressive disease after I-131 treatment.

To attain the best outcome, a therapeutic plan must be tailored to individual patients and can even be tailored to individual lesions in a patient. Theranostic radioiodine imaging can provide detailed biological status for each cancerous lesion and helps in predicting the therapeutic response of every lesion to I-131 treatment. Based on the imaging, ineffective I-131 treatment can be avoided, and furthermore, a lesion-based therapeutic plan can be established to overcome cancer heterogeneity, which is one of major therapeutic hurdles in oncologic diseases.

By applying dosimetric analysis to theranostic radioiodine imaging, the proper I-131 dose can be calculated and the response of each lesion to the I-131 therapy can be predicted by a lesion-based absorbed dose. The lesions might not respond completely to the therapy and may require a second-line treatment plan, such as surgical resection, external radiotherapy, or additional I-131 therapy to eradicate all lesions from individual patients. I-131 therapy combined with theranostic radioiodine imaging, which guides personalized or lesion-based therapeutic strategy, might be a representative model that demonstrates the ideal theranostic approach for personalized medicine.

I-131 treatment is the most important therapeutic option for treatment of differentiated thyroid cancer patients with iodine avid metastases, which cannot be resected by surgery [11]. Metastatic thyroid cancer lesions having iodine avidity are considered a more differentiated phenotype. However, metastatic lesions without iodine avidity, which do not respond to I-131 treatment, are a less differentiated phenotype and are prone to high glycolytic rates, which results in high glucose uptake on F-18 FDG PET. The inverse relation between iodine and glucose utilization in thyroid cancer according to the degree of differentiation, that is, the so-called flip-flop phenomenon, can occur in a thyroid cancer patient with multiple lesions due to heterogeneity of the metastases, which results in a mixed response to I-131 therapy [7, 20, 21]. Even though iodine avid metastases of a certain patient can be eradicated with I-131 therapy, FDG avid but iodine nonavid lesions of the patient need additional therapeutic strategies. Multimodal nuclear imaging is essential to design the lesion-based multimodal treatment strategy for patients with multiple heterogeneous metastatic lesions [22] (Figure 3).

#### 4. Optimization of Personalized Medicine with Theranostic Radioiodine Imaging

Although I-131 therapy is one of the well-established standard therapeutic modalities in differentiated thyroid cancer and dosimetric determination of I-131 dose has theoretical advantages over empirical dose determination, the I-131 dose was almost always decided empirically on the basis of local clinical experiences or according to reference values reported in the literatures [11, 23]. Popularity of empirical dose determination is mainly related to the fact that dosimetric methods were not feasibly applicable with commercially available imaging instruments and workstations. However, in order to

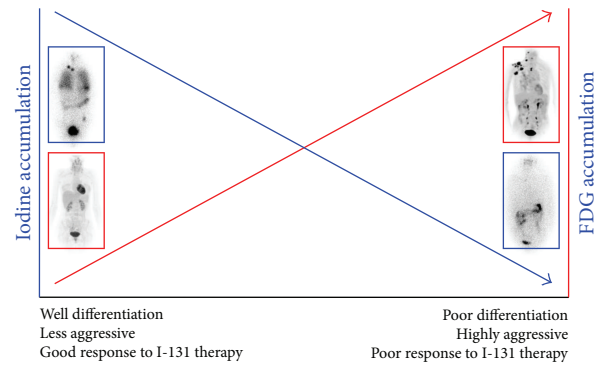
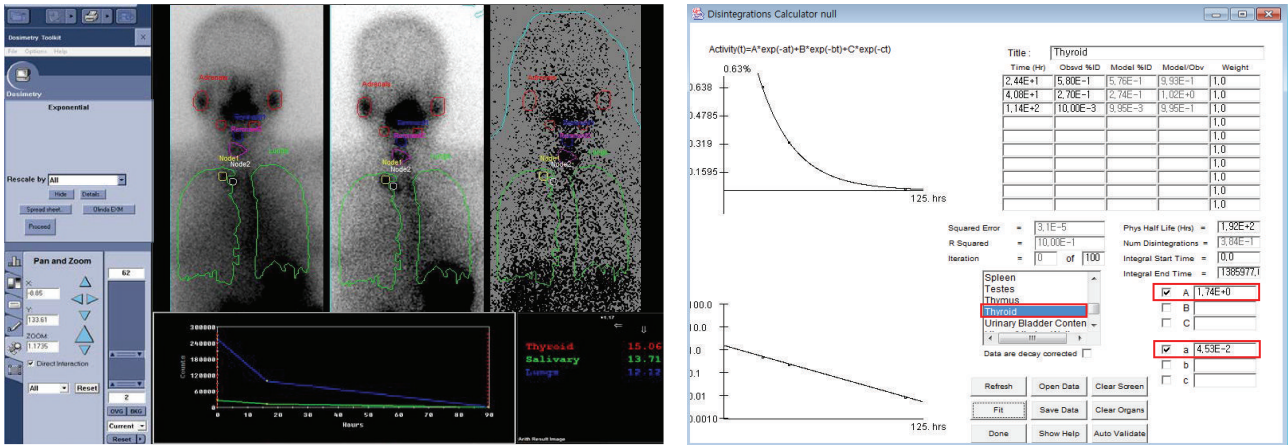


FIGURE 3: Flip-flop phenomenon of iodine and glucose avidity in thyroid cancer. Well-differentiated thyroid cancer has characteristics of the originating thyroid follicular cells, and therefore, the cancer cells can take up iodine, but not glucose. Therefore, the cancer lesions can be visualized on radioiodine imaging (blue box) but not on F-18 FDG PET imaging (red box). In contrast, poorly differentiated thyroid cancer does not have the characteristics of the originating thyroid follicular cells and has cancer hallmarks, and therefore, the cancer can take up glucose, but not iodine. Therefore, the cancer lesions can be visualized on F-18 FDG PET imaging, but not on radioiodine imaging.

decide the optimal therapeutic dose of I-131, which can attain the therapeutic goal, and to preclude unnecessary side effects, individual dosimetry with a diagnostic I-131 dose is essential. Contrary to the empirical fixed dose method, the dosimetric method takes into account anatomical and I-131 biokinetic characteristics of cancerous lesions in each individual patient [23]. In addition, dosimetry can also be performed with post-I-131-treatment imaging, and it not only predicts the response to the treatment but also is helpful in developing the following diagnostic and therapeutic plans for each individual patient.

Currently, with the progresses being made in the field, dosimetric tools of both hardware and software are available in commercial nuclear medicine imaging systems, and their implementation is also quite simple (Figure 4). Therefore, intervention of a health physicist is no longer an essential prerequisite for dosimetry. With the advent of SPECT/CT technology, the 3-dimensional (3D) absorbed dose-rate distribution from the Monte Carlo based calculation can be used to obtain the absorbed dose of the target and surrounding tissues more accurately. The dosimetric data calculated with the 3D technology provides a more accurate personalized dose of I-131, which is not only high enough to have therapeutic effects on the target tissue but also low enough to avoid significant adverse effects to nontarget organs [23].

Although the dosimetric method is logically superior to the empirical fixed dose method for determining the therapeutic dose of I-131, a fixed empirical dose approach has been preferred in most centers due to its simplicity and easy performance [11]. Other reasons for the popularity of the fixed dose method might originate from additional costs, patient discomfort, and the stunning issue by the dosimetric study before I-131 treatment. In addition, superiority of the dosimetric method over the empirical method is not obvious due to the lack of comprehensive clinical trials designed



Organ doses (mSv/MBq), nuclide: I-131 (8.02E00 day), adult female  
 Calculated: 07.21.2014 at 02:39:49 GMT

Target organ	Photon	Alpha total	Beta	Estimated absorbed dose to the metastatic LN = 3.15 mSv/MBq
...				
Salivary	4.26E - 02	0.00E000	4.50E - 01	
Lungs	3.04E - 02	0.00E000	1.50E - 01	
Metastatic LN (0.5 g)	0.00E000 3.15E000	2.95E000	2.03E - 01	
...				
Total body	0.00E000 4.02E - 02	2.41E - 02	1.61E - 02	

Number of disintegrations in source organs (N):	
...	
Thyroid	1.33E - 02 MBq-h/MBq or uCi-h/uCi
...	

FIGURE 4: Dosimetric assessment with multiple whole-body and SPECT images using a commercialized program. The retention time of each organ is obtained by imaging data with the images and the estimated absorbed doses for the organs and lesions are calculated using the OLINDA program.

to show the value of dosimetry for improving the therapy outcome [10, 23]. However, the dosimetric method can play important roles in I-131 treatment of differentiated thyroid cancer patients in unusual situations, such as distant thyroid cancer metastasis, renal insufficiency, or recombinant human thyroid stimulating hormone (TSH) application [10].

### 5. Radioiodine Treatment Coupled with Redifferentiation for Dedifferentiated Thyroid Cancer

Differentiated thyroid cancer has excellent prognosis compared to other malignancies, and this is partly related to the successful treatment of unresectable distant metastasis by therapeutic dose of I-131 administration. However, two-thirds of patients with distant metastases ultimately become radioiodine refractory disease [6, 7, 11, 20, 24–26]. The radioiodine refractory status is related to decreased

expression of the NIS and diminished targeting of NIS to the membrane of cancer cells or both [26, 27]. Localized radioiodine refractory thyroid cancer can be treated with surgery, stereotactic external beam therapy, thermal or laser or alcohol ablation, chemoembolization, or radioembolization. However, these local therapeutic approaches cannot be applied in cases with metastatic lesions that cannot be approached or in cases with numerous metastatic lesions. Systemic chemotherapy or targeted therapy with tyrosine kinase inhibitors can be applied to systemic disease; however, it is not used routinely due to a low response rate and high rate of severe adverse effects. In addition, tyrosine kinase has cytostatic effects rather than cell-killing effects on cancer cells and it might not be easy to attain cure for the disease [26].

Losing iodine avidity of differentiated thyroid cancer is related to genetic and epigenetic alterations and dysregulated signaling pathways, such as the MAPK and PI3K-AKT pathways, and research is currently on to identify compounds that

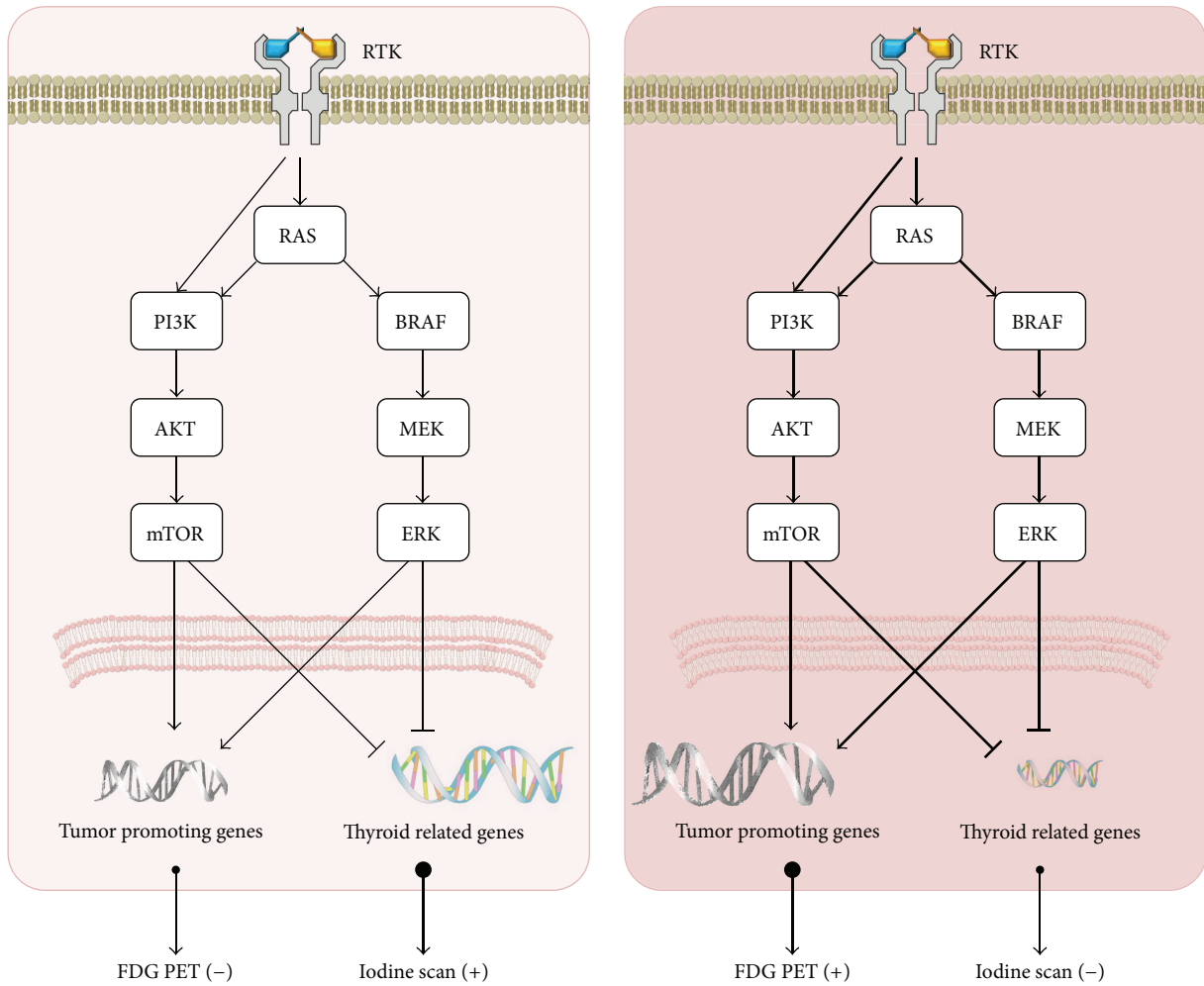


FIGURE 5: Signaling pathways related to iodine avidity or glucose avidity by thyroid cancers. Well-differentiated thyroid cancer has less iodine avidity and greater glucose avidity than normal thyroid follicular cell by activity of MAPK kinase and PI3K-AKT pathways, which inhibit the expression of thyroid related genes and reinforce the expression of tumor promoting genes. The pathways become more active in poorly differentiated thyroid cancer compared to well-differentiated thyroid cancer and eventually it loses the iodine avidity and acquires glucose avidity. RTK: receptor tyrosine kinase.

are able to increase iodine uptake by enhancing NIS expression and migration to the plasma membrane [26, 28–30] (Figures 5 and 6). Several compounds, such as retinoic acid, PPAR $\gamma$  agonists, HDAC inhibitors (valproic acid and carbamazepine), PI3K/AKT inhibitors, and MEK/ERK inhibitors, have been suggested to increase NIS expression and have resulted in increased iodine uptake in both *in vitro* and *in vivo* studies of thyroid cancers [28, 31].

The reinduction of NIS expression and iodine avidity in the radioiodine refractory cancer using redifferentiation therapy aids in curing the disease by applying I-131 treatment after the redifferentiation, similar to radioiodine therapy for unresectable metastatic differentiated thyroid cancer. To enhance radioiodine accumulation in radioiodine refractory thyroid cancer, retinoic acid has been used for more than 20 years to increase NIS expression. Although retinoic acid has the ability of increasing iodine uptake in the cancer, unfortunately, it is not used normally because the degree of

iodine accumulation by the drug is limited and a clinical response to radioiodine treatment after retinoic acid administration was marginal or negligible [32]. Drugs acting on peroxisome proliferator-activated receptor  $\gamma$  (PPAR $\gamma$ ) also have the ability of increasing iodine uptake in preclinical studies. However, the degree of iodine uptake by the drugs was not considerable, and the drugs are not frequently used in clinics to redifferentiate radioiodine refractory thyroid cancer before radioiodine treatment due to the limited therapeutic response [26, 33].

Expression of thyroid related genes is known to be related to MAPK kinase and PI3K-AKT pathways, and certain types of thyroid cancers have abnormal pathway activation due to oncogenic mutations, such as the BRAF V600E mutation. Increased activity of these pathways suppresses expression and membrane targeting of NIS protein [29, 34, 35].

Glycosylation of the NIS protein, posttranslational event of binding carbohydrates to the protein, is important for

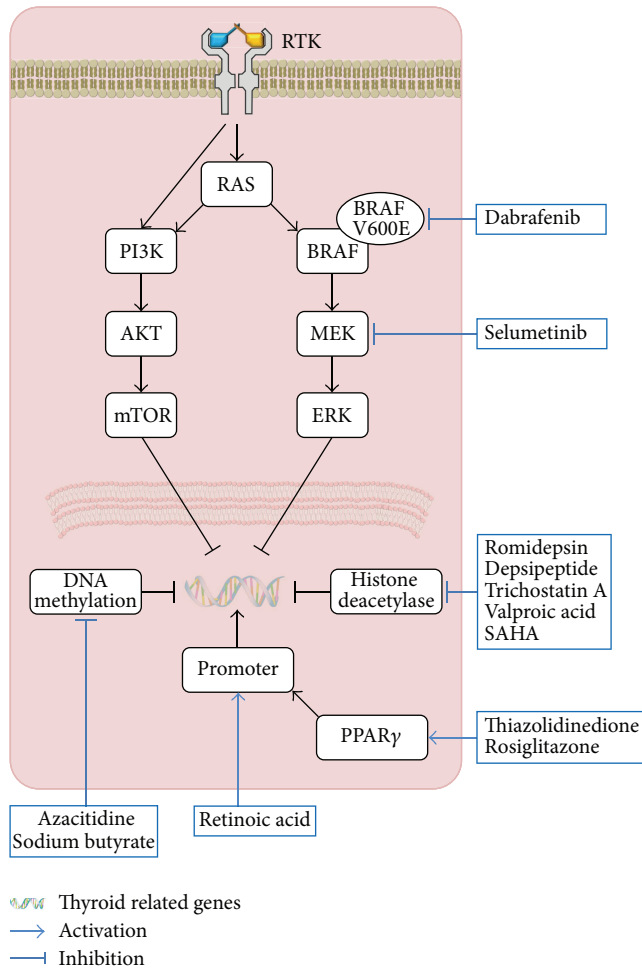


FIGURE 6: Strategies of pharmacologic redifferentiation of radioiodine refractory thyroid cancer by intervening genetic and epigenetic alterations and dysregulated signaling pathways related to the cancer.

proper localization of the transmembrane protein, which is essential for its function. Overexpression of PI3K decreases the glycosylation of the NIS protein and results in impairment of cellular iodine uptake [28]. The NIS gene expression and its migration to the proper location in a cell are differentially regulated based on the cell types, and therefore, certain drugs known to increase iodine uptake in one cell type will not work with equal potency or even reduce the iodine uptake in other cell types [28, 36]. Although certain radioiodine refractory thyroid cancers express NIS protein, the protein is predominantly localized in the cytoplasm and not in the plasma membrane, where it is not able to trap circulating iodine [37]. An understanding of the molecular mechanism for migration of NIS from the cytoplasm to the plasma membrane and methods to increase the translocation is needed for successful I-131 treatment of cancers with endogenous NIS expression. Unfortunately, the mechanism and methods might differ according to the subtypes of thyroid cancer, and therefore, the optimal strategy for enhancement of I-131 uptake should be tailored according to subtype [38].

Based on the redifferentiation effect of MAPK pathway inhibitor in preclinical studies, one clinical trial using the MEK inhibitor, selumetinib, revealed promising results of successful pharmacological redifferentiation of radioiodine refractory thyroid cancer [39].

## 6. Conclusions

Radioiodine- and NIS-based theranostics was used before coining the term “theranostics” and was successfully implemented as a representative model of personalized medicine for more than 70 years in the clinical field of differentiated thyroid cancer.

Personalized medicine using radioiodine theranostics can provide high therapeutic effects and avoid significant adverse effects through tailored therapeutic plans for individual patient, and rapid advancements in bio- and nuclear technologies can accelerate and broaden clinical application of the strategy for treating thyroid cancers with or without differentiation.

Preclinical studies for radioiodine theranostics are currently on to discover the hidden potential and the promising results are also being documented. Although inborn characteristics of limited universalization of personalized medicine may require time, the bench technology of radioiodine theranostics will be translated into clinical application as one of the tailored therapeutic approaches.

## Competing Interests

The author declares that they have no competing interests.

## Acknowledgments

This research was supported by a grant from the Medical Cluster R&D Support Project through the Daegu-Gyeongbuk Medical Innovation Foundation (DGMIF), funded by the Ministry of Health & Welfare, Republic of Korea (Grant no. HT13C0002), and by a grant from the Korea Health Technology R&D Project through the Korea Health Industry Development Institute (KHIDI), funded by the Ministry of Health & Welfare, Republic of Korea (Grant no. HI15C0001) and the National Research Foundation of Korea (NRF) grant funded by the Korean Government (MSIP) (no. NRF-2015M2A2A7A01045177).

## References

- [1] I. Gilham, *Theranostics an Emerging Tool in Drug Discovery and Commercialisation*, 2002, <http://www.ddw-online.com/personalised-medicine/pl48484-theranostics-an-emerging-tool-in-drug-discovery-and-commercialisation-fall-02.html>.
- [2] S. Jeelani, R. C. Jagat Reddy, T. Maheswaran, G. S. Asokan, A. Dany, and B. Anand, “Theranostics: a treasured tailor for tomorrow,” *Journal of Pharmacy and Bioallied Sciences*, vol. 6, supplement 1, pp. S6–S8, 2014.
- [3] S. M. Moghimi and Z. S. Farhangrazi, “Theranostics,” in *Encyclopedia of Cancer*, pp. 1–3, Springer, Berlin, Germany, 2015.

- [4] D. Y. Lee and K. C. P. Li, "Molecular theranostics: a primer for the imaging professional," *American Journal of Roentgenology*, vol. 197, no. 2, pp. 318–324, 2011.
- [5] E. B. Silberstein, "Radioiodine: the classic theranostic agent," *Seminars in Nuclear Medicine*, vol. 42, no. 3, pp. 164–170, 2012.
- [6] J.-R. Oh, B.-C. Ahn, S. Y. Jeong, S.-W. Lee, and J. Lee, "Radioiodine scan index: a simplified, quantitative treatment response parameter for metastatic thyroid carcinoma," *Nuclear Medicine and Molecular Imaging*, vol. 49, no. 3, pp. 174–181, 2015.
- [7] D.-H. Kim, J.-H. Jung, S. H. Son et al., "Difference of clinical and radiological characteristics according to radioiodine avidity in pulmonary metastases of differentiated thyroid cancer," *Nuclear Medicine and Molecular Imaging*, vol. 48, no. 1, pp. 55–62, 2014.
- [8] G. Dai, O. Levy, and N. Carrasco, "Cloning and characterization of the thyroid iodide transporter," *Nature*, vol. 379, no. 6564, pp. 458–460, 1996.
- [9] B.-C. Ahn, "Sodium iodide symporter for nuclear molecular imaging and gene therapy: from bedside to bench and back," *Theranostics*, vol. 2, no. 4, pp. 392–402, 2012.
- [10] D. S. Cooper, G. M. Doherty, B. R. Haugen et al., "Revised American thyroid association management guidelines for patients with thyroid nodules and differentiated thyroid cancer," *Thyroid*, vol. 19, no. 11, pp. 1167–1214, 2009.
- [11] B. R. M. Haugen, E. K. Alexander, K. C. Bible et al., "2015 American Thyroid Association Management guidelines for adult patients with thyroid nodules and differentiated thyroid cancer: The American Thyroid Association Guidelines task force on thyroid nodules and differentiated thyroid cancer," *Thyroid*, vol. 26, no. 1, pp. 1–133, 2015.
- [12] E. L. Mazzaferri and S. M. Jhiang, "Differentiated thyroid cancer long-term impact of initial therapy," *Transactions of the American Clinical and Climatological Association*, vol. 106, pp. 151–170, 1994.
- [13] E. L. Mazzaferri and S. M. Jhiang, "Long-term impact of initial surgical and medical therapy on papillary and follicular thyroid cancer," *The American Journal of Medicine*, vol. 97, no. 5, pp. 418–428, 1994.
- [14] E. L. Mazzaferri and R. T. Kloos, "Clinical review 128: current approaches to primary therapy for papillary and follicular thyroid cancer," *Journal of Clinical Endocrinology and Metabolism*, vol. 86, no. 4, pp. 1447–1463, 2001.
- [15] M. Luster, S. E. Clarke, M. Dietlein et al., "Guidelines for radioiodine therapy of differentiated thyroid cancer," *European Journal of Nuclear Medicine and Molecular Imaging*, vol. 35, no. 10, pp. 1941–1959, 2008.
- [16] E. B. Silberstein, A. Alavi, H. R. Balon et al., "The SNMMI practice guideline for therapy of thyroid disease with <sup>131</sup>I 3.0," *Journal of Nuclear Medicine*, vol. 53, no. 10, pp. 1633–1651, 2012.
- [17] H. Gharib, E. Papini, R. Paschke et al., "American Association of Clinical Endocrinologists, Associazione Medici Endocrinologi, and European Thyroid Association medical guidelines for clinical practice for the diagnosis and management of thyroid nodules," *Endocrine Practice*, vol. 16, supplement 1, pp. 1–43, 2010.
- [18] E. Tapscott, "The rectilinear scanner and an enduring legacy of education and research," *Journal of Nuclear Medicine*, vol. 39, no. 5, pp. 16–33, 1998.
- [19] J. E. Kim, S. Kalimuthu, and B. Ahn, "In vivo cell tracking with bioluminescence imaging," *Nuclear Medicine and Molecular Imaging*, vol. 49, no. 1, pp. 3–10, 2015.
- [20] C. M. Hong, B.-C. Ahn, S. Y. Jeong, S.-W. Lee, and J. Lee, "Distant metastatic lesions in patients with differentiated thyroid carcinoma: clinical implications of radioiodine and FDG uptake," *Nuklearmedizin*, vol. 52, no. 4, pp. 121–129, 2013.
- [21] J. W. Lee, H. S. Min, S. M. Lee, H. W. Kwon, and J. K. Chung, "Relations between pathological markers and radioiodine scan and <sup>18</sup>F-FDG PET/CT findings in papillary thyroid cancer patients with recurrent cervical nodal metastases," *Nuclear Medicine and Molecular Imaging*, vol. 49, no. 2, pp. 127–134, 2015.
- [22] B.-C. Ahn, "Applications of molecular imaging in drug discovery and development process," *Current Pharmaceutical Biotechnology*, vol. 12, no. 4, pp. 459–468, 2011.
- [23] M. Salvatori and M. Luster, "Radioiodine therapy dosimetry in benign thyroid disease and differentiated thyroid carcinoma," *European Journal of Nuclear Medicine and Molecular Imaging*, vol. 37, no. 4, pp. 821–828, 2010.
- [24] S. H. Son, S. Lee, J. Jung et al., "Analysis of clinical factors for the determination of optimal serum level of thyrotropin after recombinant human thyroid-stimulating hormone administration," *Nuclear Medicine and Molecular Imaging*, vol. 49, no. 4, pp. 268–275, 2015.
- [25] C. M. Hong, W. K. Lee, S. Y. Jeong, S.-W. Lee, B.-C. Ahn, and J. Lee, "Superiority of delayed risk stratification in differentiated thyroid cancer after total thyroidectomy and radioactive iodine ablation," *Nuclear Medicine Communications*, vol. 35, no. 11, pp. 1119–1126, 2014.
- [26] C. Spitzweg, K. C. Bible, L. C. Hofbauer, and J. C. Morris, "Advanced radioiodine-refractory differentiated thyroid cancer: the sodium iodide symporter and other emerging therapeutic targets," *The Lancet Diabetes and Endocrinology*, vol. 2, no. 10, pp. 830–842, 2014.
- [27] S. W. Oh, J. C. Paeng, and J. Chung, "New strategies for combined radioiodine therapy in refractory thyroid cancer," *Journal of Korean Thyroid Association*, vol. 8, no. 1, pp. 26–35, 2015.
- [28] S. Micali, S. Bulotta, C. Puppini et al., "Sodium iodide symporter (NIS) in extrathyroidal malignancies: focus on breast and urological cancer," *BMC Cancer*, vol. 14, no. 1, article 303, 2014.
- [29] S. M. Rothenberg, D. G. McFadden, E. L. Palmer, G. H. Daniels, and L. J. Wirth, "Redifferentiation of iodine-refractory BRAF V600E-mutant metastatic papillary thyroid cancer with dabrafenib," *Clinical Cancer Research*, vol. 21, no. 5, pp. 1028–1035, 2015.
- [30] T. S. Plantinga, B. Heinhuis, D. Gerrits et al., "mTOR inhibition promotes TTF1-dependent redifferentiation and restores iodine uptake in thyroid carcinoma cell lines," *Journal of Clinical Endocrinology and Metabolism*, vol. 99, no. 7, pp. E1368–E1375, 2014.
- [31] K.-P. Wong and B. H.-H. Lang, "New molecular targeted therapy and redifferentiation therapy for radioiodine-refractory advanced papillary thyroid carcinoma: literature review," *Journal of Thyroid Research*, vol. 2012, Article ID 818204, 9 pages, 2012.
- [32] S. W. Oh, S.-H. Moon, D. J. Park et al., "Combined therapy with <sup>131</sup>I and retinoic acid in Korean patients with radioiodine-refractory papillary thyroid cancer," *European Journal of Nuclear Medicine and Molecular Imaging*, vol. 38, no. 10, pp. 1798–1805, 2011.
- [33] W. T. Shen and W.-Y. Chung, "Treatment of thyroid cancer with histone deacetylase inhibitors and peroxisome proliferator-activated receptor- $\gamma$  agonists," *Thyroid*, vol. 15, no. 6, pp. 594–599, 2005.

- [34] M. Xing, "Molecular pathogenesis and mechanisms of thyroid cancer," *Nature Reviews Cancer*, vol. 13, no. 3, pp. 184–199, 2013.
- [35] M. Xing, B. R. Haugen, and M. Schlumberger, "Progress in molecular-based management of differentiated thyroid cancer," *The Lancet*, vol. 381, no. 9871, pp. 1058–1069, 2013.
- [36] S. Beyer, A. Lakshmanan, Y.-Y. Liu et al., "KT5823 differentially modulates sodium iodide symporter expression, activity, and glycosylation between thyroid and breast cancer cells," *Endocrinology*, vol. 152, no. 3, pp. 782–792, 2011.
- [37] T. D. Singh, S. Y. Jeong, S.-W. Lee et al., "Inverse agonist of estrogen-related receptor gamma enhances sodium iodide symporter function through mitogen-activated protein kinase signaling in anaplastic thyroid cancer cells," *Journal of Nuclear Medicine*, vol. 56, no. 11, pp. 1690–1696, 2015.
- [38] S. J. Beyer, X. Zhang, R. E. Jimenez et al., "Microarray analysis of genes associated with cell surface NIS protein levels in breast cancer," *BMC Research Notes*, vol. 4, article 397, 2011.
- [39] A. L. Ho, R. K. Grewal, R. Leboeuf et al., "Selumetinib-enhanced radioiodine uptake in advanced thyroid cancer," *The New England Journal of Medicine*, vol. 368, no. 7, pp. 623–632, 2013.

## Research Article

# The Role of $^{99m}\text{Tc}$ -Annexin V Apoptosis Scintigraphy in Visualizing Early Stage Glucocorticoid-Induced Femoral Head Osteonecrosis in the Rabbit

Xiaolong Wang,<sup>1</sup> Yu Liu,<sup>1</sup> Xuemei Wang,<sup>2</sup> Rui Liu,<sup>1</sup> Jianbo Li,<sup>2</sup> Guoliang Zhang,<sup>1</sup> Qiang Li,<sup>1</sup> Lei Wang,<sup>3</sup> Zhigang Bai,<sup>2</sup> and Jianmin Zhao<sup>1</sup>

<sup>1</sup>Department of Surgery, Affiliated Hospital of Inner Mongolia Medical University, No. 1 Tongdao North Street, Hohhot, Inner Mongolia 010050, China

<sup>2</sup>Department of Nuclear Medicine, Affiliated Hospital of Inner Mongolia Medical University, No. 1 Tongdao North Street, Hohhot, Inner Mongolia 010050, China

<sup>3</sup>Fuwai Hospital, Beijing, China

Correspondence should be addressed to Jianmin Zhao; nmzjmin@163.com

Received 17 November 2015; Accepted 17 January 2016

Academic Editor: James Russell

Copyright © 2016 Xiaolong Wang et al. This is an open access article distributed under the Creative Commons Attribution License, which permits unrestricted use, distribution, and reproduction in any medium, provided the original work is properly cited.

**Objective.** To validate the ability of  $^{99m}\text{Tc}$ -Annexin V to visualize early stage of glucocorticoid-induced femoral head necrosis by comparing with  $^{99m}\text{Tc}$ -MDP bone scanning. **Methods.** Femoral head necrosis was induced in adult New Zealand white rabbits by intramuscular injection of methylprednisolone.  $^{99m}\text{Tc}$ -Annexin scintigraphy and  $^{99m}\text{Tc}$ -MDP scans were performed before and 5, 6, and 8 weeks after methylprednisolone administration. Rabbits were sacrificed at various time points and conducted for TUNEL and H&E staining. **Results.** All methylprednisolone treated animals developed femoral head necrosis; at 8 weeks postinjection, destruction of bone structure was evident in H&E staining, and apoptosis was confirmed by the TUNEL assay. This was matched by  $^{99m}\text{Tc}$ -Annexin V images, which showed a significant increase in signal over baseline. Serial  $^{99m}\text{Tc}$ -Annexin V scans revealed that increased  $^{99m}\text{Tc}$ -Annexin V uptake could be observed in 5 weeks. In contrast, there was no effect on  $^{99m}\text{Tc}$ -MDP signal until 8 weeks. The TUNEL assay revealed that bone cell apoptosis occurred at 5 weeks. **Conclusion.**  $^{99m}\text{Tc}$ -Annexin V is superior to  $^{99m}\text{Tc}$ -MDP for the early detection of glucocorticoid-induced femoral head necrosis in the rabbit and may be a better strategy for the early detection of glucocorticoid-induced femoral head necrosis in patients.

## 1. Introduction

Glucocorticoid-induced necrosis of the femoral head (also known as glucocorticoid-induced avascular necrosis or aseptic necrosis of the femoral head) was initially reported in the 1950s [1]. In China, it is estimated that there are approximately 5 to 7.5 million patients suffering from femoral head necrosis, with 75,000 to 150,000 new cases each year [2]. Glucocorticoid is the primary cause of nontrauma femoral head necrosis, a condition which seriously reduces the patient's quality of life and ability to work, and eventually requires artificial joint replacement in the majority of cases. If femoral head necrosis can be detected at a very early stage, it may

be possible to prevent the collapse of the femoral head, preserving joint function, delaying progression of the disease, leading to an overall reduction in morbidity [3–5].

In previous decades, the pathogenesis of glucocorticoid-induced osteonecrosis has been ascribed to increasing intraosseous pressure and decreased blood perfusion in the bone, fat embolism, or a hypercoagulable state [5]. Recently, it has been demonstrated that glucocorticoid-induced bone of femoral head necrosis is closely associated with bone cell apoptosis, and, using a rabbit model, Hwang et al. demonstrated the early appearance of apoptosis after glucocorticoid treatment [6]. Youm et al. found that high dose glucocorticoid significantly increased apoptosis in osteoblast and osteoclast

cells in the femoral head, with subsequent trabecular bone fracture and femoral head collapse; further, apoptosis of osteoblasts reduced bone reconstruction and repair [7, 8], without affecting the vascular supply to the femoral head [8]. In transplant patients, Rojas et al. demonstrated osteoblastic cell apoptosis after high dose glucocorticoid [9], further supporting a role for programmed cell death in glucocorticoid-induced femoral head necrosis in patients and animals.

$^{99m}\text{Tc}$ -Annexin V is a radionuclide-labeled molecular probe for detecting apoptosis that has been validated in animal experiments and preliminary clinical use [10, 11].  $^{99m}\text{Tc}$ -Annexin V imaging successfully detected apoptotic cells in acute myocardial infarction, myocarditis, cardiac transplant rejection, unstable atherosclerotic plaque, and cancer after effective chemotherapy [11]. Recently,  $^{99m}\text{Tc}$ -Annexin V has been used to monitor the therapeutic effect of antiapoptosis drugs in heart failure patients [12–14]. We hypothesized that  $^{99m}\text{Tc}$ -Annexin V scintigraphy would successfully image apoptosis in the femoral head and so enable visualization of early stage disease.

In this study, using a rabbit model, glucocorticoid-induced necrosis of the femoral head was imaged with both  $^{99m}\text{Tc}$ -Annexin V and  $^{99m}\text{Tc}$ -MDP bone scan. Comparison of the two imaging agents suggests that  $^{99m}\text{Tc}$ -Annexin V may be superior.

## 2. Materials and Methods

**2.1. Animals.** Adult New Zealand white rabbits were purchased from Di Dunlop Biological Resources Development Co. (Xi'an, China). Rabbits were maintained and used according to the guidelines of Inner Mongolian Medical University Animal Care and Use Committee. The animal study protocols were approved by the committee. Rabbits were housed singly and supplied with standard diet.

**2.2. Generation of a Rabbit Model of Glucocorticoid-Induced Femoral Head Necrosis.** Experiments were performed on 20 rabbits (body weight  $2.5 \pm 0.3$  kg, 10 male, 10 female). Animals were acclimated in the vivarium for one week and injected intramuscularly with methylprednisolone (7.5 mg/kg), twice weekly for 8 weeks to generate femoral head necrosis. Six control rabbits received saline by the same route and schedule.

**2.3.  $^{99m}\text{Tc}$ -Annexin V Scintigraphy and  $^{99m}\text{Tc}$ -MDP Bone Scans.** Annexin V was labeled in-house as previously described [10–14], to a radiochemical purity of 90%. 0.5 mCi (18.5 MBq) was injected via the ear vein and imaging was performed 1 hour later. Bone scintigraphy was performed 48 hours prior to  $^{99m}\text{Tc}$ -Annexin V imaging.  $^{99m}\text{Tc}$ -MDP (0.5 mCi [18.5 MBq], radiochemical purity 95%) was injected via the ear vein and imaged 2 hours subsequently.

Imaging was performed with a clinical dual-head detector SPECT/CT (Millennium VG, Hawkeye; GE Healthcare) equipped with low-energy and high-resolution collimators (peak energy 140 keV, window width 20%). Animals were anesthetized by inhalation of isoflurane (1.5–2%)-air mixture

for a 6 min planar scan. SPECT data was acquired into a  $128 \times 128$  matrix.

The images were processed using a postprocessing system workstation. Tracer uptake was expressed as the ratio of signal in limb joints to mediastinum (T/N). And images were read by two nuclear medicine physicians who were blinded to the pathologic findings. In case of disagreement, a third nuclear medicine physician made a diagnostic conclusion.

**2.4. Preparation of Femoral Head Paraffin Sections for Histological Assay.** Rabbits were sacrificed either by intravenous injection of sodium pentobarbital or air embolism. The femoral heads were resected and stored in 10% formalin solution. Femoral heads were decalcified by immersing in Surgipath II decalcification solution (10% formaldehyde, 8% formic acid, and 1% methanol; Surgipath, Richmond, USA) for approximately 1 week and subsequently embedded in paraffin. Blocks were sectioned ( $4 \mu\text{m}$  slices) every 1 mm throughout the bone.

**2.5. TUNEL Assay.** Terminal deoxynucleotidyl transferase-(TDT-) mediated dUTP nick end labeling (TUNEL) was performed according to the kit manufacturer's instructions (Thermo Scientific, USA) for tissue sections. Slices were dewaxed with freshly prepared 3%  $\text{H}_2\text{O}_2$  solution at room temperature for 10 min and treated with proteinase K at  $37^\circ\text{C}$  for 10 min. Tissue was covered with  $20 \mu\text{L}$  labeling buffer containing TDT ( $1 \mu\text{L}$ ) and DIG-dUTP ( $1 \mu\text{L}$ ) and incubated for 2 h at  $37^\circ\text{C}$  in 100% humidity. Biotinylated antidigoxigenin antibody was applied ( $50 \mu\text{L}$  per specimen,  $37^\circ\text{C}$  for 30 min) followed by SABC ( $10 \mu\text{L}$ ,  $37^\circ\text{C}$ , 30 min) and finally stained with hematoxylin for 2 s. TUNEL-positive cells were identified through the nucleus, which was either stained tan or brown. Five fields were randomly selected and the osteoblast apoptosis index was calculated as the ratio of apoptotic to total cells.

**2.6. Statistical Analysis.** SPSS19.0 software (IBM, USA) was used for statistical analysis. Data was expressed as mean  $\pm$  standard deviation. Student's *t*-test was used to compare differences between groups, and a *P* value less than 0.05 was considered statistically significant.

## 3. Results

Five weeks following methylprednisolone injection, rabbits displayed decreased activity, malaise, a decrease in lower limb body support, and reduced food intake. All animals developed femur head necrosis as confirmed by H&E staining and TUNEL at 8 weeks (Figure 1).

Planar scintigraphy performed 1 day before and 8 weeks after methylprednisolone administration in 6 rabbits showed that  $^{99m}\text{Tc}$ -Annexin V accumulation in the femoral heads had significantly increased. (Representative  $^{99m}\text{Tc}$ -Annexin V images are presented in Figures 2(a) and 2(b).) Subsequent histology indicated the presence of elevated levels of apoptosis (Figure 2(c)).

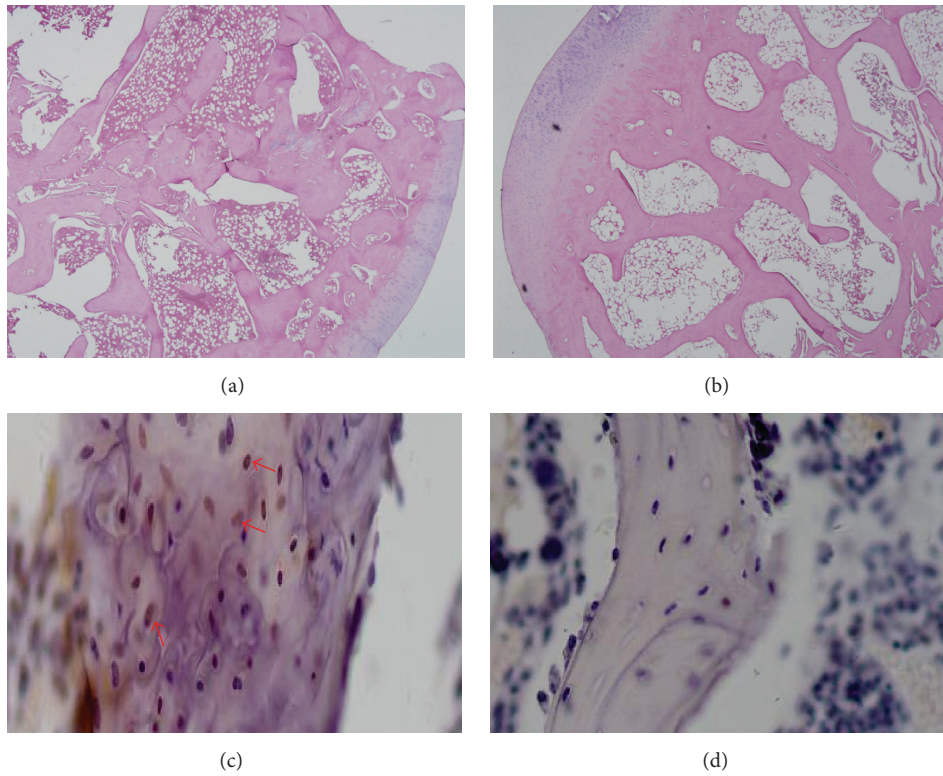


FIGURE 1: Histological images demonstrating methylprednisolone-induced femoral head necrosis. (a) Representative H&E stained section of a femoral head, 8 weeks after methylprednisolone administration, showing destruction of the bone structure (2 rabbits were examined). (b) Representative H&E stained section of a femoral head section from a control rabbit treated with saline (2 rabbits were examined). (c) TUNEL assay of a femoral head, 8 weeks after methylprednisolone administration. Apoptotic cells (indicated by arrows) are stained brown. (d) TUNEL assay of a femoral head from a control rabbit treated with saline.

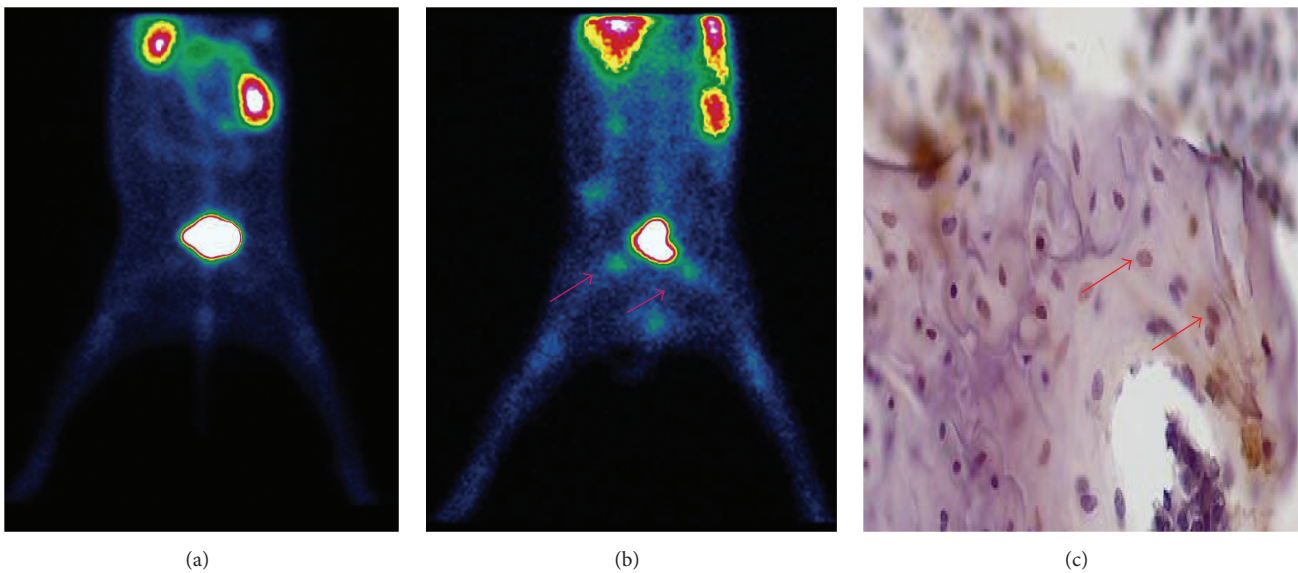


FIGURE 2: Representative <sup>99m</sup>Tc-Annexin V images of methylprednisolone-induced femoral head necrosis. (a) <sup>99m</sup>Tc-Annexin V image of a saline-treated rabbit as control. (b) <sup>99m</sup>Tc-Annexin V image of a rabbit after 8 weeks of prednisolone treatment. Radioactivity accumulates in the femoral head regions as indicated by the arrows. (c) TUNEL assay of a femoral head section, 8 weeks after prednisolone administration, with apoptotic cells stained brown, as indicated by the arrow.

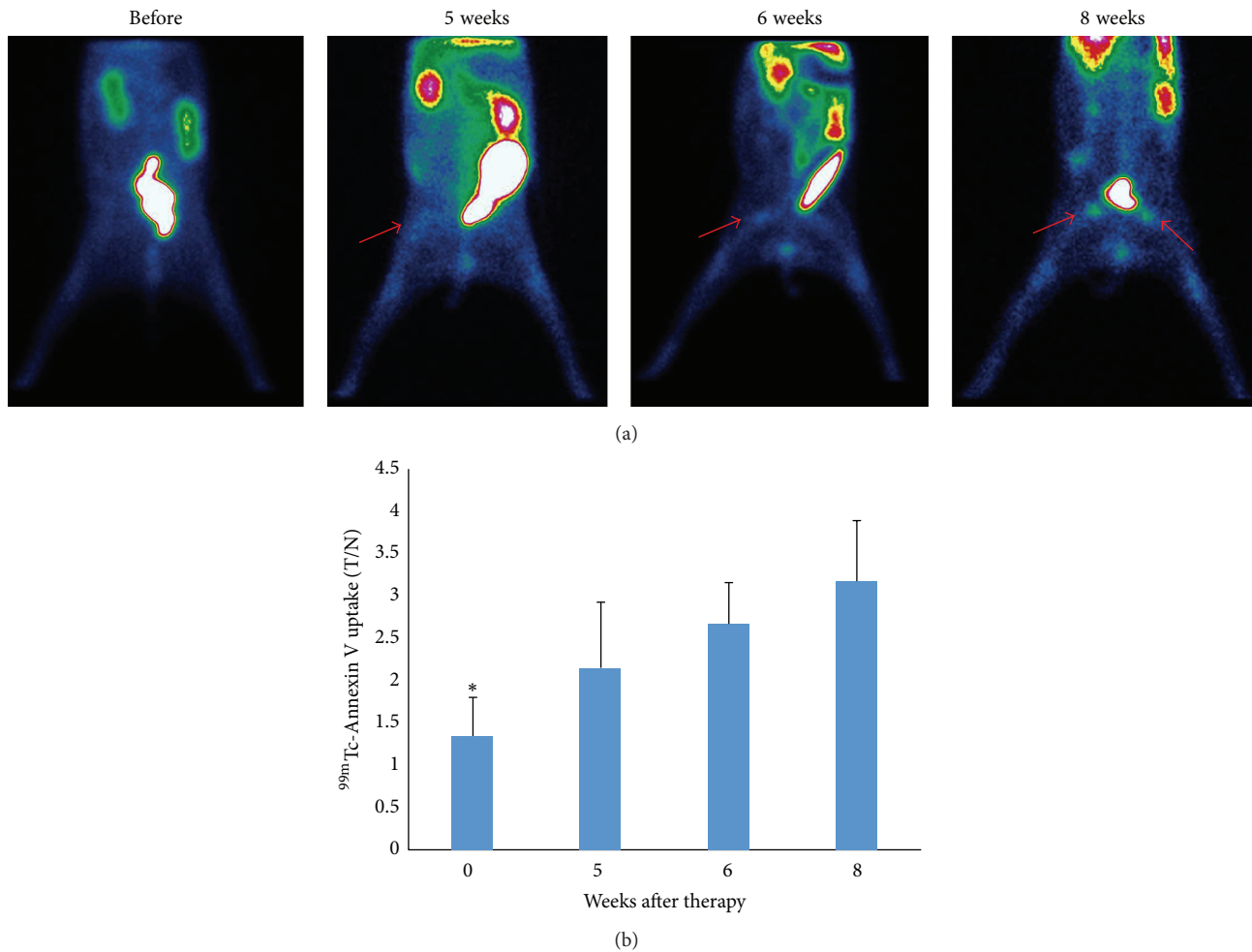


FIGURE 3: Serial  $^{99m}\text{Tc}$ -Annexin V scans in methylprednisolone treated rabbits. (a) Scans were performed before therapy and 5–8 weeks after initiation by methylprednisolone. Increasing  $^{99m}\text{Tc}$ -Annexin V uptake is observed as early as approximately 5 weeks after the start of prednisolone treatment. (b)  $^{99m}\text{Tc}$ -Annexin V uptake, expressed as T/N, significantly increased with time.

To observe the disease development process, we performed serial  $^{99m}\text{Tc}$ -Annexin V scans in 6 rabbits (3 male, 3 female). Scans were collected before treatment and 5–8 weeks after the initiation of methylprednisolone treatment. As shown in Figure 3(a), increased  $^{99m}\text{Tc}$ -Annexin V uptake was observed as early as approximately 5 weeks after commencing methylprednisolone.  $^{99m}\text{Tc}$ -Annexin V uptake, expressed as T/N, was significantly increased over baseline at all observed time points (Figure 3(b)).

$^{99m}\text{Tc}$ -MDP bone scans were performed in the same group of animals two days prior to  $^{99m}\text{Tc}$ -Annexin V imaging. Abnormal femoral head uptake of  $^{99m}\text{Tc}$ -MDP was not observed until 8 weeks, when it was significantly higher than pretreatment ( $P < 0.01$ ) (Figure 4).

In a separate group, 6 rabbits were treated with methylprednisolone and sacrificed at 5, 6, and 8 weeks after treatment (two animals per time point and four control animals). The TUNEL assay revealed a significantly higher apoptotic

index in the treated femoral heads at each endpoint ( $P < 0.05$ ) relative to the controls (Figure 5).

#### 4. Discussion

Animal models of glucocorticoid-induced femoral head osteonecrosis mimic human disease and are thus critically important for in-depth studies of both pathogenesis and therapy. Importantly, we have successfully established that, in methylprednisolone-induced femoral head osteonecrosis in rabbits, the pathogenesis was closely related to bone cell apoptosis (Figure 1). We have also used this model to validate that  $^{99m}\text{Tc}$ -Annexin V apoptosis imaging is superior to  $^{99m}\text{Tc}$ -MDP for the early detection of the disease (Figures 2–4).

Glucocorticoid treatment is the leading cause of non-traumatic femoral head necrosis [15]. However, in the asymptomatic early stage, the disease is difficult to diagnose with current imaging modalities. In 1971, Harrington et

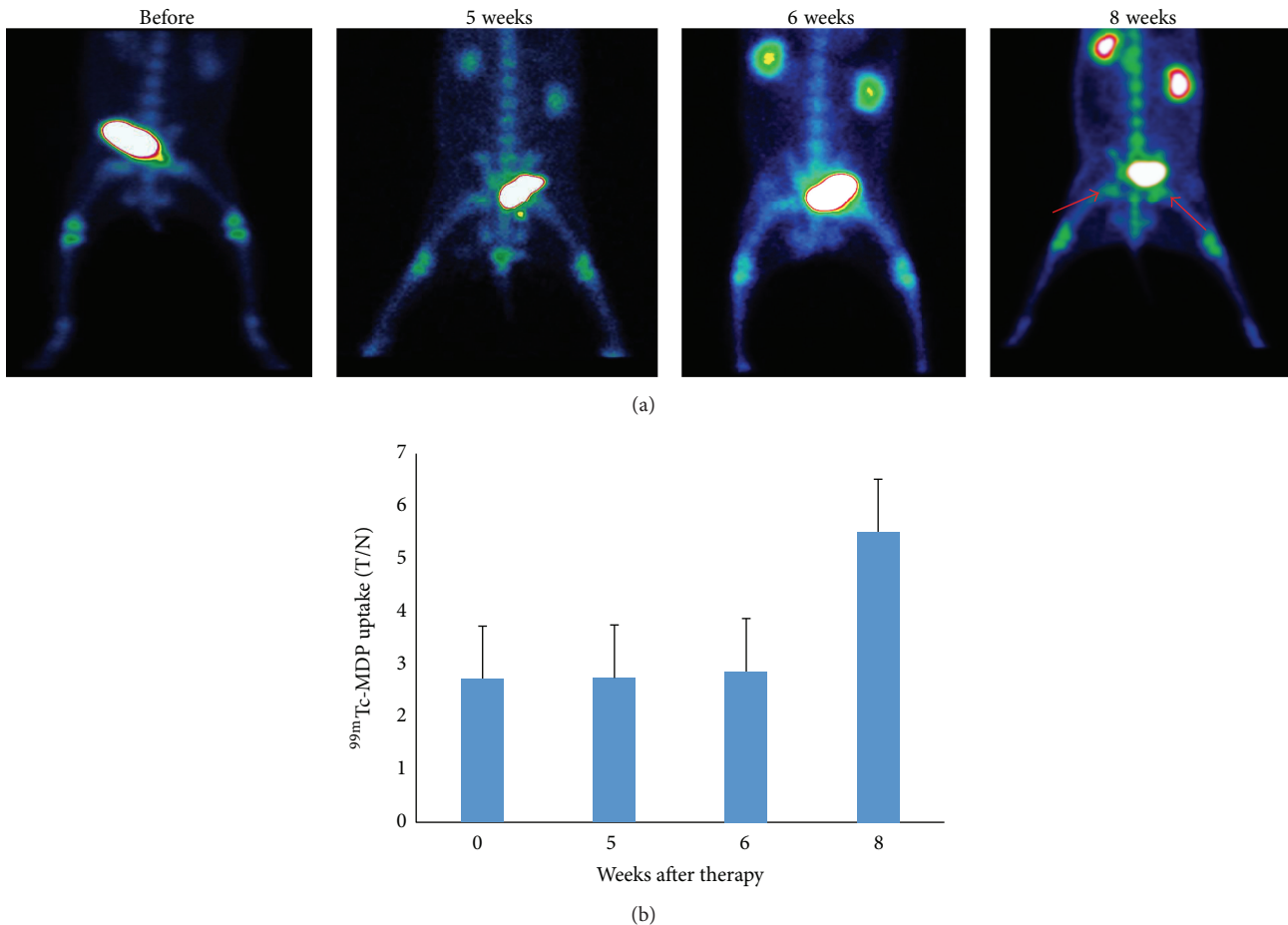


FIGURE 4: Serial  $^{99m}\text{Tc}$ -MDP bone scans in methylprednisolone treated rabbits. Animals from Figure 3 were scanned with  $^{99m}\text{Tc}$ -MDP, two days prior to  $^{99m}\text{Tc}$ -Annexin V imaging. (a) Abnormal  $^{99m}\text{Tc}$ -MDP is found by 8 weeks, as indicated by the arrow. (b) A significant increase in  $^{99m}\text{Tc}$ -MDP is observed only at 8 weeks after methylprednisolone exposure, \* $P < 0.01$  at 8 weeks versus the rest of the time points. There were no significant differences in  $^{99m}\text{Tc}$ -MDP uptake between pretherapy (week 0) and 5 or 6 weeks.

al. [16] were the first to describe bone avascular necrosis in renal transplant patients treated with glucocorticoids. Subsequently, the key role of apoptosis in the pathogenesis of glucocorticoid-induced necrosis was established [7]. Accordingly, in this study we hypothesized that apoptosis imaging may visualize early pathological changes in the femoral head.  $^{99m}\text{Tc}$ -Annexin V successfully detected the onset of femoral head necrosis after 5 weeks of continuous glucocorticoid administration (Figure 3) and was much more sensitive than a  $^{99m}\text{Tc}$ -MDP bone scan (Figure 4), which is currently considered the gold standard for the clinical diagnosis of femoral head necrosis. The imaging results were consistent with the TUNEL assay which demonstrated the presence of apoptosis 5 weeks after methylprednisolone administration.

Annexin V specifically binds to phosphatidylserine on the surface of early apoptotic cells and is widely used to detect apoptosis [17]. Radionuclide-labeled Annexin V has been used for the in vivo detection of apoptosis [18–20] and has been the subject of clinical trials in the US and Europe

designed to assess chemotherapy of small-cell lung cancer [21]. To the best of our knowledge,  $^{99m}\text{Tc}$ -Annexin V has not yet been used to detect very early stage glucocorticoid-induced femoral head osteonecrosis.

$^{99m}\text{Tc}$ -Annexin V apoptosis imaging was found to be superior to  $^{99m}\text{Tc}$ -MDP bone scintigraphy for the early detection of glucocorticoid-induced femoral head osteonecrosis (Figures 3 and 4) and may be used to observe the therapeutic effect of novel treatment strategies. We are in the process of using  $^{99m}\text{Tc}$ -Annexin V SPECT to study and evaluate patients who have received high dose glucocorticoid for various reasons.

## 5. Conclusions

$^{99m}\text{Tc}$ -Annexin V apoptosis imaging is superior to  $^{99m}\text{Tc}$ -MDP bone imaging for the early detection of glucocorticoid-induced femoral head necrosis in the rabbit and may be a

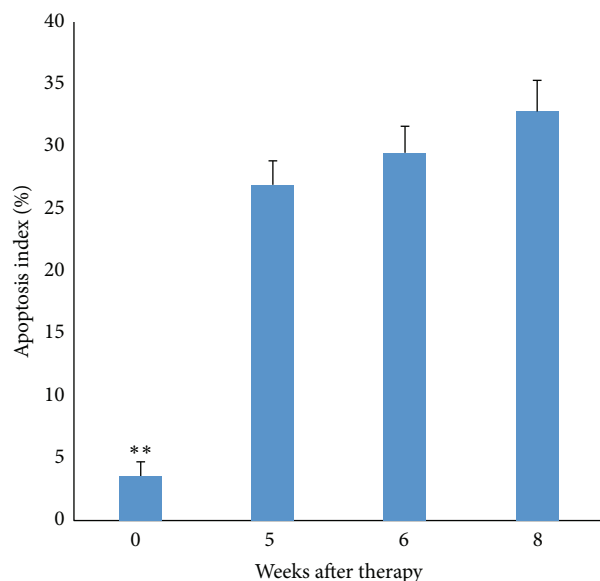


FIGURE 5: Apoptotic frequency as a function of time after treatment by TUNEL assay. The frequency of apoptosis as assessed by TUNEL in rabbits sacrificed at 5, 6, and 8 weeks after methylprednisolone treatment. Control animals were treated with saline. Each treated point represents 4 femoral heads and 8 in the control group,  $**P < 0.001$ .

better strategy for detecting early stage femoral head necrosis induced by glucocorticoid in patients.

### Conflict of Interests

The authors declare that there is no conflict of interests regarding the publication of this paper.

### Authors' Contribution

Xiaolong Wang and Yu Liu contributed equally to this paper.

### Acknowledgments

This study was supported by Natural Science Foundation of China (81360224), the Inner Mongolia Major Basic Science Research Program award for a project entitled Hypoxic Microenvironment of Lung Cancer Metastases and Hypoxia Targeted Therapy and Inner Mongolia Science and Technology Innovation project (2015cztcxyd03).

### References

- [1] V. Pietrogande and R. Mastromarino, "Osteopat da prolungata trattamento cortisonico," *Orthop Traum Appar Mat*, vol. 25, pp. 791–810, 1957.
- [2] Y. Chen, "Progress in the etiology of femoral head necrosis," *Huaxi Medicine Journal*, vol. 24, no. 7, pp. 1899–1901, 2009.
- [3] R. S. Weinstein, "Glucocorticoid-induced osteonecrosis," *Endocrine*, vol. 41, no. 2, pp. 183–190, 2012.
- [4] K. L. Chan and C. C. Mok, "Glucocorticoid-induced avascular bone necrosis: diagnosis and management," *The Open Orthopaedics Journal*, vol. 6, no. 1, pp. 449–457, 2012.
- [5] W. Drescher, G. Schlieper, J. Floege, and F. Eitner, "Steroid-related osteonecrosis-an update," *Nephrology Dialysis Transplantation*, vol. 26, no. 9, pp. 2728–2731, 2011.
- [6] Y. Hwang, J. Park, S. H. Choi, and G. Kim, "Traumatic and non-traumatic osteonecrosis in the femoral head of a rabbit model," *Laboratory Animal Research*, vol. 27, no. 2, pp. 127–131, 2011.
- [7] Y.-S. Youm, S.-Y. Lee, and S.-H. Lee, "Apoptosis in the osteonecrosis of the femoral head," *Clinics in Orthopedic Surgery*, vol. 2, no. 4, pp. 250–255, 2010.
- [8] A. W. Eberhardt, A. Yeager-Jones, and H. C. Blair, "Regional trabecular bone matrix degeneration and osteocyte death in femora of glucocorticoid-treated rabbits," *Endocrinology*, vol. 142, no. 3, pp. 1333–1340, 2001.
- [9] E. Rojas, R. G. Carlini, P. Clesca et al., "The pathogenesis of osteodystrophy after renal transplantation as detected by early alterations in bone remodeling," *Kidney International*, vol. 63, no. 5, pp. 1915–1923, 2003.
- [10] F. G. Blankenberg, "In vivo detection of apoptosis," *Journal of Nuclear Medicine*, vol. 49, supplement 2, no. 6, pp. 81S–95S, 2008.
- [11] H. H. Boersma, B. L. J. H. Kietselaer, L. M. L. Stolk et al., "Past, present, and future of annexin A5: from protein discovery to clinical applications," *Journal of Nuclear Medicine*, vol. 46, no. 12, pp. 2035–2050, 2005.
- [12] J. Taki, T. Higuchi, A. Kawashima et al., "Effect of postconditioning on myocardial  $^{99m}\text{Tc}$ -Annexin-V uptake: comparison with ischemic preconditioning and caspase inhibitor treatment," *Journal of Nuclear Medicine*, vol. 48, no. 8, pp. 1301–1307, 2007.
- [13] T. Doue, K. Ohtsuki, K. Ogawa et al., "Cardioprotective effects of erythropoietin in rats subjected to ischemia-reperfusion injury: assessment of infarct size with  $^{99m}\text{Tc}$ -Annexin V," *Journal of Nuclear Medicine*, vol. 49, no. 10, pp. 1694–1700, 2008.
- [14] B. L. J. H. Keitselaer, C. P. M. Reutelingsperger, H. H. Boersma et al., "Noninvasive detection of programmed cell loss with  $^{99m}\text{Tc}$ -labeled Annexin A5 in heart failure," *Journal of Nuclear Medicine*, vol. 48, no. 4, pp. 562–567, 2007.
- [15] E. Canalis and A. M. Delany, "Mechanisms of glucocorticoid action in bone," *Annals of the New York Academy of Sciences*, vol. 966, pp. 73–81, 2002.
- [16] K. D. Harrington, W. R. Murray, S. L. Kountz et al., "Avascular necrosis of bone after renal transplantation," *Journal of Bone and Joint Surgery*, vol. 53, no. 2, pp. 203–215, 1971.
- [17] I. Vermes, C. Haanen, H. Steffens-Nakken, and C. Reutellingsperger, "A novel assay for apoptosis flow cytometric detection of phosphatidylserine expression on early apoptotic cells using fluorescein labelled Annexin V," *Journal of Immunological Methods*, vol. 184, no. 1, pp. 39–51, 1995.
- [18] F. G. Blankenberg, P. D. Katsikis, J. F. Tait et al., "Imaging of apoptosis (programmed cell death) with  $^{99m}\text{Tc}$ -Annexin V," *Journal of Nuclear Medicine*, vol. 40, no. 1, pp. 184–191, 1999.
- [19] N. Lev, E. Melamed, and D. Offen, "Apoptosis and Parkinson's disease," *Progress in Neuro-Psychopharmacology and Biological Psychiatry*, vol. 27, no. 2, pp. 245–250, 2003.
- [20] H. D'Arceuil, W. Rhine, C. A. De et al., " $^{99m}\text{Tc}$  annexin V imaging of neonatal hypoxic brain injury," *Stroke*, vol. 31, no. 11, pp. 2692–2700, 2000.
- [21] T. Z. Belhocine and F. G. Blankenberg, " $^{99m}\text{Tc}$ -Annexin A5 uptake and imaging to monitor chemosensitivity," *Methods in Molecular Medicine*, vol. 111, pp. 363–380, 2005.

## Review Article

# The Role of $^{18}\text{F}$ -FDG PET/CT and MRI in Assessing Pathological Complete Response to Neoadjuvant Chemotherapy in Patients with Breast Cancer: A Systematic Review and Meta-Analysis

Qiufang Liu, Chen Wang, Panli Li, Jianjun Liu, Gang Huang, and Shaoli Song

Department of Nuclear Medicine, Ren Ji Hospital, Shanghai Jiao Tong University, School of Medicine, 160 Pujian Road, Shanghai 200127, China

Correspondence should be addressed to Chen Wang; wangc2012@yeah.net

Received 1 November 2015; Revised 19 December 2015; Accepted 22 December 2015

Academic Editor: Seigo Kinuya

Copyright © 2016 Qiufang Liu et al. This is an open access article distributed under the Creative Commons Attribution License, which permits unrestricted use, distribution, and reproduction in any medium, provided the original work is properly cited.

**Purpose.** We performed this meta-analysis to determine the utilities of  $^{18}\text{F}$ -FDG PET/CT and MRI in assessing the pathological complete response (pCR) after neoadjuvant chemotherapy (NAC) in the same cohort of patients with breast cancer. **Methods.** Two reviewers systematically searched on PubMed, Scopus, and Springer (from the beginning of 1992 to Aug. 1, 2015) for the eligible articles. Heterogeneity, pooled sensitivity and specificity, positive likelihood ratio, negative likelihood ratio, and the summary receiver operating characteristic (SROC) curve were calculated to estimate the diagnostic efficacy of  $^{18}\text{F}$ -FDG PET/CT and MRI. **Results.** A total of 6 studies including 382 pathologically confirmed patients were eligible. The pooled sensitivity and specificity of  $^{18}\text{F}$ -FDG PET/CT were 0.86 (95% CI: 0.76–0.93) and 0.72 (95% CI: 0.49–0.87), respectively. Pooled sensitivity and specificity of MRI were 0.65 (95% CI: 0.45–0.80) and 0.88 (95% CI: 0.75–0.95), respectively. The area under the SROC curve of  $^{18}\text{F}$ -FDG PET/CT and MRI was 0.88 and 0.84, respectively. **Conclusion.** Study indicated that  $^{18}\text{F}$ -FDG PET/CT had a higher sensitivity and MRI had a higher specificity in assessing pCR in breast cancer patients. Therefore, the combined use of these two imaging modalities may have great potential to improve the diagnostic performance in assessing pCR after NAC.

## 1. Introduction

Neoadjuvant chemotherapy (NAC) has become a standard therapy for patients with locally advanced or inflammatory breast cancer these years. One of the major advantages of neoadjuvant chemotherapy is that reduction of the tumor size and downstaging of tumor burden may facilitate the successful performance of breast-conserving surgery instead of mastectomy [1, 2]. In addition, it can also evaluate the therapy response to find the right time to do the operation and adjust the treatment plan in case of an unfavorable tumor response at an early stage [3]. Results from several studies have demonstrated superior disease-free survival and overall survival in patients who achieve a pCR (pathological complete response) [4, 5]. Hence, achieving pCR is an important treatment objective for patients with breast cancer.

However, we cannot accurately observe the pCR until the definitive breast surgery, and this will always lead to deficient or excessive chemotherapy and inappropriate surgery decision-making for patients before surgery. Therefore, to find an effective method to evaluate the pCR and to avoid unnecessary surgery option before surgery is crucial in the management of these patients.

Noninvasive imaging tools that could monitor the response to NAC are particularly attractive. Magnetic resonance imaging (MRI) and  $^{18}\text{F}$ -fluorodeoxyglucose positron emission tomography/computed tomography ( $^{18}\text{F}$ -FDG PET/CT) are increasingly being used to screen and monitor the response to NAC in breast cancer [6, 7]. In case of locally advanced breast cancer, MRI has the potential to select those patients that are eligible for conservative surgical treatment after NAC [8, 9]. In addition, as noted by Buchbender

and colleagues, PET/MRI with lower radiation exposure and joining all the benefits of morphologic and functional MRI information and metabolic PET information may be most useful in setting of evaluation for suspected tumor recurrence, response to neoadjuvant therapy, and prognosis [10]. But the fact is that PET/MRI has not been widely used in clinical practice.  $^{18}\text{F}$ -FDG PET/CT and MRI in predicting pCR had been previously reported [7, 11]. Due to different types of pathology and sample sizes used in each study, the diagnostic performance of  $^{18}\text{F}$ -FDG PET/CT and MRI has varied dramatically in breast cancer [12–14]. More importantly, most published articles evaluated the two modalities separately, not in the same group of patients. Thus, we conducted this meta-analysis to evaluate the overall diagnostic performance of  $^{18}\text{F}$ -FDG PET/CT and MRI in assessing pCR after NAC in the same cohort of patients with breast cancer.

## 2. Methods

**2.1. Literature Search.** We searched on PubMed, Scopus, and Springer (from the beginning of 1992 to Aug. 1, 2015), using “positron emission tomography OR positron emission tomography/computed tomography OR PET OR PET/CT OR PET-CT”, “breast neoplasm OR breast carcinoma OR breast cancer OR breast tumor OR breast tumor”, “response OR prediction”, and “MR OR MRI” as keywords. Certain filters were used for EMBASE according to inclusion criteria described in the following. Two reviewers independently screened titles and abstracts to select potential articles and then further examined full text articles of all potentially eligible citations. We also screened the reference list of retrieved studies for any additional publications.

**2.2. Eligibility Criteria.** The inclusion criteria were as follows: (1) patients should receive both  $^{18}\text{F}$ -FDG PET/CT scan and MRI examination before and during (after) NAC; (2) studies should be prospective or retrospective; (3) at least 10 patients were included in the article; (4) the studies should contain raw data, such as TP, FP, TN, and FN; (6) the gold standard of pCR should be complete absence of residual invasive tumor cells irrespective of carcinoma in situ or have no residual tumors and no metastatic lymph nodes; (7) for MRI assessment, complete response (CR) could be defined as having no significant enhancement on postchemotherapy MR images or at least a 30% decrease in the maximal diameter ( $D_{\max}$ ) or volume of the tumor; (8) PET/CT assessment parameters could be SUV or  $\text{SUV}_{\max}$  or pSUV. CR was defined as having completely no  $^{18}\text{F}$ -FDG uptake of the tumor or at least a reduction of 50% in the SUV or  $\text{SUV}_{\max}$  or pSUV compared with pre-NAC. The criteria were confirmed by two other reviewers (L. P, S. S). Duplicated articles, reviews, case reports, conference abstracts, animals, and cells studies and other nonrelated articles were excluded.

**2.3. Quality Assessment of the Studies.** Two reviewers assessed methodological quality of eligible studies independently by

using the QUADAS-2 (quality assessment of diagnosis accuracy study), which is a newly revised quality assessment tool specifically developed for systematic reviews of diagnostic accuracy studies [15]. It contains 4 aspects: patient selection, index test, reference standard, and flow and timing. Each domain was assessed in terms of the risk of bias, and the first three were also assessed in terms of concerns regarding applicability. Signaling questions are used to classify studies as having high, low, or unclear risk. Reasons for classifying some articles into high risk categories were as follows: the criteria were not clear, patients were not collected in consecutive order, the study did not indicate the parameters, images were not explained blind to pathology, inaccurate reference standard was used to classify the patients, and not all the patients were included in analysis in the study.

**2.4. Data Extraction.** For each eligible study, we extracted the following information: first author, county, year of publication, patients’ demographic and clinical characteristics, therapeutic interventions, scan time of  $^{18}\text{F}$ -FDG PET/CT and MRI, reference standard, and number of responders and nonresponders results. True positive (TP), false positive (FP), false negative (FN), and true negative (TN) were obtained from the  $^{18}\text{F}$ -FDG PET/CT and MRI scan results after they had been compared with the pathological results. Data extraction was done independently by two reviewers, and in case of any discrepancies, consensus was reached to solve them.

**2.5. Data Synthesis and Statistical Analysis.** For each study, a 2-by-2 contingency table was constructed to classify patients into 1 of 4 groups: true positives, true negatives, false positives, and false negatives. By using the tables, we calculated the true-positive rate (TPR; sensitivity), the false-positive rate (FPR;  $1 - \text{specificity}$ ), the positive predictive value (PPV), and the negative predictive value (NPV).

The heterogeneity among different studies was analyzed using Chi-squared test. And it was assessed by forest plot where  $Q$  and  $I^2$  statistics were presented. If there was heterogeneity, which was defined as  $I^2 > 50\%$ , the random effects model (REM) was selected; conversely, the fixed effects model (FEM) was selected. Threshold effect was an important source of heterogeneity. To judge whether the threshold effect exists, the Spearman correlation coefficients (between the logit of sensitivity and logit of specificity) for PET/CT and MRI were calculated. If  $P > 0.05$ , there was no threshold effect. And the forest plot and summary receiver operating characteristic (SROC) curve were drawn using the bivariate mixed effects models [16]. The area under the curve (AUC) of the SROC was calculated to measure the performance of  $^{18}\text{F}$ -FDG PET/CT and MRI. We also calculated the Youden index ( $*Q$ ), which is the best statistical method to reflect the diagnostic value [17]. Then  $Z$ -test was performed to find whether the sensitivity, specificity, and  $*Q$  index of one modality are significantly different from the other one. All analyses were carried out using Stata 12.0 and Meta-DiSc 14.0.

The publication bias of all included studies was analyzed by using “Deek” funnel plot. Statistical calculation and

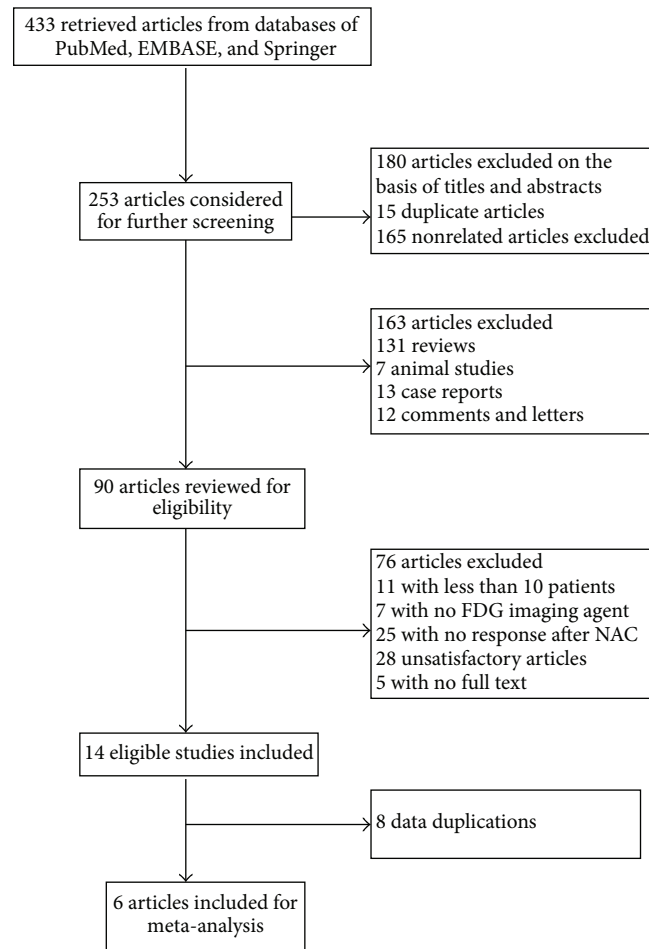


FIGURE 1: Flowchart of the literature search in the meta-analysis.

analysis were performed using Stata 12.0 (StataCorp, College Station, TX, USA).

### 3. Results

**3.1. Study Selection.** Systematic search yielded a total of 433 studies from the databases of PubMed, EMBASE, and Springer. After reviewing the titles and abstracts, 90 articles were considered as potential eligible candidates for inclusion. After in-depth reading, we excluded 76 articles since they have not met our eligibility criteria. Of the remaining 14 eligible studies, there were 8 data duplications. Thus, we have included 6 articles in our current meta-analysis [18–23]. A diagram schematizing the selection process is presented in Figure 1.

**3.2. Study Description and Patients Characteristics.** Table 1 showed that a total of 382 patients were included, and within all studies included, there were 1 from the USA, three from Korea, one from Japan, and 1 from Netherlands. Of the 6 articles, three were prospective studies and the rest of them were retrospective. The measuring parameters of  $^{18}\text{F}$ -FDG PET/CT and MRI were varied. For  $^{18}\text{F}$ -FDG PET/CT, five

of the 6 included articles chose  $\text{SUV}_{\max}$  [18, 20–23]; one study used peak-standardized uptake values (pSUV) within the ROIs [19]. For MRI, five studies measured the diameter of tumor while 1 study analyzed the data extracted from dynamic gadolinium concentration curves [18–23]. All the 6 articles used pathologic response as the golden standard [18–23]. Additionally, most of them defined pCR as “no recognizable invasive tumor cells were encountered.” Details of the 6 studies were shown in Table 2. One of the included studies has evaluated diagnostic value of ultrasound, PET/CT, MRI, or CT on predicting pCR after performing NAC on breast cancer patients, and we only extracted data of PET/CT and MRI for our meta-analysis [19].

**3.3. Quality Assessment.** The detailed information and scores regarding the quality assessment are displayed in Figure 2. In general, the results of QUADAS-2 tool showed that the qualities of included studies were satisfying and eligible.

**3.4. Heterogeneity Test.** The results showed that there were statistical heterogeneity of  $^{18}\text{F}$ -FDG PET/CT (sensitivity,  $Q$  value = 8.89,  $I^2$  = 43.77%; specificity,  $Q$  value = 59.30,  $I^2$  = 91.57%) and MRI (sensitivity,  $Q$  value = 19.55,  $I^2$  = 74.43%;

TABLE I: Characteristics of included studies for detecting pathologic response to neoadjuvant chemotherapy.

Author	County	Year	Study design	Number of patients	Mean age	Type of NAC	Cycles of NAC	Evaluation time	Endpoint	pCR/npCR	Evaluation index	Sen.
Pengel et al. [23]	Netherlands	2014	Pro.	93	47.8	Trastuzumab-based regimen	3 or 6	B/A (1 or 3 cycles)	pCR	43/50	MRI PET/CT	0.465 0.860
Kim et al. [22]	Korea	2014	Retro.	59	46.6	NR	3 or 6	B/A (3 or 6 cycles)	Miller and Payne system	34/22 23/15	MRI PET/CT	0.912 0.913
Tateishi et al. [21]	Japan	2012	Retro.	142	57	5-Fluorouracil, epirubicin, cyclophosphamide, and so forth	4	B/A (2 cycles)	pCR	24/118	MRI PET/CT	0.50 0.667
Park et al. [20]	Korea	2011	Retro.	32	45	Doxorubicin and docetaxel	3 or 6	B/A (18–22 days)	pCR	8/24	MRI PET/CT	0.625 1
Choi et al. [19]	Korea	2010	Pro.	41	45.1	Adriamycin and cyclophosphamide or docetaxel	3 or 8	B/A (3 or 8 cycles)	pCR	7/34	MRI PET/CT	0.714 0.857
Chen et al. [18]	USA	2004	Pro.	15	44	Anthracycline-based regimen	NR	B/A	pCR	10/6	MRI PET/CT	0.333 0.90

NR: not reported.

B/A: before or after the NAC.

pCR: pathology complete response.

Pro.: prospect. Retro.: retrospect.

TABLE 2: Characteristics of the patients and explanation method of the two evaluating methods (<sup>18</sup>F-FDG PET/CT and MRI).

Author	County	Year	Initial clinical stage	Histology subtype	Receptor status	Parameter of PET/CT	Parameter of MRI	Reconstruction or not	Image interpretation	Cut-off value of PET/CT	Cut-off value of MRI
Pengel et al. [23]	Netherlands	2014	II (49)	IDC (85)	HER-2(+)(25)	ROI + SUV <sub>max</sub>	ROI + diameter	Yes	NR	Reduction > 50%	Reduction > 75% (D)
			III (41)	ILC (7)	ER(+)/PR(-) (4)						
			IVa (3)	Others (1)	Triple(-) (28)						
Kim et al. [22]	Korea	2014	II (24)	IDC (54)	NR	ROI + SUV <sub>max</sub>	ROI + diameter	Yes	Blind	Reduction > 60.1%	Reduction > 50% (D)
			III (33)	ILC (1)							
			IVa (2)	MC (1)							
Tateishi et al. [21]	Japan	2012	Ia (9)	IDC (131)	ER(+) (100)	ROI + SUV <sub>max</sub>	ROI + Kep	Yes	NR	Reduction > 50%	Reduction > 30% (D)
			II (95)	ILC (11)	PR(+) (82)						
			III (38)		HER-2(+)(111)						
Park et al. [20]	Korea	2011	NR	IDC (31)	ER(+) (14)	ROI + SUV <sub>max</sub>	ROI + diameter	Yes	Blind	Reduction > 50%	Reduction > 30% (D)
				MC (1)	PR(+) (13)						
				IDC (36)	ER(+) (19)						
Choi et al. [19]	Korea	2010	II, III	ILC (2)	PR(+) (15)	ROI + pSUV	ROI + diameter	NR	Blind	Reduction > 50%	Reduction > 30% (D)
				MC (1)	HER-2(+)(10)						
				Other (2)							
Chen et al. [18]	USA	2004	LABC	IDC (12)	ER(+) (12)	ROI + SUV <sub>max</sub>	ROI + diameter	Yes	Blind	Reduction > 50%	Reduction > 30% (D)
				ILC (3)	PR(+) (11)						
				MC (1)	HER-2(+)(2)						

LABC: local advanced breast cancer.  
 IDC: invasive ductal carcinomas.  
 ILC: invasive lobular carcinomas.  
 MC: metaplastic carcinoma.  
 ER: estrogen receptor.  
 PR: progesterone receptor.  
 ROI: region of interest.  
 D: diameter.  
 V: volume.  
 NR: not reported.

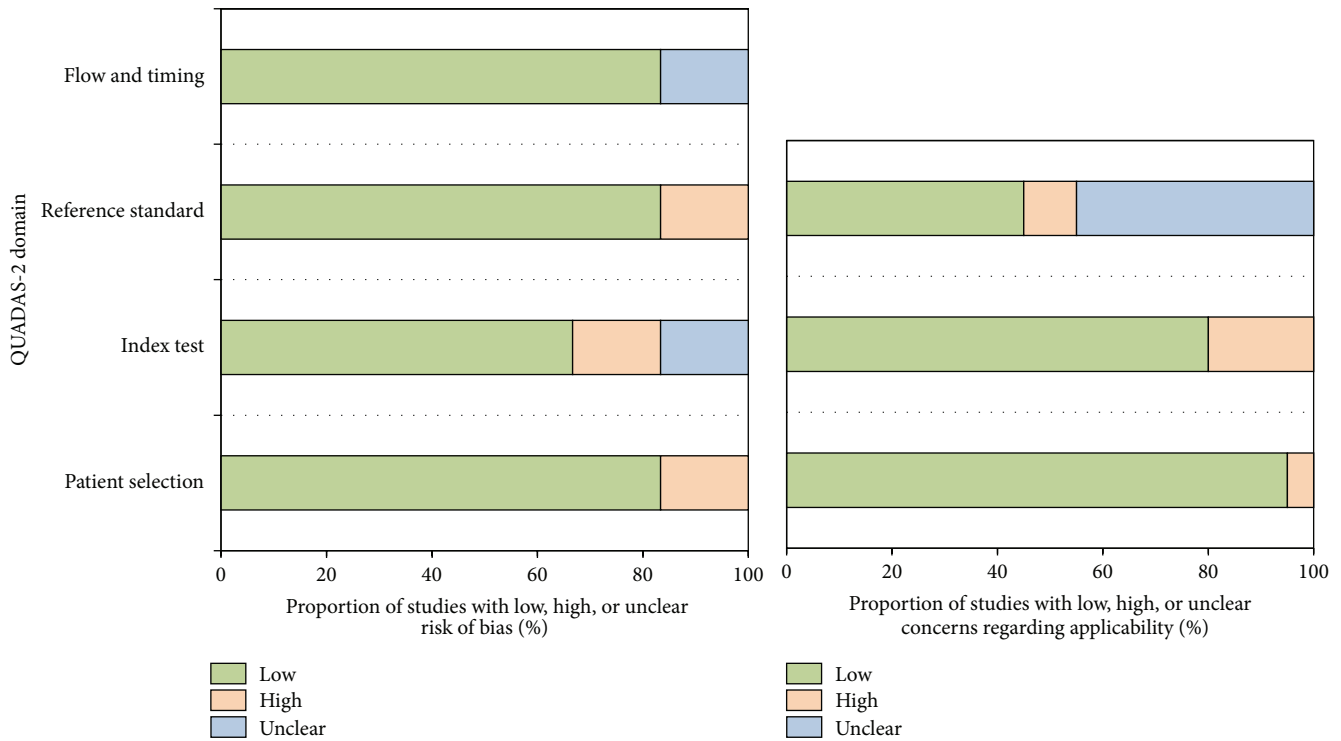


FIGURE 2: Proportion of studies with low, high, or unclear risk of bias. Proportion of studies with low or unclear concerns regarding applicability.

specificity,  $Q$  value = 34.59,  $I^2 = 85.54\%$ ) (Figures 3 and 4). Considering the heterogeneity indicated by  $I^2$ , bivariate mixed effects model was chosen to synthesize the ROC curves.

The Spearman correlation coefficient and  $P$  value of PET/CT and MRI were 0.086 ( $P = 0.872$ ,  $P > 0.05$ ) and  $-0.314$  ( $P = 0.544$ ,  $P > 0.05$ ), respectively. These results showed that there were no threshold effects in this meta-analysis.

The publication bias was shown in Figure 5. The publication bias of both  $^{18}\text{F}$ -FDG PET/CT and MRI was insignificant ( $P = 0.91$ ,  $P = 0.79$ , resp.). These results indicated that there was no significant publication bias.

**3.5. Performance of  $^{18}\text{F}$ -FDG PET/CT and MRI in Assessing Response to Preoperative NAC.** The pooled sensitivity of  $^{18}\text{F}$ -FDG PET/CT and MRI was 0.86 (95% CI, 0.76–0.93) and 0.65 (95% CI, 0.45–0.80), respectively. The sensitivity of  $^{18}\text{F}$ -FDG PET/CT was higher than that of MRI ( $P < 0.05$ ). And the specificity of  $^{18}\text{F}$ -FDG PET/CT and MRI was 0.72 (95% CI, 0.49–0.87) and 0.88 (95% CI, 0.75–0.95), respectively (Figures 3 and 4). The specificity of MRI was higher than that of  $^{18}\text{F}$ -FDG PET/CT ( $P < 0.05$ ). For  $^{18}\text{F}$ -FDG PET/CT, positive likelihood ratio, negative likelihood ratio, and diagnostic odds ratio were 3.1 (95% CI, 1.6–5.9), 0.19 (95% CI, 0.11–0.32), and 16 (95% CI, 7–37), respectively. While for MRI, positive likelihood ratio, negative likelihood ratio, and diagnostic odds ratio were 5.6 (95% CI, 2.5–0.91), 0.40 (95% CI, 0.24–0.65), and 14 (95% CI, 5–40), respectively.

SROC curves showed that the AUC of  $^{18}\text{F}$ -FDG PET/CT and MRI were 0.88 (95% CI, 0.85–0.91) and 0.84 (95% CI, 0.80–0.87), respectively (Figure 6). The Youden index ( $*Q$ ) estimates for  $^{18}\text{F}$ -FDG PET/CT and MRI were 0.82 and 0.77, respectively. And the  $*Q$  index of  $^{18}\text{F}$ -FDG PET/CT was higher than that of MRI ( $P < 0.05$ ).

#### 4. Discussion

Breast cancer response to NAC has traditionally been assessed by conventional imaging modalities such as mammogram and ultrasound. These anatomical imaging modalities sometimes have difficulties in differentiating fibrosis from residual tumors; thus they are of limited use for monitoring the treatment response. Nowadays,  $^{18}\text{F}$ -FDG PET/CT and enhanced-MRI are two imaging modalities mostly used in clinical practice.  $^{18}\text{F}$ -FDG PET/CT can differentiate changes in tumor glucose metabolism before morphologic changes. The decrease in  $^{18}\text{F}$ -FDG uptakes in tumors after chemotherapy is an indicator to assess the treatment response. Enhanced-MRI can provide information on lesion microvasculature and depict changes in the physiologic characteristics of tumors. Several studies had addressed the role of  $^{18}\text{F}$ -FDG PET/CT and MRI in assessing the early response of breast tumors to chemotherapy separately in different cohort patients.

In this study, we systematically calculated the predictive performance of  $^{18}\text{F}$ -FDG PET/CT and MRI in the same cohort of patients with breast cancer. The results showed that

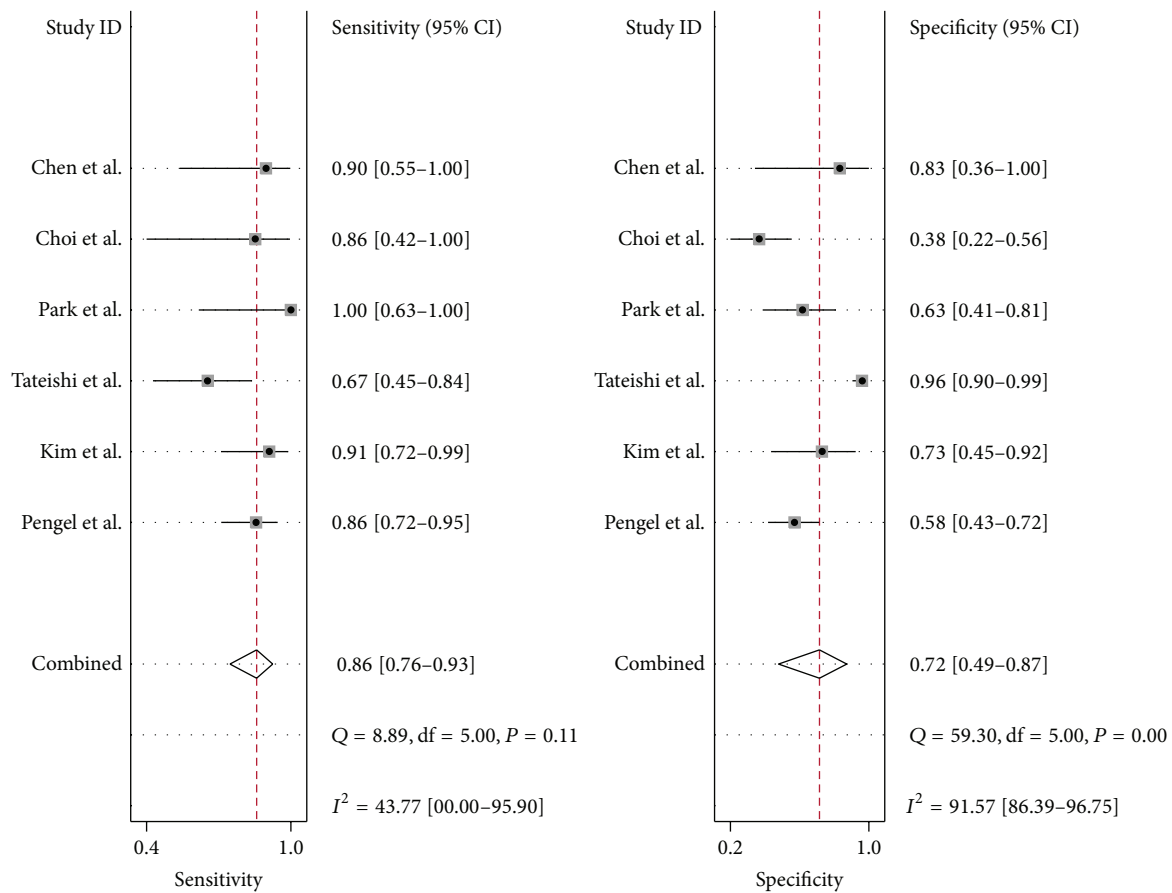


FIGURE 3: Forest plot of the <sup>18</sup>F-FDG PET/CT of 6 included studies. The size of the square plotting reflects the study weight. Horizontal lines are the 95% confidence intervals.

<sup>18</sup>F-FDG PET/CT had a higher sensitivity when compared with MRI. This may contribute to the following reasons: firstly, <sup>18</sup>F-FDG PET/CT exhibited unique advantages to offer an earlier metabolic response prediction than morphologic images. But <sup>18</sup>F-FDG is a nonspecific tracer and also accumulates in sites of inflammation. Chemotherapy induced therapeutic effects often caused apoptosis, necrosis, and inflammation [24, 25]. That caused false positive in <sup>18</sup>F-FDG PET imaging and made it difficult in image interpretation after NAC. Secondly, for most breast cancer patients with advanced stages, chemotherapy always caused tumor shrinkage rather than disappearing. When the reduction rate of  $D_{max}$  reached the specified threshold value or the lesion was no longer enhanced or completely gone, it was a complete response on MRI.

For MRI, our study results were similar in conclusion with the study by Wu et al. (sen.: 68%, spe.: 91% versus sen.: 65%, spe.: 88%) [11]. In another meta-analysis study focused on residual detection of breast cancer after NAC, the sensitivity and specificity of contrast enhanced-MRI were 54% and 87%, respectively [26]. Compared with these two similar studies, our results showed higher sensitivity and specificity [27, 28]. SUV cut-off value may be another significant factor influencing the results. Mghanga et al. studied the diagnostic performance of PET/CT in breast

cancer patients who underwent NAC. Study results showed a lower sensitivity (80.5% versus 86%) and a higher specificity (78.8% versus 72%) compared with ours [28]. Causes of the difference mainly because of SUV cut-off value in their study ranged from 40% to 88%, but ours were not less than 50%.

The integrated whole-body PET/MRI that is of lower radiation exposure and can provide high-resolution anatomical, morphological, molecular information particularly for soft tissues has attracted more and more attention in recent years. But there is limited data which has been published on the role of PET/MRI in the assessment of response after the NAC. And PET/MRI imaging in oncologic patient population is mainly applied to cover single organ region or whole-body tumor staging, restaging, and metastasis screening [29, 30]. For the high NPV (PET component) and the high specificity (MRI component), PET/MRI hold the promise to improve therapy-response evaluation [10]. For now, prospective studies are needed to demonstrate if there is improved diagnostic accuracy and cost-effectiveness of combined <sup>18</sup>F-FDG PET/MR compared to <sup>18</sup>F-FDG PET/CT.

As PET/CT has a sensitivity of 86% and MRI has a specificity of 88%, the combined use of these two imaging modalities may have great potential to improve the diagnostic performance in assessing pCR after NAC. But in clinical practice, there were cases that the results of FDG PET/CT

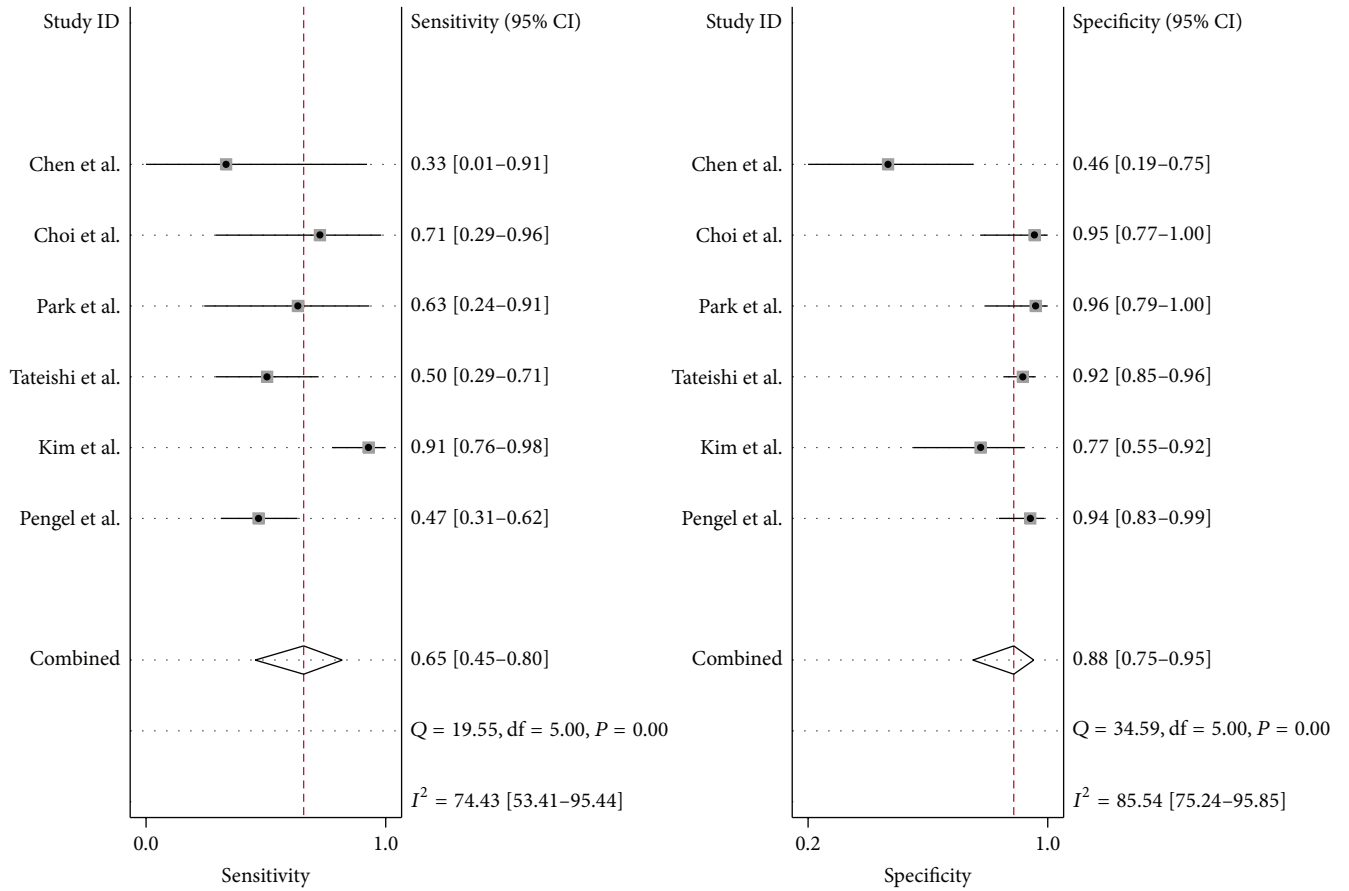


FIGURE 4: Forest plot of the MRI of 6 included studies. The size of the square plotting reflects the study weight. Horizontal lines are the 95% confidence intervals.

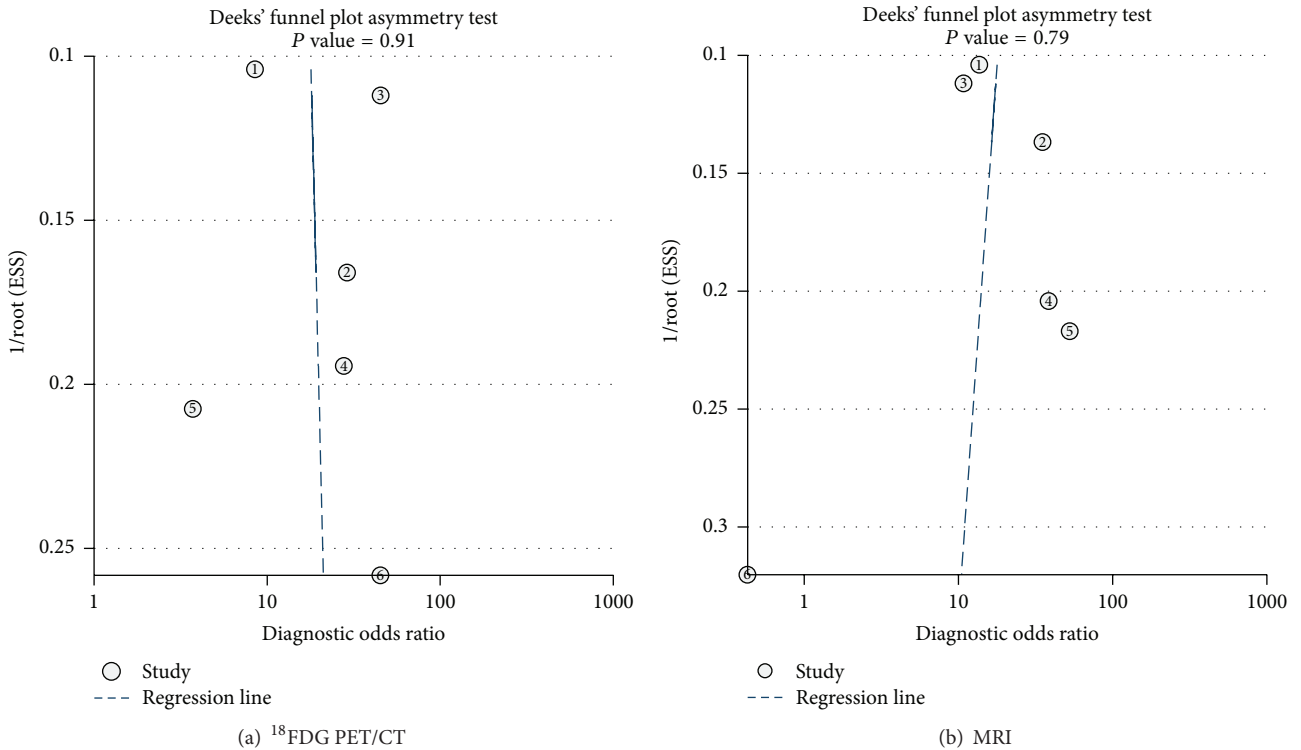


FIGURE 5: (a) Publication bias of <sup>18</sup>F-FDG PET/CT using Deek's funnel plot. (b) Publication bias of MRI using Deek's funnel plot.

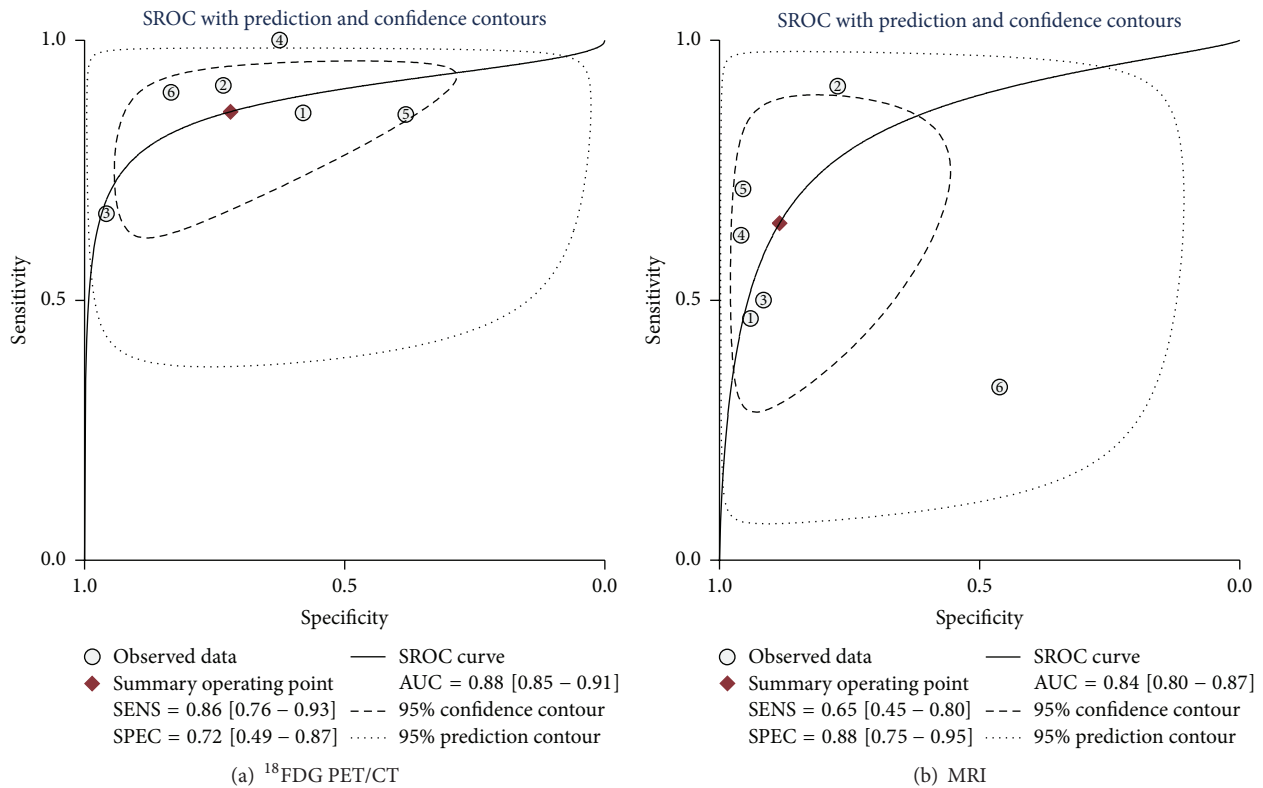


FIGURE 6: (a) SROC for NAC response prediction in primary breast cancer by <sup>18</sup>F-FDG PET/CT. (b) SROC for NAC response prediction in primary breast cancer by MRI.

and MRI may be different. Considering that PET/CT has higher sensitivity and higher accuracy in TNM staging in clinical practice, PET/CT results may be the most often used information in determining the resection margin.

There were still some limitations of our study. First, considering the limited number of the published studies for MRI and <sup>18</sup>F-FDG PET/CT in the same cohort of patients, the small cohort of patients for the two imaging modalities may cause heterogeneity. Second, the heterogeneity among studies might also come from various types and stages of breast cancer which are included in our meta-analysis. Finally, we acknowledge other potential limitations including selector bias, which was brought about by selection, publication, and verification of the studies.

### 5. Conclusion

Study indicated that <sup>18</sup>F-FDG PET/CT had a higher sensitivity and MRI had a higher specificity in assessing pCR in breast cancer patients. Therefore, the combined use of these two imaging modalities may have great potential to improve the diagnostic performance in assessing pCR after NAC.

### Conflict of Interests

The paper is approved by all authors and the authors do not have any conflict of interests.

### References

- [1] S. V. Liu, L. Melstrom, K. Yao, C. A. Russell, and S. F. Sener, "Neoadjuvant therapy for breast cancer," *Journal of Surgical Oncology*, vol. 101, no. 4, pp. 283–291, 2010.
- [2] P. Rastogi, M. E. Buyse, S. M. Swain et al., "Concurrent bevacizumab with a sequential regimen of doxorubicin and cyclophosphamide followed by docetaxel and capecitabine as neoadjuvant therapy for HER2- locally advanced breast cancer: a phase II trial of the NSABP foundation research group," *Clinical Breast Cancer*, vol. 11, no. 4, pp. 228–234, 2011.
- [3] D. Groheux, S. Giacchetti, M. Espié, D. Rubello, J.-L. Moretti, and E. Hindié, "Early monitoring of response to neoadjuvant chemotherapy in breast cancer with <sup>18</sup>F-FDG PET/CT: defining a clinical aim," *European Journal of Nuclear Medicine and Molecular Imaging*, vol. 38, no. 3, pp. 419–425, 2011.
- [4] L. J. Esserman, D. A. Berry, M. C. U. Cheang et al., "Chemotherapy response and recurrence-free survival in neoadjuvant breast cancer depends on biomarker profiles: results from the I-SPY 1 TRIAL (CALGB 150007/150012; ACRIN 6657)," *Breast Cancer Research and Treatment*, vol. 132, no. 3, pp. 1049–1062, 2012.
- [5] G. von Minckwitz, M. Untch, J.-U. Blohmer et al., "Definition and impact of pathologic complete response on prognosis after neoadjuvant chemotherapy in various intrinsic breast cancer subtypes," *Journal of Clinical Oncology*, vol. 30, no. 15, pp. 1796–1804, 2012.
- [6] H. J. Shin, H.-M. Baek, J.-H. Ahn et al., "Prediction of pathologic response to neoadjuvant chemotherapy in patients with breast

- cancer using diffusion-weighted imaging and MRS,” *NMR in Biomedicine*, vol. 25, no. 12, pp. 1349–1359, 2012.
- [7] O. Humbert, A. Cochet, B. Coudert et al., “Role of positron emission tomography for the monitoring of response to therapy in breast cancer,” *Oncologist*, vol. 20, no. 2, pp. 94–104, 2015.
  - [8] H. C. Le-Petross and N. Hylton, “Role of breast MR imaging in neoadjuvant chemotherapy,” *Magnetic Resonance Imaging Clinics of North America*, vol. 18, no. 2, pp. 249–258, 2010.
  - [9] M. G. Heldahl, S. Lundgren, L. R. Jensen, I. S. Gribbestad, and T. F. Bathen, “Monitoring neoadjuvant chemotherapy in breast cancer patients: improved MR assessment at 3 T?” *Journal of Magnetic Resonance Imaging*, vol. 34, no. 3, pp. 547–556, 2011.
  - [10] C. Buchbender, T. A. Heusner, T. C. Lauenstein, A. Bockisch, and G. Antoch, “Oncologic PET/MRI, part 1: tumors of the brain, head and neck, chest, abdomen, and pelvis,” *Journal of Nuclear Medicine*, vol. 53, no. 6, pp. 928–938, 2012.
  - [11] L.-M. Wu, J.-N. Hu, H.-Y. Gu, J. Hua, J. Chen, and J.-R. Xu, “Can diffusion-weighted MR imaging and contrast-enhanced MR imaging precisely evaluate and predict pathological response to neoadjuvant chemotherapy in patients with breast cancer?” *Breast Cancer Research and Treatment*, vol. 135, no. 1, pp. 17–28, 2012.
  - [12] C. E. Loo, M. E. Straver, S. Rodenhuis et al., “Magnetic resonance imaging response monitoring of breast cancer during neoadjuvant chemotherapy: relevance of breast cancer subtype,” *Journal of Clinical Oncology*, vol. 29, no. 6, pp. 660–666, 2011.
  - [13] M. E. Straver, C. E. Loo, E. J. T. Rutgers et al., “MRI-model to guide the surgical treatment in breast cancer patients after neoadjuvant chemotherapy,” *Annals of Surgery*, vol. 251, no. 4, pp. 701–707, 2011.
  - [14] B. B. Koolen, K. E. Pengel, J. Wesseling et al., “Sequential <sup>18</sup>F-FDG PET/CT for early prediction of complete pathological response in breast and axilla during neoadjuvant chemotherapy,” *European Journal of Nuclear Medicine Molecular Imaging*, vol. 41, no. 1, pp. 32–40, 2014.
  - [15] P. F. Whiting, A. W. S. Rutjes, M. E. Westwood et al., “QUADAS-2: a revised tool for the quality assessment of diagnostic accuracy studies,” *Annals of Internal Medicine*, vol. 155, no. 8, pp. 529–536, 2011.
  - [16] J. B. Reitsma, A. S. Glas, A. W. S. Rutjes, R. J. P. M. Scholten, P. M. Bossuyt, and A. H. Zwiderman, “Bivariate analysis of sensitivity and specificity produces informative summary measures in diagnostic reviews,” *Journal of Clinical Epidemiology*, vol. 58, no. 10, pp. 982–990, 2005.
  - [17] J. Zamora, V. Abraira, A. Muriel, K. Khan, and A. Coomarasamy, “Meta-DiSc: a software for meta-analysis of test accuracy data,” *BMC Medical Research Methodology*, vol. 6, article 31, 2006.
  - [18] X. Chen, M. O. Moore, C. D. Lehman et al., “Combined use of MRI and PET to monitor response and assess residual disease for locally advanced breast cancer treated with neoadjuvant chemotherapy,” *Academic Radiology*, vol. 11, no. 10, pp. 1115–1124, 2004.
  - [19] J. H. Choi, H. I. Lim, S. K. Lee et al., “The role of PET CT to evaluate the response to neoadjuvant chemotherapy in advanced breast cancer: comparison with ultrasonography and magnetic resonance imaging,” *Journal of Surgical Oncology*, vol. 102, no. 5, pp. 392–397, 2010.
  - [20] J. S. Park, W. K. Moon, C. Y. Lyou, N. Cho, K. W. Kang, and J.-K. Chung, “The assessment of breast cancer response to neoadjuvant chemotherapy: comparison of magnetic resonance imaging and <sup>18</sup>F-fluorodeoxyglucose positron emission tomography,” *Acta Radiologica*, vol. 52, no. 1, pp. 21–28, 2011.
  - [21] U. Tateishi, M. Miyake, T. Nagaoka et al., “Neoadjuvant chemotherapy in breast cancer: prediction of pathologic response with PET/CT and dynamic contrast-enhanced MR imaging—prospective assessment,” *Radiology*, vol. 263, no. 1, pp. 53–63, 2012.
  - [22] T. Kim, D. K. Kang, Y.-S. An et al., “Utility of MRI and PET/CT after neoadjuvant chemotherapy in breast cancer patients: correlation with pathological response grading system based on tumor cellularity,” *Acta Radiologica*, vol. 55, no. 4, pp. 399–408, 2014.
  - [23] K. E. Pengel, B. B. Koolen, C. E. Loo et al., “Combined use of <sup>18</sup>F-FDG PET/CT and MRI for response monitoring of breast cancer during neoadjuvant chemotherapy,” *European Journal of Nuclear Medicine and Molecular Imaging*, vol. 41, no. 8, pp. 1515–1524, 2014.
  - [24] M. S. Kwong, G. G. Chung, L. J. Horvath et al., “Postchemotherapy MRI overestimates residual disease compared with histopathology in responders to neoadjuvant therapy for locally advanced breast cancer,” *Cancer Journal*, vol. 12, no. 3, pp. 212–221, 2006.
  - [25] F. Denis, A. V. Desbiez-Bourcier, C. Chapiron, F. Arbion, G. Body, and L. Brunereau, “Contrast enhanced magnetic resonance imaging underestimates residual disease following neoadjuvant docetaxel based chemotherapy for breast cancer,” *European Journal of Surgical Oncology*, vol. 30, no. 10, pp. 1069–1076, 2004.
  - [26] M. L. Marinovich, N. Houssami, P. MacAskill et al., “Meta-analysis of magnetic resonance imaging in detecting residual breast cancer after neoadjuvant therapy,” *Journal of the National Cancer Institute*, vol. 105, no. 5, pp. 321–333, 2013.
  - [27] Y. Wang, C. Zhang, J. Liu, and G. Huang, “Is <sup>18</sup>F-FDG PET accurate to predict neoadjuvant therapy response in breast cancer? A meta-analysis,” *Breast Cancer Research and Treatment*, vol. 131, no. 2, pp. 357–369, 2012.
  - [28] F. P. Mghanga, X. Lan, K. H. Bakari, C. Li, and Y. Zhang, “Fluorine-18 fluorodeoxyglucose positron emission tomography-computed tomography in monitoring the response of breast cancer to neoadjuvant chemotherapy: a meta-analysis,” *Clinical Breast Cancer*, vol. 13, no. 4, pp. 271–279, 2013.
  - [29] C. Buchbender, V. Hartung-Knemeyer, K. Beiderwellen et al., “Diffusion-weighted imaging as part of hybrid PET/MRI protocols for whole-body cancer staging: does it benefit lesion detection?” *European Journal of Radiology*, vol. 82, no. 5, pp. 877–882, 2013.
  - [30] A. Wetter, C. Lipponer, F. Nensa et al., “Simultaneous <sup>18</sup>F choline positron emission tomography/magnetic resonance imaging of the prostate: initial results,” *Investigative Radiology*, vol. 48, no. 5, pp. 256–262, 2013.

## Research Article

# The Synthesis and Evaluations of the $^{68}\text{Ga}$ -Lissamine Rhodamine B (LRB) as a New Radiotracer for Imaging Tumors by Positron Emission Tomography

Xuena Li, Yafu Yin, Bulin Du, Na Li, and Yaming Li

Department of Nuclear Medicine, The First Hospital of China Medical University, Shenyang 110001, China

Correspondence should be addressed to Yaming Li; [yml2001@163.com](mailto:yml2001@163.com)

Received 25 November 2015; Accepted 13 January 2016

Academic Editor: James Russell

Copyright © 2016 Xuena Li et al. This is an open access article distributed under the Creative Commons Attribution License, which permits unrestricted use, distribution, and reproduction in any medium, provided the original work is properly cited.

**Purpose.** The aim of this study is to synthesize and evaluate  $^{68}\text{Ga}$ -labeled Lissamine Rhodamine B (LRB) as a new radiotracer for imaging MDA-MB-231 and MCF-7 cells induced tumor mice by positron emission tomography (PET). **Methods.** Firstly, we performed the radio synthesis and microPET imaging of  $^{68}\text{Ga}(\text{DOTA-LRB})$  in athymic nude mice bearing MDA-MB-231 and MCF-7 human breast cancer xenografts. Additionally, the evaluations of  $^{18}\text{F}$ -fluorodeoxyglucose (FDG), as a glucose metabolism radiotracer for imaging tumors in the same xenografts, have been conducted as a comparison. **Results.** The radiochemical purity of  $^{68}\text{Ga}(\text{DOTA-LRB})$  was  $>95\%$ . MicroPET dynamic imaging revealed that the uptake of  $^{68}\text{Ga}(\text{DOTA-LRB})$  was mainly in normal organs, such as kidney, heart, liver, and brain and mainly excreted from kidney. The MDA-MB-231 and MCF-7 tumors were not clearly visible in PET images at 5, 15, 30, 40, 50, and 60 min after injection of  $^{68}\text{Ga}(\text{DOTA-LRB})$ . The tumor uptake values of  $^{18}\text{F}$ -FDG were  $3.79 \pm 0.57$  and  $1.93 \pm 0.48\% \text{ID/g}$  in MDA-MB-231 and MCF-7 tumor xenografts, respectively. **Conclusions.**  $^{68}\text{Ga}(\text{DOTA-LRB})$  can be easily synthesized with high radiochemical purity and stability; however, it may be not an ideal PET radiotracer for imaging of MDR-positive tumors.

## 1. Introduction

Tumor growth depends on the energy metabolism of the supply, and the biological energy of tumor has received much attention in recent years [1, 2]. A metabolic shift from oxidative phosphorylation in the mitochondria to glycolysis in cancer was first described about 80 years ago by Warburg [3]. Increased glucose metabolism is an important feature of cancer [4]. Active glucose uptake by cancer cells constitutes the basis for  $^{18}\text{F}$ -fluorodeoxyglucose-positron emission tomography ( $^{18}\text{F}$ -FDG PET), an imaging technology commonly used in cancer diagnosis. However, the reverse Warburg effect was recently found in a human breast cancer model [5–7]. The researchers found that breast cancer cells showed a significant increase activity in mitochondria [8]. However, the development of molecular imaging probes targeting tumor mitochondria is very limited.

It has been reported that the mitochondrial potential in carcinoma cells is significantly higher than that in normal

epithelial cells [9, 10], and mitochondrial potential is negative; many organic cations are driven through these cell membranes and able to localize in the mitochondria of tumor cells [11–13]. Several studies proposed to use the  $^{64}\text{Cu}(\text{DO3A-xy-TPEP})$  and  $^{18}\text{F}$ -labeled phosphonium cations as PET radiotracers for tumor mitochondria, but they had high background in normal organs [14, 15]. Lissamine Rhodamine B (LRB) is a derivative of rhodamine, which has been used as probe for mitochondrial potentials.  $^{64}\text{Cu-LRB}$ , a radiotracer targeting tumor mitochondria for U87MG human glioma xenografts, has low radioactivity accumulation in the brain, and  $^{64}\text{Cu}$  requires high energy cyclotron for production, both of which limit the clinical application in the tumor [16].  $^{68}\text{Ga}$  is a generator-produced radionuclide, and its half-life is 67.6 min, which is produced by  $^{68}\text{Ge}/^{68}\text{Ga}$  generator; the production of  $^{68}\text{Ga}$  is not dependent on the cyclotron.

The objective of our study is to synthesize and evaluate  $^{68}\text{Ga}$ -labeled Lissamine Rhodamine B (LRB) (Figure 1) as

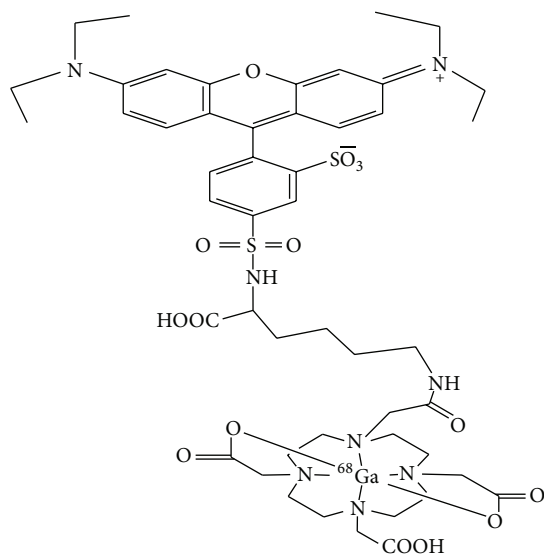


FIGURE 1: Proposed structure of  $^{68}\text{Ga}(\text{DOTA-LRB})$ .

a new radiotracer for imaging MDA-MB-231 and MCF-7 cells induced tumor mice by positron emission tomography (PET). Additionally,  $^{18}\text{F}$ -FDG, as a glucose metabolism radiotracer for imaging tumors in the same xenografts, was further evaluated as a comparison.

## 2. Materials and Methods

2-(6-(Diethylamino)-3-(diethyliminio)-3H-xanthen-9-yl)-5-(N-(2-(2-(4,7,10-tris(carboxymethyl)-1,4,7,10-tetraazacyclododecan-1-yl)acetamido)ethyl)sulfamoyl)-benzenesulfonate (DOTA-LRB) was kindly provided by Dr. Shuang Liu (School of Health Sciences, Purdue University, West Lafayette, Indiana, USA), and the method of synthesis and purification was described in the previous study [16].

**2.1. HPLC Methods.** The semiprep HPLC method used a Waters 2545+BIOSCAN Flowcount system equipped with a UV/Vis detector ( $\lambda = 254\text{ nm}$ ) and CHROM-MATRIX C-18 semiprep column (10 mm  $\times$  250 mm). The flow rate was 3 mL/min. The mobile phase was isocratic with 70% A (0.1% TFA in water) and 30% B (0.1% TFA in methanol) at 0–5 min, followed by a gradient mobile phase going from 30% B at 5 min to 80% B at 20 min, followed by a gradient mobile phase going from 80% B at 20 min to 30% B at 25 min. The radio-HPLC analysis method used a system (Waters, Inc., USA) consisting of Agilent TC-18 Chromatographic column (4.6  $\times$  250 mm, 5  $\mu\text{m}$ ), Perkinzimer online radioactivity detector, and a UV detector ( $\lambda = 254\text{ nm}$ ). The flow rate was 1 mL/min. The mobile phase was isocratic with 60% A (0.1% TFA in water) and 40% B (0.1% TFA in methanol) at 0–1 min, followed by a gradient mobile phase going from 40% B at 1 min to 90% B at 40 min, followed by a gradient mobile phase going from 90% B at 40 min to 98% B at 45 min.

**2.2.  $^{68}\text{Ga}$  Radiolabeling.**  $^{68}\text{Ga}$  was obtained from a  $^{68}\text{Ge}/^{68}\text{Ga}$  generator (Garching GmbH, Germany) eluted with 0.1 N HCl. Fresh  $^{68}\text{Ga}$  was loaded into an ion exchange column. By using a mixture of 400  $\mu\text{L}$  97.6% acetone and 0.05 M hydrochloric acid,  $^{68}\text{Ga}$  was eluted from the exchange column and added to the solution containing 10  $\mu\text{g}$  DOTA-LRB in 400  $\mu\text{L}$  0.25 M HEPES (pH 4.0); the reaction mixture was then heated at 100  $^{\circ}\text{C}$  for 20 min.

**2.3. Cancer Cell Line, Nude Mice, and Cancer Models.** The human breast cancer MDA-MB-231 and MCF-7, purchased from Shanghai Cell Bank of Chinese Academy of Sciences, were used in our experiments and preparation of animal models. The human breast cancer MDA-MB-231 and MCF-7 cells were maintained in DMEM (Dulbecco's modified Eagle's medium) (GIBCO, Inc.) supplemented with 10% fetal bovine serum (GIBCO, Inc.) with 100 units/mL streptomycin and 100 units/mL penicillin. Cells were grown in a humidified atmosphere at 37  $^{\circ}\text{C}$  with 5% carbon dioxide.

All experiments were performed using 6-week-old female athymic nude mice purchased from Shanghai Silaike Experimental Animal Co. Ltd. Athymic nude mice derived are in compliance with regulations of our institution. All animal experiments were approved by the China Medical University Animal Care and Use Committee.

Subcutaneous injection of  $5 \times 10^6$  tumor cells into the breast fat pad of female athymic nude mice generated the tumor model. When the tumor volume was 100–300  $\text{mm}^3$  (about 3–4 weeks after inoculation), the mice underwent small animal PET imaging studies.

### 2.4. MicroPET Imaging

**2.4.1.  $^{68}\text{Ga}(\text{DOTA-LRB})$  MicroPET Imaging and  $^{18}\text{F}$ -FDG MicroPET Imaging.** The tumor-bearing MDA-MB-231 ( $n = 6$ ) and MCF-7 ( $n = 6$ ) nude mice were imaged in the Inveon microPET scanner (Siemens Medical Solutions). Animals were anesthetized by isoflurane. Each tumor-bearing mouse was injected with  $\sim 100\ \mu\text{Ci}$  of  $^{68}\text{Ga}(\text{DOTA-LRB})$  via the tail vein; 10 min static scans were obtained at 5, 15, 30, 40, 50, and 60 min p.i. Each tumor-bearing mouse was injected with  $\sim 100\ \mu\text{Ci}$  of  $^{18}\text{F}$ -FDG via the tail vein; 10 min scans were acquired at 1 h after injection. The all images were reconstructed by a 3D-OSEM (three-dimensional ordered subsets expectation maximum) algorithm. The boundary was determined with the threshold of 50%. The radioactivity concentration of the tumor or normal organ was obtained from uptake values within the ROI [17].

**2.5. Statistical Analysis.** Quantitative data is expressed as mean  $\pm$  SD. Means were compared using Student's  $t$ -test.  $P < 0.05$  was considered statistically significant.

## 3. Results

**3.1. Chemistry and Radiochemistry.** The retention time of  $^{68}\text{Ga}(\text{DOTA-LRB})$  was 9.8 min. The radiochemical purity of

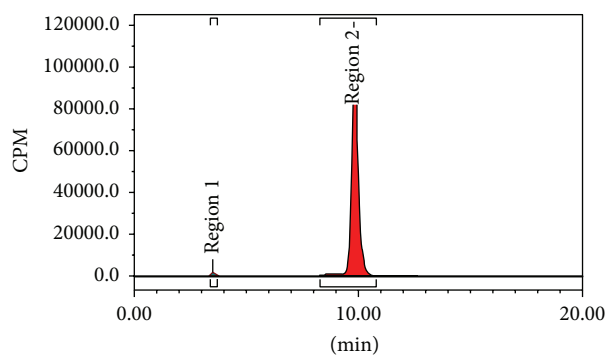


FIGURE 2: Radio-HPLC chromatogram of  $^{68}\text{Ga}(\text{DOTA-LRB})$ .

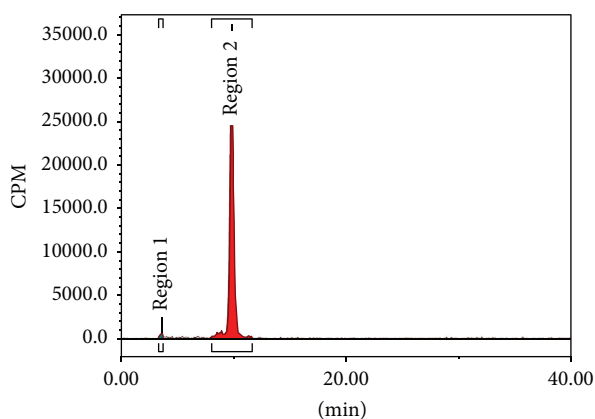


FIGURE 3: Radio-HPLC chromatogram of  $^{68}\text{Ga}(\text{DOTA-LRB})$  in PBS at  $37^\circ\text{C}$  for 2 h.

final product was 98.9% (Figure 2); it was analyzed by an analytical HPLC. The experiments in vitro demonstrated that radiochemical purity of  $^{68}\text{Ga}(\text{DOTA-LRB})$  was  $>95\%$  in PBS at  $37^\circ\text{C}$  for 2 h (Figure 3).

**3.2.  $^{68}\text{Ga}(\text{DOTA-LRB})$  MicroPET Imaging.** Figure 4 showed microPET images of MDA-MB-231 breast cancer-bearing mouse administered  $\sim 100\ \mu\text{Ci}$  of  $^{68}\text{Ga}(\text{DOTA-LRB})$  at 5, 15, 30, 40, 50, and 60 min p.i. The MDA-MB-231 tumors were not clearly visible with high contrast at all the time points examined for  $^{68}\text{Ga}(\text{DOTA-LRB})$  PET imaging.

Figure 5 showed microPET images of MCF-7 breast cancer-bearing mice administered  $\sim 100\ \mu\text{Ci}$  of  $^{68}\text{Ga}(\text{DOTA-LRB})$  at 5, 15, 30, 40, 50, and 60 min p.i. The uptake of  $^{68}\text{Ga}$ -labeled LRB was negative at all the time points.

MicroPET dynamic imaging revealed the uptake of  $^{68}\text{Ga}(\text{DOTA-LRB})$  in normal organs (kidney, heart, and liver) and the excretion from the kidney. It had very low  $^{68}\text{Ga}(\text{DOTA-LRB})$  radioactivity accumulation in the brain. The uptakes of  $^{68}\text{Ga}(\text{DOTA-LRB})$  in kidneys, liver, heart, and brain were  $4.44 \pm 2.32$ ,  $2.11 \pm 0.98$ ,  $2.17 \pm 0.90$ , and  $0.53 \pm 0.19\%$  ID/g at 30 min p.i., respectively.

**3.3.  $^{18}\text{F-FDG}$  MicroPET Imaging.** Figure 6 showed microPET images of MDA-MB-231 breast cancer-bearing mouse and

MCF-7 breast cancer-bearing mouse administered  $\sim 100\ \mu\text{Ci}$  of  $^{18}\text{F-FDG}$  at 60 min p.i. The tumor uptake values were  $3.79 \pm 0.57$  and  $1.93 \pm 0.48\%$  ID/g in MDA-MB-231 and MCF-7 breast cancer-bearing mice, respectively. The tumor uptake of  $^{18}\text{F-FDG}$  was visually higher than that of  $^{68}\text{Ga}(\text{DOTA-LRB})$ .

## 4. Discussion

Increase of mitochondrial transmembrane potential ( $\Delta\Psi_m$ ) is an important characteristic of cancer [18–20]. Molecular imaging probes based on mitochondrial transmembrane potential have attracted intensive research attention in recent years. Although many radiolabeled cationic tracers have been reported, they all need to be produced by the cyclotron.  $^{68}\text{Ga}$  is produced by  $^{68}\text{Ge}$ - $^{68}\text{Ga}$  generator.  $^{68}\text{Ga}$  is the short half-life radionuclide, which is difficult for commercial distribution. The major advantage of the generator is that it can produce continuous source of  $^{68}\text{Ga}$  independent of the cyclotron;  $^{68}\text{Ga}$ -labeled biomolecules have great advantages in clinical application [21–23].

This is the first synthesis study for  $^{68}\text{Ga}(\text{DOTA-LRB})$ , which was easily labeled with  $^{68}\text{Ga}$  and the radiochemical purity of  $^{68}\text{Ga}(\text{DOTA-LRB})$  could reach more than 95% with HPLC purification. The HPLC retention time was 9.8 min. The experiments in vitro demonstrated that  $^{68}\text{Ga}(\text{DOTA-LRB})$  was stable in PBS at  $37^\circ\text{C}$  for 2 h.

MicroPET dynamic imaging revealed that normal organs (kidney, heart, and liver) had  $^{68}\text{Ga}(\text{DOTA-LRB})$  uptake and mainly excreted from the kidney. It had very low  $^{68}\text{Ga}(\text{DOTA-LRB})$  radioactivity accumulation in the normal brain tissue. The distribution of  $^{68}\text{Ga}(\text{DOTA-LRB})$  in normal tissues was consistent with that of  $^{64}\text{Cu}(\text{DOTA-LRB})$  [16].  $^{68}\text{Ga}(\text{DOTA-LRB})$  was very low accumulation in the normal brain; it is probably because this compound is not able to cross the blood brain barrier (BBB).  $^{68}\text{Ga}(\text{DOTA-LRB})$  showed better biodistribution in normal organs in this study, compared with another report using  $^{64}\text{Cu}$ -labeled acridinium cation, which is high and prolonged liver uptake [24].

The previous study showed that the uptake of  $^{64}\text{Cu}(\text{DOTA-LRB})$  was positive in U87MG human glioma xenografts [16], whereas our study showed  $^{68}\text{Ga}(\text{DOTA-LRB})$  uptake in MDA-MB-231 and MCF-7 breast cancer cells was negative. We attributed the difference to different cell lines. The study by Dr. Liu's group with  $^{64}\text{Cu}(\text{DOTA-LRB})$  used the U87MG human glioma cell, which is negative expression of multidrug resistance (MDR) protein tumor cell [16], whereas our study used the MDA-MB-231 and MCF-7 breast cancer cell lines, which are not MRP-negative cancer cell. It was reported that the MDR had positive expression in MDA-MB-231 and MCF-7 breast cancer cells [25]. Because some cations are the substrate for MDR protein, cationic radiotracers have been clinically used for noninvasive monitoring of the multidrug resistance transport function in tumors [26, 27]. Lissamine Rhodamine B (LRB) is a member of rhodamine derivatives, which is also the substrate for MDR protein. Therefore, lower  $^{68}\text{Ga}(\text{DOTA-LRB})$  tumor uptake in the two breast cancer cells may be associated with

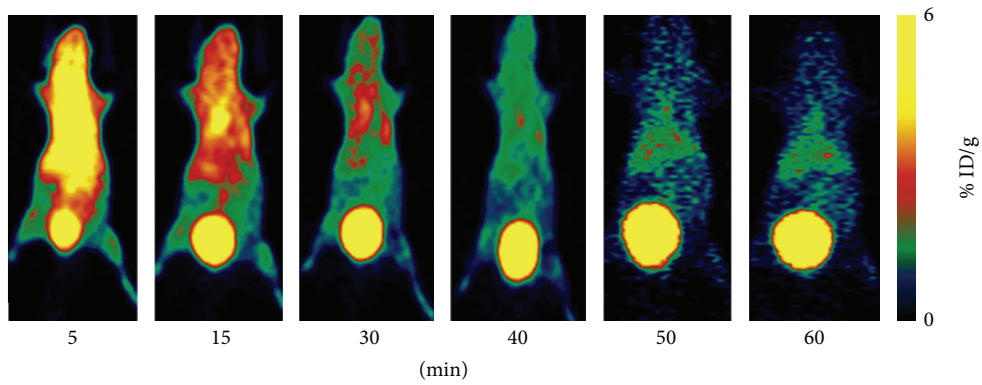


FIGURE 4: Whole-body coronal microPET images of MDA-MB-231 tumor-bearing mouse at 5, 15, 30, 40, 50, and 60 min after injection of  $\sim 100 \mu\text{Ci}$   $^{68}\text{Ga}(\text{DOTA-LRB})$ .

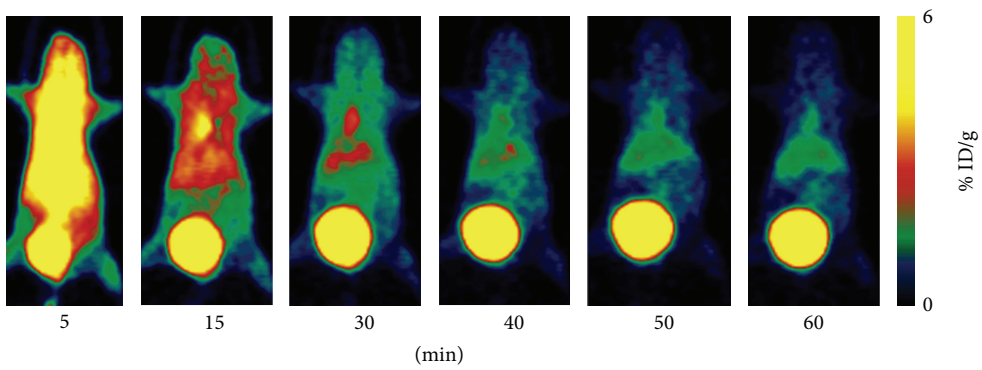


FIGURE 5: Whole-body coronal microPET images of tumor-bearing MCF-7 mouse at 5, 15, 30, 40, 50, and 60 min after injection of  $\sim 100 \mu\text{Ci}$   $^{68}\text{Ga}(\text{DOTA-LRB})$ .

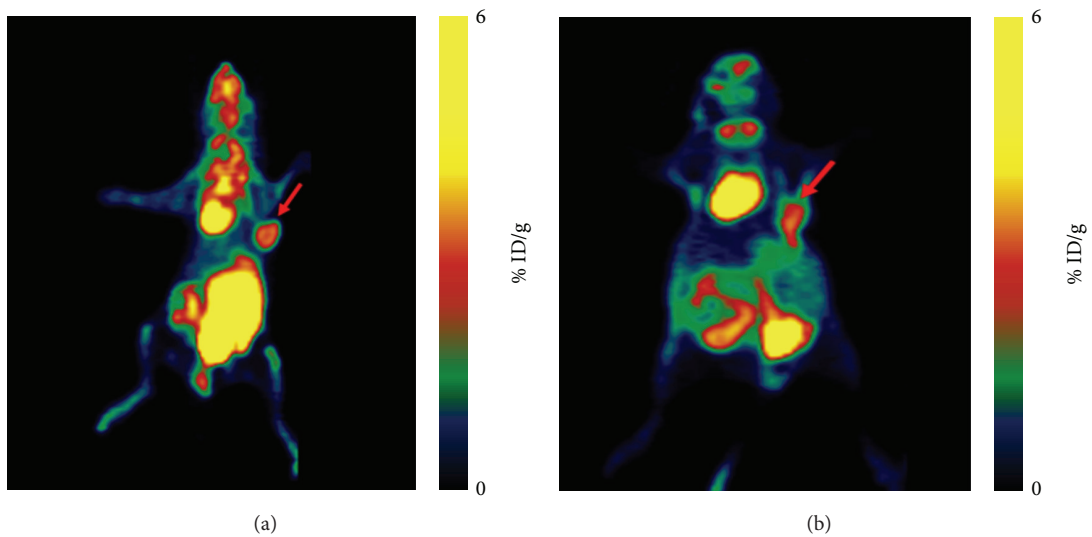


FIGURE 6: (a) Whole-body coronal microPET image of tumor-bearing MDA-MB-231 mouse at 60 min after injection of  $\sim 100 \mu\text{Ci}$   $^{18}\text{F-FDG}$ . Tumors are indicated by arrows. (b) Whole-body coronal microPET image of a tumor-bearing MCF-7 mouse at 60 min after injection of  $\sim 100 \mu\text{Ci}$   $^{18}\text{F-FDG}$ . Tumors are indicated by arrows.

MDR.  $^{68}\text{Ga}(\text{DOTA-LRB})$  may enter the tumor cells but pump out of the tumor cells as a substrate for MDR. These results suggested that the  $^{68}\text{Ga}(\text{DOTA-LRB})$  molecular probe may be used to measure the MDR of tumor.

We also found that the uptake of MDA-MB-231 and MCF-7 was positive by  $^{18}\text{F-FDG}$  microPET imaging, and the uptake of MDA-MB-231 in the high invasive  $^{18}\text{F-FDG}$  tumor was slightly higher than that in the low invasive MCF-7 tumor, but without statistical significance. Previous group has demonstrated that some types of aggressive breast cancers are associated with a high uptake for  $^{18}\text{F-FDG}$ , while more indolent breast cancers are characterized by low  $^{18}\text{F-FDG}$  uptake [28, 29].

In non-MDR negative tumors, the uptake of  $^{68}\text{Ga}(\text{DOTA-LRB})$  was low in MDA-MB-231 xenografts and MCF-7 xenografts, but it was very easy to synthesize. In the future study, we will perform a study of  $^{68}\text{Ga}(\text{DOTA-LRB})$  in MDR negative tumors.

## 5. Conclusions

$^{68}\text{Ga}(\text{DOTA-LRB})$  can be easily synthesized with high radiochemical purity and stability.  $^{68}\text{Ga}(\text{DOTA-LRB})$  may be not an ideal PET radiotracer for tumor imaging of non-MDR-negative tumors.

## Conflict of Interests

The authors declare that there is no conflict of interests regarding the publication of this paper.

## Acknowledgments

This work was supported by the National Natural Science Foundation of China (Grant no. 81301249). The authors also express appreciation to Dr. Shuang Liu for guidance and support for the synthesis of radiotracer.

## References

- [1] R. M. Perera, S. Stoykova, B. N. Nicolay et al., "Transcriptional control of autophagy-lysosome function drives pancreatic cancer metabolism," *Nature*, vol. 524, no. 7565, pp. 361–365, 2015.
- [2] S.-M. Jeon, N. S. Chandel, and N. Hay, "AMPK regulates NADPH homeostasis to promote tumour cell survival during energy stress," *Nature*, vol. 485, no. 7400, pp. 661–665, 2012.
- [3] O. Warburg, "On the origin of cancer cells," *Science*, vol. 123, no. 3191, pp. 309–314, 1956.
- [4] M. G. V. Heiden, L. C. Cantley, and C. B. Thompson, "Understanding the warburg effect: the metabolic requirements of cell proliferation," *Science*, vol. 324, no. 5930, pp. 1029–1033, 2009.
- [5] S. Pavlides, D. Whitaker-Menezes, R. Castello-Cros et al., "The reverse Warburg effect: aerobic glycolysis in cancer associated fibroblasts and the tumor stroma," *Cell Cycle*, vol. 8, no. 23, pp. 3984–4001, 2009.
- [6] G. Bonucci, D. Whitaker-Menezes, R. Castello-Cros et al., "The reverse Warburg effect: glycolysis inhibitors prevent the tumor promoting effects of caveolin-1 deficient cancer associated fibroblasts," *Cell Cycle*, vol. 9, no. 10, pp. 1960–1971, 2010.
- [7] S. Pavlides, A. Tsigirig, I. Vera et al., "Loss of stromal caveolin-1 leads to oxidative stress, mimics hypoxia and drives inflammation in the tumor microenvironment, conferring the 'reverse Warburg effect': a transcriptional informatics analysis with validation," *Cell Cycle*, vol. 9, no. 11, pp. 2201–2219, 2010.
- [8] F. Sotgia, D. Whitaker-Menezes, U. E. Martinez-Outschoorn et al., "Mitochondria 'fuel' breast cancer metabolism: fifteen markers of mitochondrial biogenesis label epithelial cancer cells, but are excluded from adjacent stromal cells," *Cell Cycle*, vol. 11, no. 23, pp. 4390–4401, 2012.
- [9] J. S. Modica-Napolitano and K. K. Singh, "Mitochondria as targets for detection and treatment of cancer," *Expert Reviews in Molecular Medicine*, vol. 4, no. 9, pp. 1–19, 2002.
- [10] M. R. Duchon, "Mitochondria in health and disease: perspectives on a new mitochondrial biology," *Molecular Aspects of Medicine*, vol. 25, no. 4, pp. 365–451, 2004.
- [11] S.-G. Huang, "Development of a high throughput screening assay for mitochondrial membrane potential in living cells," *Journal of Biomolecular Screening*, vol. 7, no. 4, pp. 383–389, 2002.
- [12] E. Gottlieb and C. B. Thompson, "Targeting the mitochondria to enhance tumor suppression," *Methods in Molecular Biology*, vol. 223, pp. 543–554, 2003.
- [13] M. F. Ross, G. F. Kelso, F. H. Blaikie et al., "Lipophilic triphenylphosphonium cations as tools in mitochondrial bioenergetics and free radical biology," *Biochemistry*, vol. 70, no. 2, pp. 222–230, 2005.
- [14] C. T. Yang, Y. S. Kim, J. Wang et al., " $^{64}\text{Cu}$ -labeled 2-(diphenylphosphoryl) ethyldiphenylphosphonium cations as highly selective tumor imaging agents: effects of linkers and chelates on radiotracer biodistribution characteristics," *Bioconjugate Chemistry*, vol. 19, no. 10, pp. 2008–2022, 2008.
- [15] J. J. Min, S. Biswal, C. Deroose, and S. S. Gambhir, "Tetraphenylphosphonium as a novel molecular probe for imaging tumors," *Journal of Nuclear Medicine*, vol. 45, no. 4, pp. 636–643, 2004.
- [16] Y. Zhou, Y.-S. Kim, X. Yan, O. Jacobson, X. Chen, and S. Liu, " $^{64}\text{Cu}$ -labeled Lissamine rhodamine B: a promising PET radiotracer targeting tumor mitochondria," *Molecular Pharmaceutics*, vol. 8, no. 4, pp. 1198–1208, 2011.
- [17] D. Pan, Y. P. Xu, R. H. Yang et al., "A new  $^{68}\text{Ga}$ -labeled BBN peptide with a hydrophilic linker for GRPR-targeted tumor imaging," *Amino Acids*, vol. 46, no. 6, pp. 1481–1489, 2014.
- [18] J. S. Modica-Napolitano and J. R. Aprille, "Delocalized lipophilic cations selectively target the mitochondria of carcinoma cells," *Advanced Drug Delivery Reviews*, vol. 49, no. 1–2, pp. 63–70, 2001.
- [19] G. Kroemer, B. Dallaporta, and M. Resche-Rigon, "The mitochondrial death/life regulator in apoptosis and necrosis," *Annual Review of Physiology*, vol. 60, pp. 619–642, 1998.
- [20] S. H. Dairkee and A. J. Hackett, "Differential retention of rhodamine 123 by breast carcinoma and normal human mammary tissue," *Breast Cancer Research and Treatment*, vol. 18, no. 1, pp. 57–61, 1991.
- [21] K. P. Zhernosekov, D. V. Filosofov, R. P. Baum et al., "Processing of generator-produced  $^{68}\text{Ga}$  for medical application," *Journal of Nuclear Medicine*, vol. 48, no. 10, pp. 1741–1748, 2007.
- [22] W. A. P. Breeman, E. de Blois, H. Sze Chan, M. Konijnenberg, D. J. Kwekkeboom, and E. P. Krenning, " $^{68}\text{Ga}$ -labeled DOTA-peptides and  $^{68}\text{Ga}$ -labeled radiopharmaceuticals for positron

- emission tomography: current status of research, clinical applications, and future perspectives,” *Seminars in Nuclear Medicine*, vol. 41, no. 4, pp. 314–321, 2011.
- [23] I. Virgolini, V. Ambrosini, J. B. Bomanji et al., “Procedure guidelines for PET/CT tumour imaging with  $^{68}\text{Ga}$ -DOTA-conjugated peptides:  $^{68}\text{Ga}$ -DOTA-TOC,  $^{68}\text{Ga}$ -DOTA-NOC,  $^{68}\text{Ga}$ -DOTA-TATE,” *European Journal of Nuclear Medicine and Molecular Imaging*, vol. 37, no. 10, pp. 2004–2010, 2010.
- [24] Y. Zhou, Y.-S. Kim, J. Shi, O. Jacobson, X. Chen, and S. Liu, “Evaluation of  $^{64}\text{Cu}$ -labeled acridinium cation: a PET radiotracer targeting tumor mitochondria,” *Bioconjugate Chemistry*, vol. 22, no. 4, pp. 700–708, 2011.
- [25] Y.-J. Chen, C.-D. Kuo, S.-H. Chen et al., “Small-molecule synthetic compound norcantharidin reverses multi-drug resistance by regulating Sonic hedgehog signaling in human breast cancer cells,” *PLoS ONE*, vol. 7, no. 5, Article ID e37006, 2012.
- [26] D. Piwnicka-Worms and V. Sharma, “Probing multidrug resistance P-glycoprotein transporter activity with SPECT radiopharmaceuticals,” *Current Topics in Medicinal Chemistry*, vol. 10, no. 17, pp. 1834–1845, 2010.
- [27] G. Trencsényi, I. Kertész, Z. T. Krasznai et al., “2'[(18)F]-fluoroethylrhodamine B is a promising radiotracer to measure P-glycoprotein function,” *European Journal of Pharmaceutical Sciences*, vol. 74, no. 8, pp. 27–35, 2015.
- [28] K. McLarty, M. D. Moran, D. A. Scollard et al., “Comparisons of [ $^{18}\text{F}$ ]-1-deoxy-1-fluoro-scylo-inositol with [ $^{18}\text{F}$ ]-FDG for PET imaging of inflammation, breast and brain cancer xenografts in athymic mice,” *Nuclear Medicine and Biology*, vol. 38, no. 7, pp. 953–959, 2011.
- [29] M. W. Makinen, R. Bamba, L. Ikejimba, C. Wietholt, C.-T. Chen, and S. D. Conzen, “The vanadyl chelate bis(acetylacetonato)oxovanadium(IV) increases the fractional uptake of 2-(fluorine-18)-2-deoxy-D-glucose by cultured human breast carcinoma cells,” *Dalton Transactions*, vol. 42, no. 33, pp. 11862–11867, 2013.

## Research Article

# **$N$ - $^{11}\text{C}$ -Methyl-Dopamine PET Imaging of Sympathetic Nerve Injury in a Swine Model of Acute Myocardial Ischemia: A Comparison with $^{13}\text{N}$ -Ammonia PET**

Weina Zhou,<sup>1</sup> Xiangcheng Wang,<sup>1</sup> Yulin He,<sup>1</sup> Yongzhen Nie,<sup>2</sup> Guojian Zhang,<sup>1</sup> Cheng Wang,<sup>1</sup> Chunmei Wang,<sup>1</sup> and Xuemei Wang<sup>1</sup>

<sup>1</sup>Department of Nuclear Medicine, Affiliated Hospital of Inner Mongolia Medical University, Hohhot, Inner Mongolia 010050, China

<sup>2</sup>Department of Anesthesiology, Affiliated People's Hospital of Inner Mongolia Medical University, Hohhot, Inner Mongolia 010020, China

Correspondence should be addressed to Xuemei Wang; wangxuemei201010@163.com

Received 24 November 2015; Accepted 6 January 2016

Academic Editor: James Russell

Copyright © 2016 Weina Zhou et al. This is an open access article distributed under the Creative Commons Attribution License, which permits unrestricted use, distribution, and reproduction in any medium, provided the original work is properly cited.

**Objective.** Using a swine model of acute myocardial ischemia, we sought to validate  $N$ - $^{11}\text{C}$ -methyl-dopamine ( $^{11}\text{C}$ -MDA) as an agent capable of imaging cardiac sympathetic nerve injury. **Methods.** Acute myocardial ischemia was surgically generated in Chinese minipigs. ECG and serum enzyme levels were used to detect the presence of myocardial ischemia. Paired  $^{11}\text{C}$ -MDA PET and  $^{13}\text{N}$ -ammonia PET scans were performed at baseline, 1 day, and 1, 3, and 6 months after surgery to relate cardiac sympathetic nerve injury to blood perfusion. **Results.** Seven survived the surgical procedure. The ECG-ST segment was depressed, and levels of the serum enzymes increased. Cardiac uptake of tracer was quantified as the defect volume. Both before and immediately after surgery, the images obtained with  $^{11}\text{C}$ -MDA and  $^{13}\text{N}$ -ammonia were similar. At 1 to 6 months after surgery, however,  $^{11}\text{C}$ -MDA postsurgical left ventricular myocardial defect volume was significantly greater compared to  $^{13}\text{N}$ -ammonia. **Conclusions.** In the Chinese minipig model of acute myocardial ischemia, the extent of the myocardial defect as visualized by  $^{11}\text{C}$ -MDA is much greater than would be suggested by blood perfusion images, and the recovery from myocardial sympathetic nerve injury is much slower than the restoration of blood perfusion.  $^{11}\text{C}$ -MDA PET may provide additional biological information during recovery from ischemic heart disease.

## 1. Introduction

Cardiovascular disease is the leading cause of death worldwide [1], and myocardial ischemia and myocardial infarction are the major causes of fatal heart failure. Early diagnosis of myocardial ischemia and myocardial infarction is required to reduce mortality, particularly through evaluation of electrophysiological changes after cardiac injury. Studies have shown that myocardial ischemia is followed by reduced perfusion and abnormalities of innervation, metabolism, and wall motion, as well as endothelial dysfunction [2–7]. The cardiac sympathetic nerves play a key role in regulating heart function [8]. It has been demonstrated in severe coronary artery stenosis that sympathetic tissues are more susceptible to ischemia than myocardial muscle cells [9, 10]. Accordingly, we hypothesized that cardiac sympathetic nerve injury may

be a more sensitive marker of postischemic cardiac damage than changes in blood perfusion during early stage coronary artery events. Many studies have explored myocardial reperfusion and metabolism. However, sympathetic nerve injury and reinnervation, particularly in regard to early diagnosis, have been less examined.

Several compounds have been used for sympathetic nerve receptor imaging in preclinical or clinical studies [11–16]. Both  $^{123}\text{I}$  metaiodobenzylguanidine ( $^{123}\text{I}$ -MIBG) and  $^{11}\text{C}$ -hydroxyephedrine ( $^{11}\text{C}$ -HED) are norepinephrine analogs [17, 18], which are accumulated via the norepinephrine transporter (NET) [19]. However, neither tracer has been found to be suitable for the early detection of sympathetic denervation [20].  $6$ - $^{18}\text{F}$ -Fluorodopamine ( $^{18}\text{F}$ -DA) is an imaging agent used for the evaluation of primary or secondary lesions in

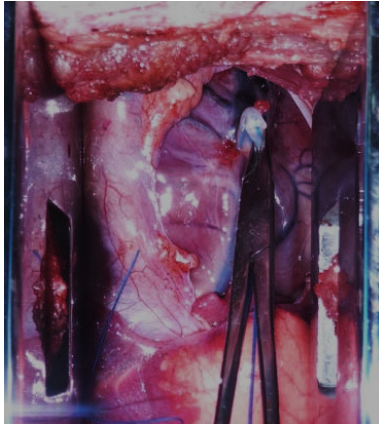


FIGURE 1: A thoracotomy with blocking of the left anterior descending coronary artery, to generate acute myocardial ischemia in a Chinese minipig.

sympathetic tissue [21, 22]. However, the synthesis of  $^{18}\text{F}$ -MDA is expensive and produces low yields, and these problems have limited its use.

We have recently synthesized a novel tracer  $N$ - $^{11}\text{C}$ -methyl-dopamine ( $^{11}\text{C}$ -MDA) for cardiac sympathetic nerve imaging. The biological properties of  $^{11}\text{C}$ -MDA were evaluated in normal mice and healthy Chinese minipigs [23].  $^{11}\text{C}$ -MDA had a high myocardium uptake in biodistribution studies. It could be clearly imaged in the heart by PET/CT, and this uptake was blocked by imipramine hydrochloride. Therefore,  $^{11}\text{C}$ -MDA is a promising candidate radiotracer for imaging the cardiac sympathetic nervous system.

In this study, we established a model of acute myocardial ischemia in Chinese minipigs. Animals were imaged by PET/CT with  $^{11}\text{C}$ -MDA and  $^{13}\text{N}$ -ammonia for myocardial blood perfusion. In this way, we were able to observe cardiac sympathetic nerve injury and recovery over a period of 6 months.

## 2. Materials and Methods

**2.1. Synthesis of  $^{11}\text{C}$ -MDA and  $^{13}\text{N}$ -Ammonia.**  $^{11}\text{C}$ -MDA and  $^{13}\text{N}$ -ammonia were synthesized in-house in our PET center cyclotron facility as previously described [23]. Radiochemical purity was greater than 95% for both  $^{11}\text{C}$ -MDA and  $^{13}\text{N}$ -ammonia. Radiopharmaceuticals were passed through a  $0.2\ \mu\text{m}$  membrane filter for in vivo use.

**2.2. Animal Model of Cardiac Disease.** The study reported here, as well as all aspects of animal maintenance and welfare, was approved by the Inner Mongolian Medical University Animal Care and Use Committee. Ten Chinese minipigs (Shihuang Shiji Mini-Pig Breeding Base, Beijing, China) were maintained in our large animal facility, housed singly, and supplied with the standard diet for swine.

Surgery was performed as follows: Animals were fasted for 6 hours and intramuscularly injected with ketamine (20 mg/kg) and diazepam (2 mg/kg) for anesthesia; an intravenous route was established at the ear vein and propofol

(2 mg/kg/h) was infused to maintain anesthesia. Pigs were placed on the operating table and connected to ECG and oxygen monitor. After successful intubation, the animal underwent ventilator-assisted breathing (tidal volume 8–10 mL/kg, respiratory rate 12–15 beats/min, and respiratory ratio of 1:1.5). Hair on the chest was shaved, and the skin was disinfected with 0.1% benzalkonium bromide solution. As shown in Figure 1, a direct thoracotomy was performed at the fifth intercostal space. A 3 mm diameter pneumatic coronary occluder was placed around the left anterior descending coronary artery below the second diagonal branch.

The onset of ischemia was identified by an increase or decrease in the ECG-ST segment of 0.2 mV. Coronary artery occlusion was then released to form acute myocardial ischemia model. Intraoperative electrocardiographic monitoring and venous blood serum enzyme examination (aspartate amino transferase, lactate dehydrogenase, creatine kinase, myocardial muscle creatine kinase, and hydroxybutyrate dehydrogenase) at 9–12 hours after surgery were conducted in all subjects.

**2.3. PET/CT Image Acquisition.** Chinese minipigs were fixed supinely in a special wooden frame and anesthetized as described above. Animals were injected with  $^{11}\text{C}$ -MDA (74 MBq) and, 10 minutes later, given a 20-minute thoracic PET scan followed by CT. Six hours later, animals received intravenous  $^{13}\text{N}$ -ammonia (555 MBq) and, after 5 minutes, a 20-minute thoracic PET scan. A clinical PET/CT scanner (DST16-PET/CT, GE Healthcare) was used for 2D nongated PET acquisition, and low dose CT was always performed for attenuation correction (tube voltage 120 kV, tube current 80 mA, rotation time 0.5 s, 1.2 pitch, and thickness 3.75 mm) before each PET scan.

**2.4. PET/CT Image Reconstruction and Image Analysis.** After acquisition, images were transferred to Xeleris (version 4.1, GE Healthcare, USA) and AW (version 4.4, GE Healthcare, USA) image processing workstation for image interpretation and semiquantitative analysis. All image reconstruction was conducted by Butterworth filter function, and the short axis, horizontal long axis, and vertical long axis of the three cross-sectional images were presented.

**2.5. Statistical Analysis.** Data are presented as the mean  $\pm$  SD. A paired  $t$ -test was used to compare the effect of treatment on the same imaging agent and an unpaired  $t$ -test was used to compare the results of two imaging agents. ANOVA was used to analyze the cardiac defect volumes of both imaging agents. SPSS13.0 software (IBM) was used for statistical analysis. A  $P$  value less than 0.05 was considered statistically significant.

## 3. Results

**3.1. ECG and Myocardial Enzymes Changes Demonstrate the Induction of Acute Myocardial Ischemia in the Animal Model.** Of the ten pigs that underwent surgery, 7 survived and were available for 6 months of follow-up. Evidence of acute myocardial ischemia was present in all 7 animals. The ECG-ST segment was depressed by over 0.2 mV at lead II (Figure 2).

TABLE 1: Serum levels of myocardial enzymes before and after surgery.

	AST (U/L)		LDH (U/L)		CK (U/L)		CK-MB (U/L)		HBDH (U/L)	
	Before	After	Before	After	Before	After	Before	After	Before	After
1	20.0	410.9	120.0	1992.0	180.0	23720.0	15.0	664.2	84.5	1617.0
2	18.0	123.1	135.0	978.0	154.8	18083.0	13.4	481.6	79.4	874.0
3	8.0	331.2	158.0	3227.0	198.0	4014.0	7.0	372.7	80.0	1548.0
4	21.0	195.6	181.0	2559.0	148.2	7418.0	14.0	164.7	154.0	822.0
5	30.0	164.6	153.0	1579.0	75.0	8185.0	6.9	265.2	135.4	1657.0
6	25.3	215.7	127.5	1375.0	176.0	5224.0	10.7	273.5	92.7	1385.0
7	27.8	305.5	159.3	1498.0	210.0	6718.0	13.2	318.7	127.4	1439.0
Mean	21.4	249.5	147.7	1886.9	163.1	10480.3	11.5	362.9	107.6	1334.6
SD	7.3	102.5	21.3	773.8	44.6	7431.2	3.3	165.2	30.6	345.8

AST: normal reference value (8–37 U/L); LDH: normal reference value (110–240 U/L); CK: normal reference value (0–250 U/L); CK-MB: normal reference value (0–25 U/L); HBDH: normal reference value (72–182 U/L).

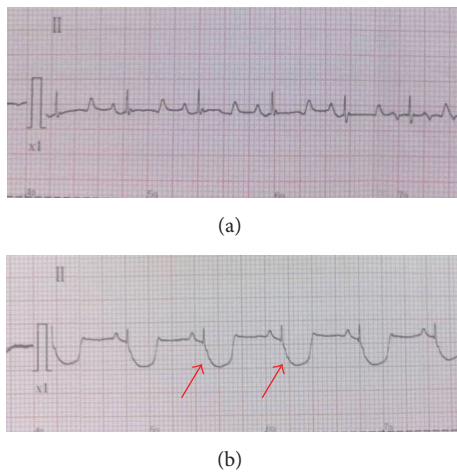


FIGURE 2: ECG records. (a) Before surgery. (b) After surgery. ST-T segments, showing characteristic depression, are indicated by arrows.

Blood serum enzymes (listed in Table 1) were examined 9–12 hours after surgery, and, for all enzymes examined, all animals showed a marked increase over baseline.

3.2.  $^{11}\text{C}$ -MDA and  $^{13}\text{N}$ -Ammonia Imaging of Damage to Cardiac Tissue. Baseline  $^{11}\text{C}$ -MDA PET showed uniform distribution of radioactivity in the left ventricular myocardium and mild uptake in the right ventricular wall, which was broadly similar to  $^{13}\text{N}$ -ammonia myocardium images (Figure 3). Serial  $^{11}\text{C}$ -MDA and subsequent  $^{13}\text{N}$ -ammonia scans were performed 1 day and 1, 3, and 6 months after surgery. One day after the surgery, there was obvious uptake defect in  $^{11}\text{C}$ -MDA imaging but not  $^{13}\text{N}$ -ammonia; the myocardial uptake defect was the widest in 3 months for both  $^{11}\text{C}$ -MDA and  $^{13}\text{N}$ -ammonia. A total restoration of  $^{13}\text{N}$ -ammonia uptake was observed at 6 months, but recovery for  $^{11}\text{C}$ -MDA uptake was still on its way. The  $^{11}\text{C}$ -MDA PET images revealed a defect area that was wider than that suggested by  $^{13}\text{N}$ -ammonia PET. This was true at all time points examined,

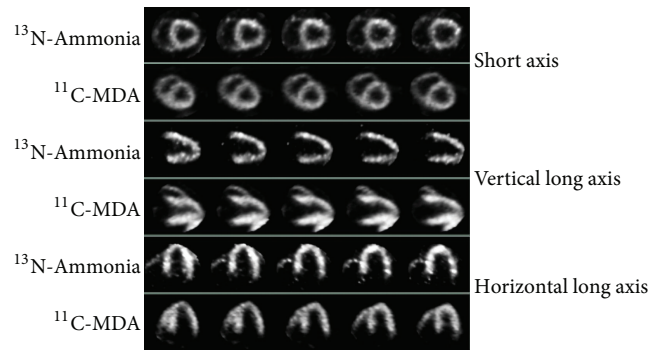


FIGURE 3: Baseline  $^{11}\text{C}$ -MDA and  $^{13}\text{N}$ -ammonia PET in a preoperation pig.  $^{11}\text{C}$ -MDA and  $^{13}\text{N}$ -ammonia PET scans were performed over a 6-hour interval. Short axis and vertical and horizontal long axis imaging of the myocardium are presented.

as  $^{11}\text{C}$ -MDA imaging revealed that the defect area recovered slowly (Figures 4 and 5, Table 2), a finding confirmed by the bull's-eye diagram (Figure 6).

#### 4. Discussion

In this study, we established acute cardiac ischemia model in Chinese minipig (Figures 1 and 2); we have found that  $^{11}\text{C}$ -MDA imaging was more sensitive than  $^{13}\text{N}$ -ammonia for detection myocardium damage following acute ischemic event (Figures 3–6). Unfortunately, we were unable to directly compare  $^{11}\text{C}$ -MDA and  $^{123}\text{I}$ -MIBG in this study, owing to the absence of  $^{123}\text{I}$  in China, and cardiac imaging with  $^{131}\text{I}$ -MIBG proved ineffective. However, our findings with  $^{11}\text{C}$ -MDA are consistent with other tracers in clinical use. For example, in a study of 31 patients with coronary heart disease, Hartikainen et al. found that the defect area revealed by  $^{123}\text{I}$ -MIBG and  $^{99\text{m}}\text{Tc}$ -sestamibi ( $^{99\text{m}}\text{Tc}$ -MIBI) imaging was greater than that suggested by myocardial blood perfusion imaging [24]. In 8 patients with multivessel coronary heart disease but without myocardial infarction, Bülow et al. found significantly reduced  $^{11}\text{C}$ -HED retention, while

TABLE 2: Comparison of defect scores, ischemic-to-normal ratios, and volume of ischemic myocardium for  $^{11}\text{C-N-CH}_3$ -dopamine and  $^{13}\text{N-ammonia}$  PET imaging at each time point after myocardial ischemia-reperfusion.

Time	Defect score		Ischemic-to-normal ratio		Volume of ischemic myocardium ( $\text{cm}^3$ )		P
	$^{11}\text{C-N-CH}_3$ -dopamine	$^{13}\text{N-Ammonia}$	$^{11}\text{C-N-CH}_3$ -dopamine	$^{13}\text{N-Ammonia}$	$^{11}\text{C-N-CH}_3$ -dopamine	$^{13}\text{N-Ammonia}$	
1 day	$10.2 \pm 2.5$	$9.9 \pm 0.9$	$0.61 \pm 0.12$	$0.61 \pm 0.08$	$3.79 \pm 0.06$	$3.66 \pm 0.08$	NS
1 month	$13.3 \pm 3.3$	$7.7 \pm 1.0$	$0.51 \pm 0.22$	$0.60 \pm 0.10$	$4.21 \pm 0.34$	$2.54 \pm 0.11$	<0.001
3 months	$18.6 \pm 4.4$	$4.9 \pm 1.0$	$0.42 \pm 0.13$	$0.60 \pm 0.09$	$10.67 \pm 0.71$	$2.47 \pm 0.12$	<0.001
6 months	$10.7 \pm 4.2$	$4.1 \pm 0.9$	$0.60 \pm 0.17$	$0.60 \pm 0.09$	$5.96 \pm 0.50$	$2.43 \pm 0.11$	<0.001

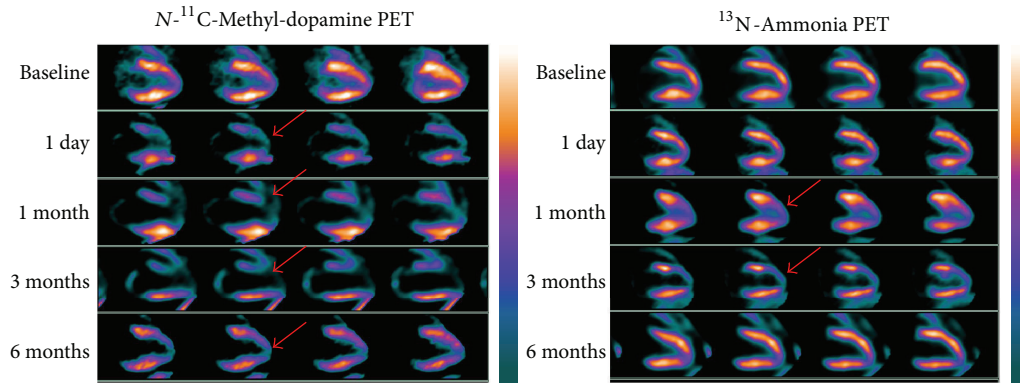


FIGURE 4: Serial  $^{11}\text{C}$ -MDA and  $^{13}\text{N}$ -ammonia PET imaging, shown in the vertical long axis of an injured pig at 1 day, 1 month, 3 months, and 6 months after surgery. The defective region is broader in  $^{11}\text{C}$ -MDA images compared to  $^{13}\text{N}$ -ammonia (arrows).

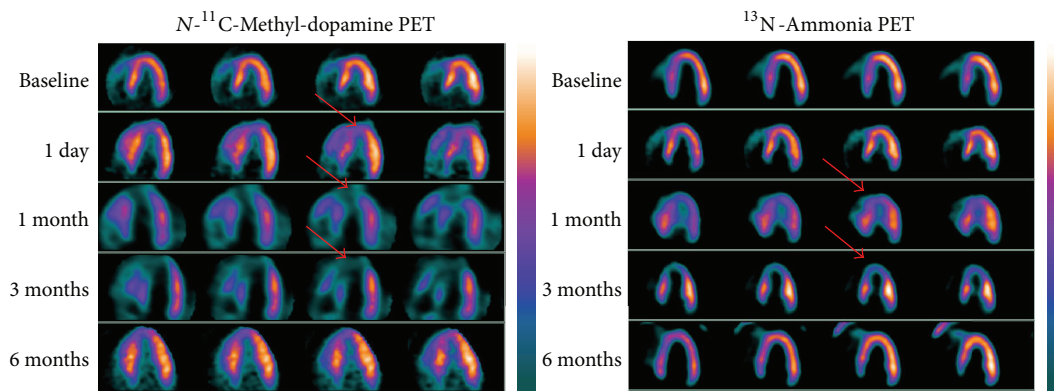


FIGURE 5: Serial  $^{11}\text{C}$ -MDA and  $^{13}\text{N}$ -ammonia PET imaging, shown in the horizontal long axis of an injured pig at 1 day, 1 month, 3 months, and 6 months after surgery. The defective region is broader in  $^{11}\text{C}$ -MDA images compared to  $^{13}\text{N}$ -ammonia (arrows).

$^{13}\text{N}$ -ammonia was unperturbed [25]. Accordingly,  $^{11}\text{C}$ -MDA provides more information than blood perfusion imaging for evaluation of post-acute ischemia induced myocardium injury and recovery.

Damage to nervous tissue is an inevitable consequence of myocardial ischemia or infarction, and activation of sympathetic reflex leads to increased vasospasm. As the nutrient supply is restricted and metabolic waste products cannot be efficiently cleared, further nerve damage ensues. Moreover, ATP pools in nerve terminals become depleted, also triggering damage to the nerve endings, and this damage is generally beyond repair. Reperfusion and calcium release from endothelial cells also contribute to damage.

The study also found that myocardial ischemia-reperfusion and cardiac sympathetic restoration occurred over different time scales (Figures 4–6). This finding was consistent with many other studies [26, 27], which showed that animals that had acute myocardial infarction would have varying degrees of cardiac sympathetic nerve regeneration. In 10 patients followed by  $^{18}\text{F}$ -DA imaging, Fallen et al. [28] found that tracer uptake increased by 14%–15% between 2 weeks and 3 months after myocardial infarction, with no further changes being noted over the next 3 months. Our

results are thus in line with previously published data, bearing in mind the different experimental model and the difference between myocardial ischemia and myocardial infarction. The mismatch between the restoration of myocardial perfusion and normal myocardial sympathetic response could cause life-threatening ventricular arrhythmias [29], and at the same time immune reactions were more likely to occur to harmful ventricular arrhythmias [30, 31]. Sympathetic nerve regeneration plays a critical role in ventricular arrhythmias [32], and in general cardiac pathology [33], including sudden cardiac death, congestive heart failure, and diabetic autonomic neuropathy [34, 35]. Our study found that the use of  $^{11}\text{C}$ -MDA PET/CT imaging could successfully detect abnormal sympathetic tissue in the damaged heart (Figures 4 and 5), and this agent may have an important role in cardiac imaging.

The objective of this study was to compare  $^{11}\text{C}$ -MDA PET imaging sympathetic nerve recovery with  $^{13}\text{N}$ -ammonia for blood perfusion; dynamic PET acquisition immediately after tracer inoculation was not conducted in this study. Dynamic PET data analysis for compartment modeling was not performed in this study, and a future study may need to focus on this issue.

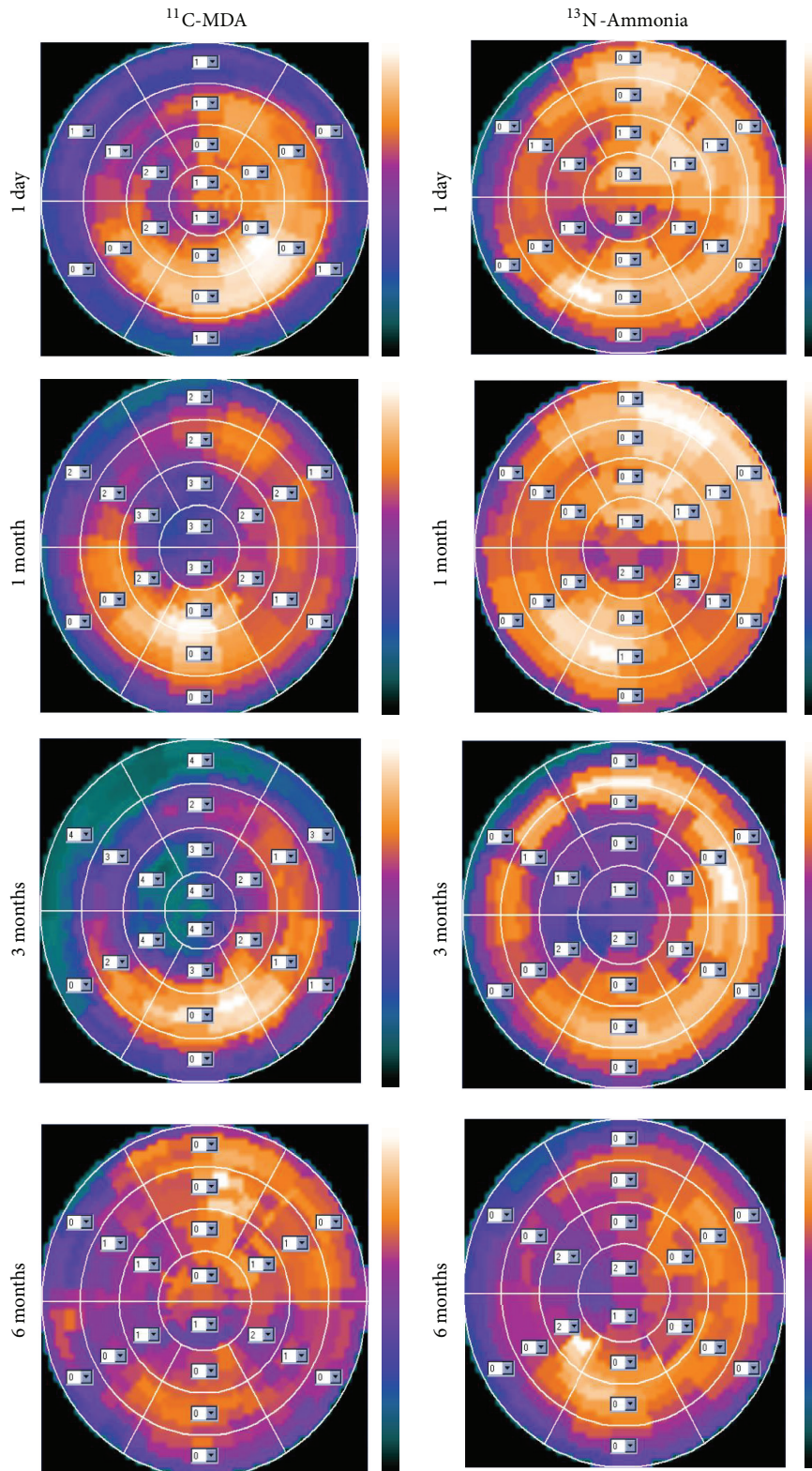


FIGURE 6: Bull's-eye diagram of  $^{11}\text{C-MDA}$  and  $^{13}\text{N-ammonia}$  PET during the 6 months following treatment.

## 5. Conclusion

Using a Chinese minipig model of acute myocardial ischemia, we have demonstrated that  $^{11}\text{C}$ -MDA is capable of imaging cardiac damage and provides information that is distinct from blood perfusion imaging.  $^{11}\text{C}$ -MDA PET may provide additional biological information during recovery from ischemic heart disease.

## Conflict of Interests

The authors declare that there is no conflict of interests regarding the publication of this paper.

## Authors' Contribution

Weina Zhou and Xiangcheng Wang contributed equally to this work.

## Acknowledgments

This study was supported by Natural Science foundation of China (nos. 81060019, 81560686, and 81460271) and Natural Science foundation of Inner Mongolia (nos. 2012ZD11, 2014MS0859, and 2013MS1188) and Inner Mongolia Medical University Affiliated Hospital Scientific Research Project 2014NYFYB008. The authors thank Dr. Wei Fang from Cardiovascular Institute and Fuwai Hospital of China, for comments during preparation of this paper.

## References

- [1] R. O. Bonow, L. A. Smaha, S. C. Smith Jr., G. A. Mensah, and C. Lenfant, "World Heart Day 2002: the international burden of cardiovascular disease: responding to the emerging global epidemic," *Circulation*, vol. 106, no. 13, pp. 1602–1605, 2002.
- [2] M. S. Stanton, M. M. Tuli, N. L. Radtke et al., "Regional sympathetic denervation after myocardial infarction in humans detected noninvasively using I-123-metaiodobenzylguanidine," *Journal of the American College of Cardiology*, vol. 14, no. 6, pp. 1519–1526, 1989.
- [3] A. I. McGhie, J. R. Corbett, M. S. Akers et al., "Regional cardiac adrenergic function using I-123 meta-iodobenzylguanidine tomographic imaging after acute myocardial infarction," *The American Journal of Cardiology*, vol. 67, no. 4, pp. 236–242, 1991.
- [4] M. W. Dae, J. M. Herre, J. W. O'Connell, E. H. Botvinick, D. Newman, and L. Munoz, "Scintigraphic assessment of sympathetic innervation after transmural versus nontransmural myocardial infarction," *Journal of the American College of Cardiology*, vol. 17, no. 6, pp. 1416–1423, 1991.
- [5] S. Simula, T. Lakka, T. Laitinen et al., "Cardiac adrenergic denervation in patients with non-Q-wave versus Q-wave myocardial infarction," *European Journal of Nuclear Medicine*, vol. 27, no. 7, pp. 816–821, 2000.
- [6] Y. Kawai, E. Tsukamoto, Y. Nozaki, K. Morita, M. Sakurai, and N. Tamaki, "Significance of reduced uptake of iodinated fatty acid analogue for the evaluation of patients with acute chest pain," *Journal of the American College of Cardiology*, vol. 38, no. 7, pp. 1888–1894, 2001.
- [7] K. Watanabe, T. Takahashi, S. Miyajima et al., "Myocardial sympathetic denervation, fatty acid metabolism, and left ventricular wall motion in vasospastic angina," *Journal of Nuclear Medicine*, vol. 43, no. 11, pp. 1476–1481, 2002.
- [8] D. M. Raffel and D. M. Wieland, "Assessment of cardiac sympathetic nerve integrity with positron emission tomography," *Nuclear Medicine and Biology*, vol. 28, no. 5, pp. 541–559, 2001.
- [9] S. Joho, H. Asanoi, J. Takagawa et al., "Cardiac sympathetic denervation modulates the sympathoexcitatory response to acute myocardial ischemia," *Journal of the American College of Cardiology*, vol. 39, no. 3, pp. 436–442, 2002.
- [10] F. M. Bengel and M. Schwaiger, "Assessment of cardiac sympathetic neuronal function using PET imaging," *Journal of Nuclear Cardiology*, vol. 11, no. 5, pp. 603–616, 2004.
- [11] K. Sakata, M. Shirovani, H. Yoshida, and C. Kurata, "Iodine-123 metaiodobenzylguanidine cardiac imaging to identify and localize vasospastic angina without significant coronary artery narrowing," *Journal of the American College of Cardiology*, vol. 30, no. 2, pp. 370–376, 1997.
- [12] Y. Inobe, K. Kugiyama, H. Miyagi et al., "Long-lasting abnormalities in cardiac sympathetic nervous system in patients with coronary spastic angina: quantitative analysis with iodine 123 metaiodobenzylguanidine myocardial scintigraphy," *American Heart Journal*, vol. 134, no. 1, pp. 112–118, 1997.
- [13] A. Cohen-Solal, F. Rouzet, A. Berdeaux et al., "Effects of carvedilol on myocardial sympathetic innervation in patients with chronic heart failure," *Journal of Nuclear Medicine*, vol. 46, no. 11, pp. 1796–1803, 2005.
- [14] S. Yamashina and J.-I. Yamazaki, "Neuronal imaging using SPECT," *European Journal of Nuclear Medicine and Molecular Imaging*, vol. 34, supplement 1, pp. S62–S73, 2007.
- [15] R. Lautamäki, D. Tipre, and F. M. Bengel, "Cardiac sympathetic neuronal imaging using PET," *European Journal of Nuclear Medicine and Molecular Imaging*, vol. 34, supplement 1, pp. S74–S85, 2007.
- [16] F. M. Bengel, "Imaging targets of the sympathetic nervous system of the heart: translational considerations," *Journal of Nuclear Medicine*, vol. 52, no. 8, pp. 1167–1170, 2011.
- [17] D. M. Wieland, L. E. Brown, W. L. Rogers et al., "Myocardial imaging with a radioiodinated norepinephrine storage analog," *Journal of Nuclear Medicine*, vol. 22, no. 1, pp. 22–31, 1981.
- [18] M. Schwaiger, V. Kalff, K. Rosenspire et al., "Noninvasive evaluation of sympathetic nervous system in human heart by positron emission tomography," *Circulation*, vol. 82, no. 2, pp. 457–464, 1990.
- [19] D. M. Raffel and D. M. Wieland, "Assessment of cardiac sympathetic nerve integrity with positron emission tomography," *Nuclear Medicine and Biology*, vol. 28, no. 5, pp. 541–559, 2001.
- [20] K. S. Jang, Y.-W. Jung, P. S. Sherman, C. A. Quesada, G. Gu, and D. M. Raffel, "Synthesis and bioevaluation of [ $^{18}\text{F}$ ]4-fluoro-*m*-hydroxyphenethylguanidine ([ $^{18}\text{F}$ ]4F-MHPG): a novel radiotracer for quantitative PET studies of cardiac sympathetic innervation," *Bioorganic & Medicinal Chemistry Letters*, vol. 23, no. 6, pp. 1612–1616, 2013.
- [21] I. Ilias, C. C. Chen, J. A. Carrasquillo et al., "Comparison of 6- $^{18}\text{F}$ -fluorodopamine PET with 123I- metaiodobenzylguanidine and 111In-pentetreotide scintigraphy in localization of nonmetastatic and metastatic pheochromocytoma," *Journal of Nuclear Medicine*, vol. 49, no. 10, pp. 1613–1619, 2008.
- [22] H. J. L. M. Timmers, C. C. Chen, J. A. Carrasquillo et al., "Comparison of  $^{18}\text{F}$ -fluoro-L-DOPA,  $^{18}\text{F}$ -fluoro-deoxyglucose,

- and  $^{18}\text{F}$ -fluorodopamine PET and  $^{123}\text{I}$ -MIBG scintigraphy in the localization of pheochromocytoma and paraganglioma," *Journal of Clinical Endocrinology and Metabolism*, vol. 94, no. 12, pp. 4757–4767, 2009.
- [23] Y. L. He, W. N. Zhou, X. C. Wang et al., "The synthesis of a new cardiac sympathetic nerve imaging agent  $N$ - $^{11}\text{C}$ CH<sub>3</sub>-dopamine and biodistribution study," *Journal of Radioanalytical and Nuclear Chemistry*, vol. 301, no. 2, pp. 469–474, 2014.
- [24] J. Hartikainen, J. Mustonen, J. Kuikka, E. Vanninen, and R. Kettunen, "Cardiac sympathetic denervation in patients with coronary artery disease without previous myocardial infarction," *American Journal of Cardiology*, vol. 80, no. 3, pp. 273–277, 1997.
- [25] H. P. Bülow, F. Stahl, B. Lauer et al., "Alterations of myocardial presynaptic sympathetic innervation in patients with multi-vessel coronary artery disease but without history of myocardial infarction," *Nuclear Medicine Communications*, vol. 24, no. 3, pp. 233–239, 2003.
- [26] I. Matsunari, U. Schricke, F. M. Bengel et al., "Extent of cardiac sympathetic neuronal damage is determined by the area of ischemia in patients with acute coronary syndromes," *Circulation*, vol. 101, no. 22, pp. 2579–2585, 2000.
- [27] M. V. Simões, P. Barthel, I. Matsunari et al., "Presence of sympathetically denervated but viable myocardium and its electrophysiologic correlates after early revascularised, acute myocardial infarction," *European Heart Journal*, vol. 25, no. 7, pp. 551–557, 2004.
- [28] E. L. Fallen, G. Coates, C. Nahmias et al., "Recovery rates of regional sympathetic reinnervation and myocardial blood flow after acute myocardial infarction," *American Heart Journal*, vol. 137, no. 5, pp. 863–869, 1999.
- [29] H. V. Huikuri, M. J. P. Raatikainen, R. Moerch-Joergensen et al., "Prediction of fatal or near-fatal cardiac arrhythmia events in patients with depressed left ventricular function after an acute myocardial infarction," *European Heart Journal*, vol. 30, no. 6, pp. 689–698, 2009.
- [30] D. S. Goldstein, B. Eldadah, Y. Sharabi, and F. B. Axelrod, "Cardiac sympathetic hypo-innervation in familial dysautonomia," *Clinical Autonomic Research*, vol. 18, no. 3, pp. 115–119, 2008.
- [31] T. Sasano, M. R. Abraham, K.-C. Chang et al., "Abnormal sympathetic innervation of viable myocardium and the substrate of ventricular tachycardia after myocardial infarction," *Journal of the American College of Cardiology*, vol. 51, no. 23, pp. 2266–2275, 2008.
- [32] D. P. Zipes and M. Rubart, "Neural modulation of cardiac arrhythmias and sudden cardiac death," *Heart Rhythm*, vol. 3, no. 1, pp. 108–113, 2006.
- [33] P. J. Schwartz, "The autonomic nervous system and sudden death," *European Heart Journal*, vol. 19, supplement F, pp. F72–F80, 1998.
- [34] M. Packer, "The neurohormonal hypothesis: a theory to explain the mechanism of disease progression in heart failure," *Journal of the American College of Cardiology*, vol. 20, no. 1, pp. 248–254, 1992.
- [35] D. J. Ewing, "Diabetic autonomic neuropathy and the heart," *Diabetes Research and Clinical Practice*, vol. 30, supplement, pp. 31–36, 1996.

## Clinical Study

# Thyroid Remnant Estimation by Diagnostic Dose $^{131}\text{I}$ Scintigraphy or $^{99\text{m}}\text{TcO}_4^-$ Scintigraphy after Thyroidectomy: A Comparison with Therapeutic Dose $^{131}\text{I}$ Imaging

Guanghai Liu, Na Li, Xuena Li, Song Chen, Bulin Du, and Yaming Li

Department of Nuclear Medicine, The First Hospital of China Medical University, Shenyang 110001, China

Correspondence should be addressed to Yaming Li; [yml2001@163.com](mailto:yml2001@163.com)

Received 17 October 2015; Revised 19 November 2015; Accepted 3 January 2016

Academic Editor: James Russell

Copyright © 2016 Guanghai Liu et al. This is an open access article distributed under the Creative Commons Attribution License, which permits unrestricted use, distribution, and reproduction in any medium, provided the original work is properly cited.

In this clinical study, we have compared routine diagnostic dose  $^{131}\text{I}$  scan and  $^{99\text{m}}\text{TcO}_4^-$  thyroid scintigraphy with therapeutic dose  $^{131}\text{I}$  imaging for accurate thyroid remnant estimation after total thyroidectomy. We conducted a retrospective review of the patients undergoing total thyroidectomy for differentiated thyroid carcinoma (DTC) and subsequently receiving radioactive iodine (RAI) treatment to ablate remnant thyroid tissue. All patients had therapeutic dose RAI whole body scan, which was compared with that of diagnostic dose RAI,  $^{99\text{m}}\text{TcO}_4^-$  thyroid scan, and ultrasound examination. We concluded that therapeutic dose RAI scan reveals some extent thyroid remnant in all DTC patients following total thyroidectomy. Diagnostic RAI scan is much superior to ultrasound and  $^{99\text{m}}\text{TcO}_4^-$  thyroid scan for the postoperative estimation of thyroid remnant. Ultrasound and  $^{99\text{m}}\text{TcO}_4^-$  thyroid scan provide little information for thyroid remnant estimation and, therefore, would not replace diagnostic RAI scan.

## 1. Introduction

Thyroid carcinoma is one of the most common malignant tumors in the endocrine system; the estimated incidence of thyroid cancer currently was around 0.01% to 0.03% per year [1]. Differentiated thyroid carcinoma (DTC) accounts for 90% of all thyroid cancers [2].

DTC treatment guidelines recommended a near total or total thyroidectomy for patients with tumor size greater than 1 cm in diameter or those who have multiple lesions or distal metastases. Radioiodine (RAI) remnant ablation has been increasingly used to eliminate the postsurgical thyroid remnant [3].

The remnant thyroid volume affects the ablation dose of RAI [4, 5], so it was important to identify remnant volume for further treatment after surgery. The extent of remnant thyroid plays a significant role for DTC recurrence and the evaluation of remnant thyroid with imaging technique may provide additional information for prediction of the recurrence and also for estimation of the amount of radioiodine to be used for ablation.

$^{99\text{m}}\text{TcO}_4^-$  scintigraphy, routine diagnostic radioiodine whole body scintigraphy, and ultrasound have been widely

used to estimate thyroid remnant following thyroidectomy. However which is the ideal imaging modality for accurate thyroid remnant estimation after total thyroidectomy was not well concluded.

Thyroglobulin (Tg) is glycoprotein secreted by thyroid follicular epithelial cells with plasma half-life of 3.7 h to 4.3 d [6]. Thyroglobulin antibody (TgAb) is the antibody of Tg. Both of them are regulated by thyroid-stimulating hormone (TSH). The serum levels of Tg, TgAb, and TSH have been used as indicators for thyroid remnant [7–9]. In this study, we also observed these parameters and related to thyroid remnant defined by RAI scan.

In this retrospective analysis, we have compared routine diagnostic dose radioiodine whole body scintigraphy,  $^{99\text{m}}\text{TcO}_4^-$  thyroid scan, and ultrasound with that post-iodine-131 ablation therapeutic dose imaging.

## 2. Material and Methods

**2.1. Patients.** This study was preapproved by the hospital institutional review boards of the First Hospital of China Medical University (Shenyang, China). This retrospective

analysis used the following inclusion criteria: total thyroidectomy, no lymph node metastasis or distant metastasis, and the first time of RAI ablation. A total of 100 DTC patients from October 2011 to August 2014 were included; all of them had total thyroidectomy with pathologically confirmed as thyroid papillary carcinoma and were subsequently referred to our department for the first time of RAI remnant ablation. The patients' age ranged from 13 to 71 years (mean 43 years), 76 of them were female and 24 were male. The duration from thyroidectomy to RAI ablation was 1–12 months (mean 4 months). Before RAI ablation, all patients fasted from iodine-enriched foods and medications (sea food, milk products, and iodine containing ointments/balms) for 2–4 weeks. Patients had either  $^{99m}\text{TcO}_4^-$  thyroid scan or diagnostic RAI whole body scan (WBS) or ultrasound (US) examination prior to  $^{131}\text{I}$  ablation. All patients had RAI whole body scans 3 days after therapeutic dose of  $^{131}\text{I}$  administration.

**2.2. Imaging Protocols.** For  $^{99m}\text{TcO}_4^-$  scan, the patients were intravenously injected with  $^{99m}\text{TcO}_4^-$  185 MBq (5 mCi) and after 30 mins, anterior planar thyroid scan was acquired for 5 min using a Symbia T2 SPECT/CT detector (Siemens, Germany) equipped with low-energy and high-resolution collimators (matrix  $256 \times 256$ , Zoom 2), the peak energy is 140 keV, and window width was set as 20%.

For diagnostic dose RAI whole body scan, the patient took 74 MBq (2 mCi)  $^{131}\text{I}$  (NaI) solution orally after overnight fasting and whole body scan was performed 24 hours later using a Symbia T2 SPECT/CT detector equipped with high-energy collimators (matrix  $128 \times 128$ , Zoom 1). The scan speed was set as 15 cm/min.

For therapeutic dose RAI whole body imaging, the patients took  $^{131}\text{I}$  3.7 GBq (100 mCi) orally after overnight fasting for ablate thyroid remnant. Whole body scan was performed 3 days later, whole body scan was done following above-mentioned diagnostic  $^{131}\text{I}$  scan protocol and imaging was obtained from the same device.

Three board-certified nuclear medicine attending physicians read RAI whole body imaging and  $^{99m}\text{TcO}_4^-$  thyroid scan. Negative result was defined as tracer uptake was not exceeding neck background. Each modality imaging was compared with therapeutic dose RAI whole body scan which served as a “gold standard” for defining the presence or absence of remnant thyroid. Severe remnant was defined as imaging agent uptake in the thyroid bed being strong, imaging appearing as “sunshine” shape; mild remnant group as imaging agent uptake in the thyroid bed being weaker, with no “sunshine” appearance; and no remnant defined as no tracer uptake beyond neck background in the thyroid bed [10].

**2.3. Serological Examination.** The serological examination of Tg, TgAb, and TSH was taken in our hospital 1–3 days before the patients took therapeutic dose  $^{131}\text{I}$ .

**2.4. Statistical Analysis.** Statistical analysis was performed by SPSS 17.0; a  $p$  value less than 0.05 was considered as statistically significant.

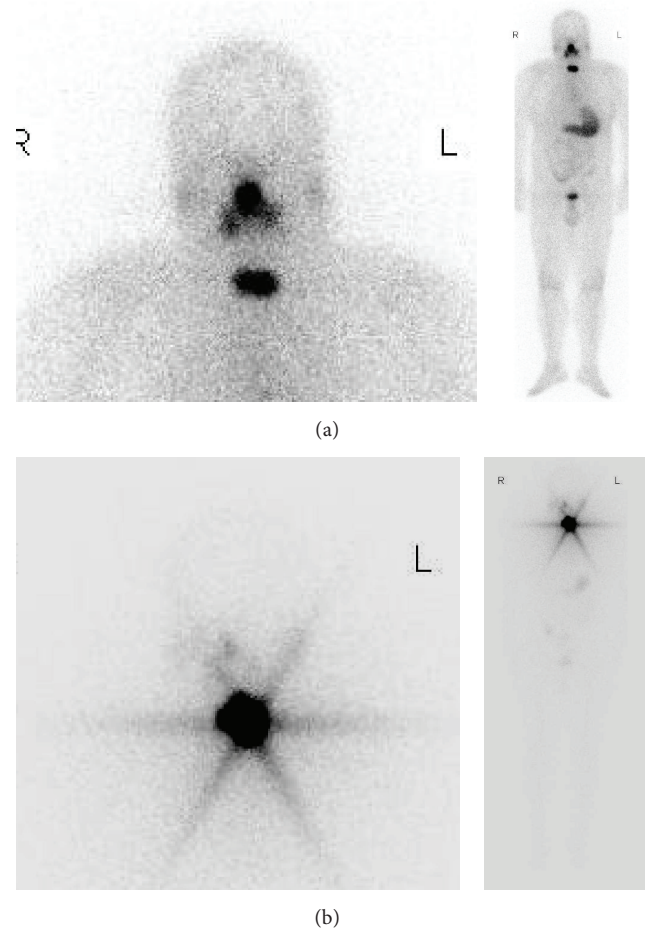


FIGURE 1: Extent of thyroid remnant detected after  $^{131}\text{I}$  ablation imaging (therapeutic RAI whole body scan). (a) Mild remnant of a 37-year-old male after total thyroidectomy. Whole body scan and regional image 3 days after 3.7 GBq (100 mCi)  $^{131}\text{I}$  oral administration. (b) Severe remnant of a 31-year-old female after total thyroidectomy. Whole body scan and regional image 3 days after 3.7 GBq (100 mCi)  $^{131}\text{I}$  oral administration.

### 3. Results

Therapeutic dose RAI whole body scans revealed that all thyroid beds following total thyroidectomy contained residual thyroid tissue which accumulated at least some extent of  $^{131}\text{I}$ . Accordingly, of 100 patients, 55 patients had mild thyroid remnant and 45 had severe remnant. Representative therapeutic RAI images showed mild thyroid remnant (Figure 1(a)) and severe remnant (Figure 1(b)).

Of 100 patients, all had whole body scans three days after therapeutic iodine administration. Before RAI thyroid ablation, ultrasound and  $^{99m}\text{TcO}_4^-$  thyroid scan were done in 45 patients and ultrasound and diagnostic dose  $^{131}\text{I}$  whole body scan were performed in 39 patients, while just ultrasound exam was conducted in 15 patients; the results were summarized in Table 1. Diagnostic RAI scan detected thyroid remnant in 67% (26/39) patients and  $^{99m}\text{TcO}_4^-$  thyroid scan had a sensitivity of 13% (6/45), while as ultrasound the

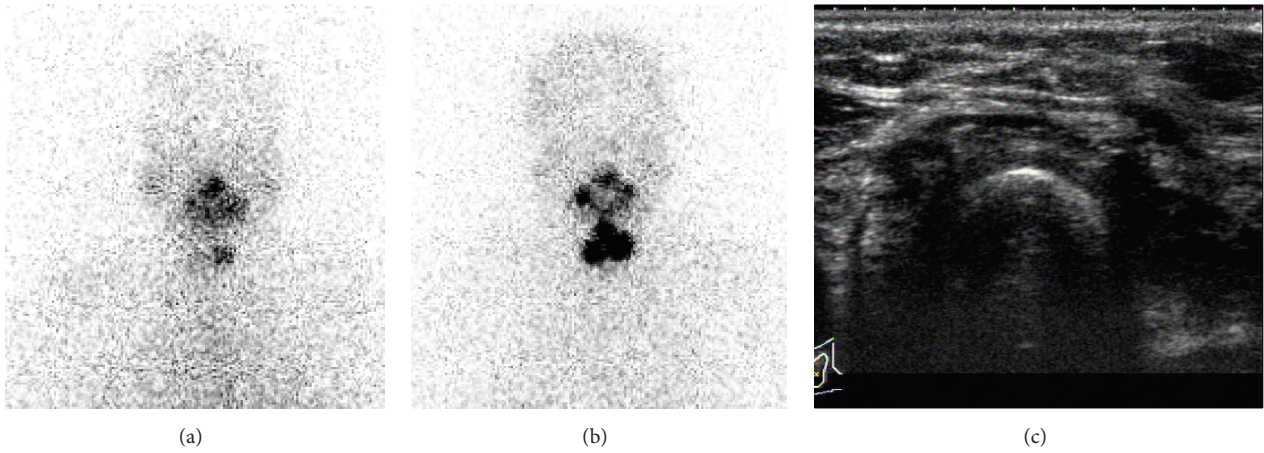


FIGURE 2: Comparing diagnostic <sup>131</sup>I scan with postablation therapy <sup>131</sup>I imaging. A 49-year-old female after total thyroidectomy. (a) Diagnostic RAI scan performed 24 hours after 74 MBq (2 mCi) <sup>131</sup>I oral administration. (b) Therapeutic dose scan performed 3 days after 3.7 GBq (100 mCi) <sup>131</sup>I oral administration 3 weeks after diagnostic <sup>131</sup>I scan. Thyroid remnant is visualized by diagnostic and therapeutic dose of <sup>131</sup>I scans, but smaller residual thyroid is found by diagnostic scan. (c) Ultrasound fails to detect thyroid remnant.

TABLE 1: Comparison of ultrasound <sup>99m</sup>TcO<sub>4</sub><sup>-</sup> thyroid scan and diagnostic dose <sup>131</sup>I scan for thyroid remnant detection.

Imaging strategy	Positive	Negative	Total
Ultrasound	8	91	99
<sup>99m</sup> TcO <sub>4</sub> <sup>-</sup> thyroid scan	6	39	45
Diagnostic dose <sup>131</sup> I scan	26	13	39

TABLE 2: Serum TG, TGAb, and TSH level and extent thyroid remnant.

Serum level	Mild remnant	Severe remnant	<i>p</i>
TG (ng/mL)	4.00 ± 7.24	22.23 ± 52.68	0.000
TGAb (IU/mL)	25.16 ± 65.16	85.27 ± 241.44	0.001
TSH (mIU/mL)	63.82 ± 27.58	47.93 ± 25.92	0.400

Thyroglobulin (Tg); thyroglobulin antibody (TgAb); thyroid-stimulating hormone (TSH).

sensitivity was only 8% (8/99). The sensitivity for diagnostic RAI scan to detect thyroid remnant was significantly higher than <sup>99m</sup>TcO<sub>4</sub><sup>-</sup> thyroid scan (*p* < 0.001) and ultrasound (*p* < 0.001) and there was no significant difference between <sup>99m</sup>TcO<sub>4</sub><sup>-</sup> thyroid scan and ultrasound (*p* = 0.34).

Figure 2 showed thyroid remnant was detected by both diagnostic dose and therapeutic dose RAI whole body scans in a 49-year-old female who underwent total thyroidectomy for treating DTC, though the extent thyroid remnant imaged by diagnostic RAI was apparently smaller than therapeutic RAI scan. Ultrasound failed to detect the presence of remnant thyroid tissue.

On the other hand, 33% diagnostic dose RAI whole body scan failed to map thyroid remnant which was presented in diagnostic RAI imaging (Figure 3). <sup>99m</sup>TcO<sub>4</sub><sup>-</sup> thyroid scan and ultrasound failed to image majority of thyroid remnant, an example of <sup>99m</sup>TcO<sub>4</sub><sup>-</sup> thyroid scan; ultrasound and diagnostic RAI scan were presented in Figure 4.

Serum levels of Tg, TGAb, and TSH between mild group and severe group were analyzed and summarized in Table 2. The levels of Tg and TGAb were significantly higher in severe remnant patients than mild remnant patients; therefore Tg and TGAb can be used as indicators of extent thyroid remnant. TSH values had no statistical difference between the two groups.

As the ability of diagnostic dose RAI whole body scan for detecting thyroid remnant is also dependent on TSH level, we

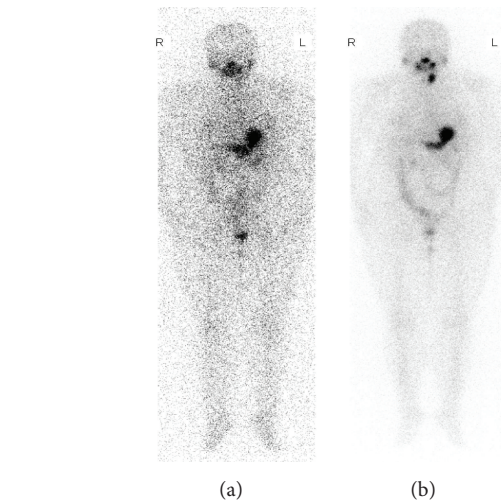


FIGURE 3: Difference between diagnostic and therapeutic dose <sup>131</sup>I scan. A 37-year-old patient with total thyroidectomy. Diagnostic dose whole body scan (a) fails to visualize the presence of thyroid remnant identified by therapeutic dose of <sup>131</sup>I scan (b).

analyzed the TSH level between the two groups of different diagnostic dose RAI whole body scan results and there was no significant difference (*t* = 1.475, *p* = 0.493).

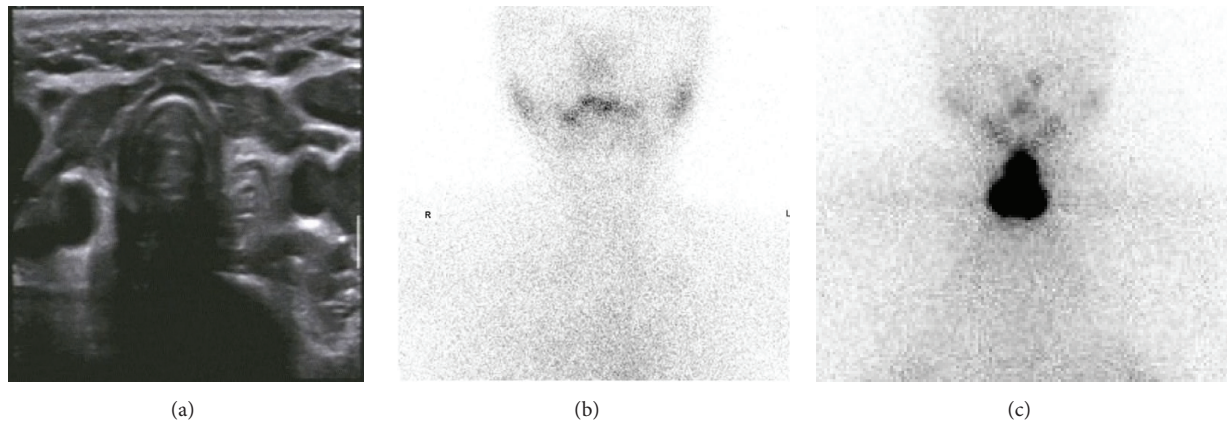


FIGURE 4: Comparing  $^{99m}\text{TcO}_4^-$  thyroid scan and ultrasound therapeutic dose of  $^{131}\text{I}$  scan for thyroid remnant detection in the same patient. A 32-year-old female after total thyroidectomy. Ultrasound (a) and  $^{99m}\text{TcO}_4^-$  thyroid scan (b) fail to visualize thyroid remnant detected by therapeutic dose of  $^{131}\text{I}$  scan (c).

#### 4. Discussion

Although there has been considerable debate as to the role of total versus less than total thyroidectomy (usually lobectomy and isthmusectomy) for differentiated thyroid cancers [11, 12], most people suggest total thyroidectomy. Large databases showing statistically significant differences in outcome between total thyroidectomy and lobectomy for tumors >1 cm. Furthermore, these patients can then undergo RAI therapy and use Tg levels as a marker to monitor recurrent diseases [13]. The guidelines for DTC therapy recommend total thyroidectomy for cancer bigger than 1 cm in diameter. Thyroid remnant in DTC after thyroidectomy may contain micrometastases which may be the source of recurrence or metastasis [14].

A follow-up report of the impact of therapy in 576 patients showed a 45% risk of recurrence in total thyroidectomy only; the risk in total thyroidectomy and TSH suppression therapy and total thyroidectomy + TSH suppression therapy + radioiodine (RAI) remnant ablation were 11% and 2.7%, respectively [15]. Therefore estimation of thyroid remnant and the role of postoperative remnant ablation with RAI is important for curing DTC.

Our therapeutic dose RAI scan findings indicated that thyroid remnant existed in all patients after total thyroidectomy (Figure 1). This is not a surprise: surgeons leave some thyroid tissue near the upper parathyroid and the insertion of the recurrent laryngeal nerve to protect these structures; this is so called near total thyroidectomy [16].

Our data clearly demonstrated that, in addition to therapeutic dose RAI whole body scan, diagnostic RAI scan had far higher sensitivity for thyroid remnant evaluation (Table 1). Although ultrasound and  $^{99m}\text{TcO}_4^-$  thyroid scan are routinely used in thyroid clinic, both strategies provided minimal information with respect to thyroid remnant (Table 1, Figure 4). Therefore, our results suggested not to use ultrasound and  $^{99m}\text{TcO}_4^-$  thyroid scan for thyroid remnant estimation.

$^{99m}\text{TcO}_4^-$  is a widely used tracer for thyroid imaging in clinical setting.  $^{99m}\text{TcO}_4^-$  scan reported a sensitivity of 87%,

specificity of 97%, and accuracy of 92.5% for detecting thyroid remnant and ectopic thyroid tissue when compared to  $^{131}\text{I}$  scan [17].

However, our data indicated that  $^{99m}\text{TcO}_4^-$  thyroid scans provided little information to detect thyroid remnant, which was far worse than  $^{131}\text{I}$  (Figure 4, Table 1). Therefore,  $^{99m}\text{TcO}_4^-$  thyroid scan should be carefully considered to locate thyroid remnant.

Compared to other modalities, the coincidence rate between diagnostic RAI scan and therapeutic RAI imaging was much higher in identifying thyroid remnant. However, we recognize that the difference between diagnostic dose and therapeutic dose scan was apparent (Table 1, Figures 2 and 3), this may be due to the difference in amount of administration dose of  $^{131}\text{I}$  (100 mCi vs. 2 mCi), as well as the time of scans (3 d vs. 1 d). Of note, negative diagnostic RAI imaging frequently indicated mild thyroid remnant.

The levels of Tg, in theory, could not be detected after being fully removed from thyroid tissue. We found that Tg still could be detected 12 months after so called total thyroidectomy; the levels of Tg as well as TgAb in severe group (defined by therapeutic RAI scan) were significantly higher than mild group. Therefore, the serum level of Tg also had a certain value in the evaluation of the degree of postoperative thyroid remnant.

About 10% ~40% DTC patients after total thyroidectomy and  $^{131}\text{I}$  ablation had detectable serum level of TgAb [18, 19], which is probably due to the following reasons: DTC patients might still have memory lymphocyte after treatment, they maintain the ability to produce TgAb; the radiation damage of RAI remnant ablation causes the release of antigen; and metastases have the ability to produce TgAb which become the source of autoantigen. Elevated levels of serum TgAb may also be an indicator of thyroid remnant, but it seems less specific than Tg.

#### 5. Conclusions

Therapeutic dose RAI scan reveals the extent thyroid remnant in all DTC patients following total thyroidectomy. Diagnostic

RAI scan is much superior to ultrasound and  $^{99m}\text{TcO}_4^-$  thyroid scan for the postoperative estimation of thyroid remnant. Ultrasound and  $^{99m}\text{TcO}_4^-$  thyroid scan provide little information for thyroid remnant estimation and, therefore, would not replace diagnostic RAI scan.

### Conflict of Interests

The authors declare that there is no conflict of interests regarding the publication of this paper.

### References

- [1] T. F. Heston and R. L. Wahl, "Molecular imaging in thyroid cancer," *Cancer Imaging*, vol. 10, no. 1, pp. 1-7, 2010.
- [2] S. I. Sherman, "Thyroid carcinoma," *The Lancet*, vol. 361, no. 9356, pp. 501-511, 2003.
- [3] I. D. Hay, G. B. Thompson, C. S. Grant et al., "Papillary thyroid carcinoma managed at the Mayo Clinic during six decades (1940-1999): temporal trends in initial therapy and long-term outcome in 2444 consecutively treated patients," *World Journal of Surgery*, vol. 26, no. 8, pp. 879-885, 2002.
- [4] W. H. Beierwaltes, R. Rabbani, C. Dmuchowski, R. V. Lloyd, P. Eyre, and S. Mallette, "An analysis of 'ablation of thyroid remnants' with I-131 in 511 patients from 1947-1984: experience at University of Michigan," *Journal of Nuclear Medicine*, vol. 25, no. 12, pp. 1287-1293, 1984.
- [5] N. Arslan, S. Ilgan, M. Serdengeçti et al., "Post-surgical ablation of thyroid remnants with high-dose 131I in patients with differentiated thyroid carcinoma," *Nuclear Medicine Communications*, vol. 22, no. 9, pp. 1021-1027, 2001.
- [6] U. Feldt-Rasmussen, P. H. Petersen, H. Nielsen, J. Date, and C. M. Madsen, "Thyroglobulin of varying molecular sizes with different disappearance rates in plasma following subtotal thyroidectomy," *Clinical Endocrinology*, vol. 9, no. 3, pp. 205-214, 1978.
- [7] S. Ha, S. W. Oh, Y. K. Kim et al., "Clinical outcome of remnant thyroid ablation with low dose radioiodine in Korean patients with low to intermediate-risk thyroid cancer," *Journal of Korean Medical Science*, vol. 30, no. 7, pp. 876-881, 2015.
- [8] P. Fabián, A. Erika, T. Hernán, B. Fernanda, U. Carolina, and C. Graciela, "Biochemical persistence in thyroid cancer: is there anything to worry about?" *Endocrine*, vol. 46, no. 3, pp. 532-537, 2014.
- [9] P. W. S. Rosario, J. B. N. dos Santos, and M. R. Calsolari, "Follow-up of patients with low-risk papillary thyroid carcinoma and undetectable basal serum thyroglobulin after ablation measured with a sensitive assay: a prospective study," *Hormone and Metabolic Research*, vol. 45, no. 12, pp. 911-914, 2013.
- [10] R.-J. Zou, H.-L. Fu, J.-C. Wu, J.-N. Li, and H. Wang, "Clinical value of combination of multiple radionuclide imaging methods in 131I therapy for differentiated thyroid carcinoma," *Journal of Shanghai Jiaotong University*, vol. 30, no. 3, pp. 256-258, 2010.
- [11] K. Y. Bilimoria, D. J. Bentrem, C. Y. Ko et al., "Extent of surgery affects survival for papillary thyroid cancer," *Annals of Surgery*, vol. 246, no. 3, pp. 375-381, 2007.
- [12] J. P. Shah, T. R. Loree, D. Dharker, and E. W. Strong, "Lobectomy versus total thyroidectomy for differentiated carcinoma of the thyroid: a matched-pair analysis," *The American Journal of Surgery*, vol. 166, no. 4, pp. 331-335, 1993.
- [13] N. G. Iyer and A. R. Shaha, "Controversies and challenges in the management of well-differentiated thyroid cancer," *The Indian Journal of Surgery*, vol. 71, no. 6, pp. 299-307, 2009.
- [14] B. Dewil, B. Van Damme, V. V. Poorten, P. Delaere, and F. Debruyne, "Completion thyroidectomy after the unexpected diagnosis of thyroid cancer," *B-ENT*, vol. 1, no. 2, pp. 67-72, 2005.
- [15] E. L. Mazzaferri, R. L. Young, J. E. Oertel, W. T. Kemmerer, and C. P. Page, "Papillary thyroid carcinoma: the impact of therapy in 576 patients," *Medicine*, vol. 56, no. 3, pp. 171-196, 1977.
- [16] D. F. Schneider, K. A. Ojomo, H. Chen, and R. S. Sippel, "Remnant uptake as a postoperative oncologic quality indicator," *Thyroid*, vol. 23, no. 10, pp. 1269-1276, 2013.
- [17] N. F. Khammash, R. K. Halkar, and H. M. Abdel-Dayem, "The use of technetium-99m pertechnetate in postoperative thyroid carcinoma. A comparative study with iodine-131," *Clinical Nuclear Medicine*, vol. 13, no. 1, pp. 17-22, 1988.
- [18] J. I. Torrrens and H. B. Burch, "Serum thyroglobulin measurement. Utility in clinical practice," *Endocrinology and Metabolism Clinics of North America*, vol. 30, no. 2, pp. 429-467, 2001.
- [19] M. D. Ringel, P. W. Ladenson, and M. A. Levine, "Molecular diagnosis of residual and recurrent thyroid cancer by amplification of thyroglobulin messenger ribonucleic acid in peripheral blood," *The Journal of Clinical Endocrinology and Metabolism*, vol. 83, no. 12, pp. 4435-4442, 1998.